# Vortex breakdown and its topologies in turbulent flows within a typical swirl combustor geometry

Nitesh Kumar Sahu<sup>a,\*</sup>, Anupam Dewan<sup>b</sup> and Mayank Kumar<sup>c,\*</sup>

- a: Department of Fuel, Minerals & Metallurgical Engineering, Indian Institute of Technology (ISM) Dhanbad, Dhanbad, Jharkhand 826004, India
- b: Department of Applied Mechanics, Indian Institute of Technology Delhi, Hauz Khas, New Delhi – 110016, India
- c: Department of Mechanical Engineering, Indian Institute of Technology Delhi, Hauz Khas, New Delhi – 110016, India
- \* Corresponding Author (1): Email nitesh@iitism.ac.in, Tel: +91-32-6223-5158
- \* Corresponding Author (3): Email <a href="mailto:kmayank@mech.iitd.ac.in">kmayank@mech.iitd.ac.in</a>, Tel: +91-11-2659-7392

<u>Note</u>: The following article has been submitted to Physics of Fluids and is Under Review. After it is published, it will be found at the journal website.

© 2025 Nitesh Kumar Sahu, Anupam Dewan, and Mayank Kumar. This article is distributed under a Creative Commons Attribution-NonCommercial 4.0 International (CC BY-NC) License. <a href="https://creativecommons.org/licenses/by-nc/4.0/">https://creativecommons.org/licenses/by-nc/4.0/</a>

#### **Abstract**

We investigate vortex breakdown (VB) and its dominant topologies in turbulent, non-reacting flows within a canonical swirl-combustor using large-eddy simulations (LES). A baseline configuration and operating-conditions are first used to validate the LES solver, after which five additional cases with different swirler vane-angles are simulated while keeping all other flow and geometric parameters fixed. The onset of VB is quantified using the generic swirl-strength formulation,  $SN_a$ , by detecting the appearance of internal

recirculation zones (IRZs) in the mean flow, thereby excluding cases with highly intermittent VB. Analysis of the mean flow shows that  $SN_{a}$  measured within  $40~\mathrm{mm}$ downstream of the swirler best represents the flow's swirl-strength compared with commonly used alternatives. A stable-VB first appears in the flow with  $25^{\circ}$  vane-angle.  $SN_q \approx 0.35$ . Q-criterion iso-surfaces and velocity time-series at VC-footprints show a single-helix VC to prevail across all investigated vane-angles; up-to  $60^{\circ}$ ,  $SN_a = 1.15$ . Weaker double-helix characteristics appear. They are quadratic self-interaction of singlehelix tone for vane-angles  $\leq 50^{\circ}$ , but are quadratically independent in  $60^{\circ}$  case, indicating a distinct helical hydrodynamic-mode. Axisymmetric IRZ oscillations interact with helical VC-dynamics in  $25^{\circ}$  and  $60^{\circ}$  cases. VC precesses as stable limit-cycle oscillation in  $40^{0} - 50^{0}$  cases, by marginally-stable mode, and precession waxes-andwanes strongly in  $25^{\circ}$  and  $60^{\circ}$  cases, by stochastic-forcing on slightly-stable mode. Alongside a coherent VC-strand, a weakly-coherent strand originates from swirler. Its precession frequencies match with lowest precession frequencies of coherent strands, corroborating its precession-based origin. Overall, we establish critical-values, evaluation locations, and a topology map for predicting and interpreting VB-states in isothermal swirl-combustor flows.

## Acronyms

CB Center-body

IRZ Internal recirculation zone

ISL Inner shear layer

OSL Outer shear layer

Re Reynold number

 $Re_{inlet}$  Inlet Reynolds number

*SN<sub>c</sub>* Conventional swirl number

 $SN_a$  Generic swirl number

VB Vortex breakdown

VC Vortex core

## 1. Introduction

Swirl combustors are widely employed in combustion facilities, such as gas turbines [1,2] and pulverized coal-based reactors [3-5]. A typical swirl combustor design features an expansion plane connecting two tubes of different diameters and a swirl generator in the smaller diameter tube [1, 6-8]. These features are incorporated to induce vortex breakdown, essential for flame stabilization in the inherently turbulent flow of swirl combustors [9, 10]. Vortex breakdown is a phenomenon marked by the sudden emergence of a low-velocity recirculation zone in the core of a swirling flow [9]. Moreover, a vortex core in a swirling flow can break down into various topologies [9, 11-13], each of which uniquely influences the flow dynamics. The dynamics in turn, differently affect mixing [9, 14, 15], flame stability [16, 17], pollutant emissions [18], hotspot formation [18-20] and instability characteristics [18-20] in swirl combustors.

Therefore, comprehensive knowledge of the predominant vortex breakdown (VB) topologies and the parameter space governing both the onset of VB and the transitions among its various topologies in swirl combustors is crucial.

Since vortex breakdown was first observed over seven decades ago, numerous theories have been proposed to explain its onset mechanism and resulting flow topologies. A successful theory would identify the parameters that govern both the onset of VB and the transitions among its various topologies [9]. However, only a few recent theories, specifically those invoking a jump-like transition in vortex core dynamics about a critical state within a flow, have been able to partially explain the VB mechanism and identify the parameters governing it [9, 21-23]. Accordingly, experimental observations and numerical simulations are generally relied upon for identifying the parameters and their critical thresholds governing the onset and topology of VB [11, 13, 21]. An ensemble of flow-based and geometry-based parameters is expected to be of relevance [11-13, 21]. Combustion is known to modulate VB characteristics by altering flow properties [8, 20]. However, in the present study, we examine the effect of relevant parameters decoupled from combustion. Accordingly, we focus only on non-reacting, isothermal flow inside swirl combustors. The influence of combustion parameters such as heat release rate, temperature of flow, etc., on VB characteristics in swirl combustors will be explored in our forthcoming work.

Based on the previous studies [11-13, 21], swirl strength emerges as a relevant flow parameter. Earlier researchers [11-13, 24, 25] used various scaling-based definitions—such as the circulation number,  $\Omega$ , and the inverse of Rossby number,  $Ro^{-1}$ ,

shown in Eq. (1)—to quantify swirl strength of isothermal flows. However, evaluation of these quantities in flows without solid-body rotation require additional assumptions and supplementary analysis [21, 24, 25]. Building on the conservation laws, Chigier and coworkers [26–28] introduced a non-dimensional number naming it swirl number, shown in Eq. (2), which can be evaluated directly from local flow-field data. Their goal was to develop a relevant parameter that remains constant in the absence of viscous dissipation and otherwise exhibits a net decay along the flow, with weak variation rates, in a region of fixed-cross-section away from any flow transition. Owing to these traits, swirl number has become the standard metric for quantifying swirl intensity [29]. Its most generic formulation for an isothermal flow is given in Eq. (3) [29]. In practice, Chigier *et al.* [26] also proposed a simplified version,  $SN_p$ , [Eq. (4)] which neglects the mean of the fluctuating terms—trading some generality for ease of use, as we will discuss later.

$$\Omega = \frac{\Gamma}{\langle U_a \rangle_{A-ava} d_c} \qquad Ro = \frac{2\langle U_a \rangle_{A-ava}}{\omega_c d_c} \tag{1}$$

$$SN = \frac{2*time-mean of the axial flux of tangential momentum}{d_c*time-mean of the axial flux of axial momentum}$$
 (2)

$$SN_g = \frac{2 \iint_{A_c} \rho(\langle U_a \rangle \langle U_t \rangle + \langle u'_a u'_t \rangle) r dA}{d_c \iint_{A_c} \{(\langle p \rangle - p_{ref}) + \rho(\langle U_a \rangle \langle U_a \rangle + \langle u'_a u'_a \rangle)\} dA} \qquad U_t = \frac{(\vec{r} \times \vec{U}) \cdot \hat{e}_a}{|\vec{r}| = r}$$
(3)

$$SN_p = \frac{2 \iint_{A_c} \rho(\langle U_a \rangle \langle U_t \rangle) r dA}{d_c \iint_{A_c} \{(\langle p \rangle - p_{ref}) + \rho \langle U_a \rangle \langle U_a \rangle\} dA}$$
(4)

here  $\Gamma$  is the flow circulation,  $< U_a>_{A-avg}$  is the area-averaged time-mean axial-velocity component,  $\omega_c$  is a characteristic rotation rate and  $d_c$  is a characteristic diameter, <  $U_a>$  and <  $U_t>$  are the time-mean axial & azimuthal/ tangential components of velocity, respectively,  $< u_a'u_t'>$  is their cross-correlation and  $< u_a'u_a'>$  is the variance

of axial-velocity fluctuations, is the time-mean local static pressure,  $p_{ref}$  is a reference pressure. All formulations assume statistically stationary flow.  $\hat{e}_a$  is unit-vector along flow.

The foregoing overview on swirl numbers is to provide a consistent basis for the subsequent discussions in the present work. Sarpkaya [11] as well as Fahler and Leibovich [12] experimentally investigated the impact of Reynolds number (Re) and circulation number  $(\Omega)$  on the onset and topology of VB inside a diverging tube with the cone angle of 30. They observed that the interplay of these parameters governs the onset and topology of VB in the investigated geometry. VB occurred only when Re exceeded 3700 in the flow with the lowest investigated circulation number,  $\Omega=1.07$ , whereas VB was observed for all the investigated Reynolds numbers above 700 in the flow with  $\Omega=3.00$ . A total of six VB topologies/modes were observed in the diverging tube [12]. Only two of these VB modes, namely spiral VB (single helix mode) and bubble VB, were predominant in flows with  $Re \geq 4000$ . Bubble VB was the only mode observed at higher values of  $\Omega$  in these flows. The bubble topology became unstable below a certain threshold value of  $\Omega$ where it intermittently transitioned into either a single helix or double helix configuration. The VB topology stabilized exclusively as the single helix configuration below a further lower threshold value of  $\Omega$ , i.e., only spiral VB occurred at lower values of  $\Omega$  in flows with  $Re \geq 4000$ . These threshold values of  $\Omega$  decreased with increase in Re. Syred and Beer [21] reparametrized Sarpkaya's results [11] by replacing  $\Omega$  with a highly simplified formulation of swirl number expressed here as  $SN_c$  and defined in Eq. (5). As expected,

the results show that bubble VB predominated at higher values of  $SN_c$ , while spiral VB predominated at lower values of  $SN_c$  in flows with  $Re \ge 4000$ .

$$SN_c = \frac{2\int_0^{R_0} 2\pi\rho \bar{U}_a \bar{U}_t r^2 dr}{a_c \int_0^{R_0} \{\rho \bar{U}_a \bar{U}_a\} 2\pi r dr}$$

$$\tag{5}$$

Escudier and Zehnder [13] investigated the impact of divergence/cone angle on VB characteristics by systematically testing various short diverging tubes with cone angles up to  $25^{\circ}$  within a confined facility. Their results demonstrated that larger divergence angles led to an earlier onset of VB. Furthermore, only the bubble and spiral VB modes predominated in flows with  $Re \geq 4000$  across all the investigated divergence angles. Bubble VB exclusively appeared at higher values of  $\Omega$ , while spiral VB was the only mode visible at lower values of  $\Omega$  under these conditions.

Based on the aforementioned studies [11-13], it is likely that the predominant VB modes within a typical swirl combustor configuration, described earlier, are also independent of  $Re_{inlet}$  at least for  $Re_{inlet} \geq 10^4$  ( $Re_{inlet}$  was used in [11-13]). This range of  $Re_{inlet}$  is typical for practical reactor operations [3-6] and is therefore the focus of the present work. Accordingly, it seems reasonable to identify the prevailing VB topologies in an isothermal swirl combustor by investigating it over a wide range of operating conditions that influence VB, where  $Re_{inlet}$  has any value above  $10^4$ . Swirl strength was identified as one such parameter in the above studies. Furthermore, in a typical swirl combustor geometry, the expansion ratio, ER [Eq. (6)], could also be a parameter influencing the VB topology.

$$ER = \frac{hydraulic\ dia\ of\ tube\ after\ expansion\ plane}{hydraulic\ dia\ of\ tube\ before\ expansion\ plane} \tag{6}$$

A few numerical studies [30, 31] have investigated predominant VB modes in swirl combustor geometries at inlet Reynolds numbers up to 3000. However, no attempt has yet been made to resolve the dominant VB topologies in swirl combustors for  $Re_{inlet} \geq$ 104. Recently, Vanierschot et al. [32] conducted an experiment to investigate the VB topology within a swirl combustor using a tomographic PIV, albeit at only a single value each of  $SN_c$  and  $Re_{inlet}$  (operating conditions are such that the effect of outlet contraction on VB characteristics is negligible [33]).  $Re_{inlet}$  was approximately  $1.4 \times 10^4$ ,  $SN_c$  was 0.36 and ER of the investigated setup was just above 20.0 [32].  $SN_c$  was measured at the expansion plane immediately downstream of the swirler. The VC structure at each measured instant was revealed using the iso-surface of a suitable value of the Q-criterion. These iso-surfaces exhibited the double helix VC structure across the investigated time period. When the instantaneous velocity field data were phaseaveraged, to isolate the large-scale flow structures, the reproduced iso-surface of the Qcriterion again exhibited a double helix VC. Accordingly, Vanierschot et al. [32] reported the formation of a stable double helix VB topology. Lu et al. [34] numerically investigated flow fields with  $SN_c=0.30$  and 0.50,  $Re_{inlet}\approx 1.25\times 10^5$  within a swirl combustor having  $ER \approx 1.5$ .  $SN_c$  was calculated just downstream of the swirler. The VB appeared intermittently at  $SN_c=0.30$ , while a stable VB was observed at  $SN_c=0.50$ . The instantaneous fields of velocity, pressure and iso-surfaces of vorticity presented in the article clearly depict the formation of a stable double helix VB in the latter case, which is of practical interest. However, the double helix VB was rarely observed in flows with  $\textit{Re}_{inlet} \geq 4000$  inside diverging and constant diameter tubes, and when it appeared it was unstable or intermittent [11-13]. Notably, the experiments in [32] and simulations in [34] did not adopt any systematic approach to stabilize this rare VB mode, making it an intriguing subject for further investigation.

One possible reason for this unique occurrence might be the difference in the profile of the center-body (CB) of swirlers used in [32] and [34] compared to the previous relevant works [11-13]; (CB with a bluff-body profile creates a separation bubble at its tip that eases flame ignition by providing a hot spot [36]). Vanierschot *et al.* [32] and Lu *et al.* [34] used center-bodies with bluff-body profiles, whereas previous studies [11-13] employed either streamlined center-bodies or omitted them entirely. Vortex shedding from a bluff body evolves into a coherent helical structure in its wake under conditions suitable to excite the wavemaker of a global helical instability [35]. The interaction of this response with a confined swirling flow may have induced the formation of the stable double helix VB observed in [32, 34]. To isolate the primary cause, we simulate an isothermal swirl combustor with a bluff body profiled CB and operating at  $Re_{inlet} \geq 10^4$ , where if a double helix is observed we investigate the mechanism of its formation.

Taamallah et~al.~ [20] simulated both reacting and non-reacting flows with  $SN_c \approx 0.70~$  and  $Re_{inlet} = 2.0 \times 10^4~$  in a swirl combustor with ER = 2.0~ and a swirler with a sharp-edged CB using FVM-filtered large-eddy simulation (LES) approach. The sharp-edged CB is effectively a bluff-body. As mentioned earlier, the focus of the present study is exclusively on non-reacting flows. Taamallah et~al.~ [20] reported the formation of a nearly stable single helix VB that occasionally transitioned into a double helix configuration, a dominant topology and transition behavior not observed in other swirl

combustors of interest [32, 34]. However, Taamallah et al. [20] employed first-order accurate spatial discretization schemes for a few quantities along with a non-zero subgrid closure in their model. Such a combination introduces significant numerical diffusion into discretized governing-equations [37]. Further, they did not provide sufficient evidence to substantiate the formation of the claimed VB topologies. Their result showing 2-D slice of vortex core (VC) on a streamwise plane, using lambda- $2/\lambda_2$ -criterion [38] at several instances, reveals only a single patch. Still, Taamallah et al. [20] concluded the occasional presence of a double helix configuration without any additional justification. Hence, an appropriate LES along with a proper presentation of the results, 2-D and 3-D presentation of VC like in [32, 34, 38], is necessary for the setup in [20] to correctly identify the corresponding VB topology. Notably, the geometries studied in [20, 32, 34] effectively correspond to the typical swirl combustor configuration, which is specified in the very beginning of this section. No outlet contraction is one of the features of a typical swirl combustor. The word effectively is to imply that the cases where the effect of outlet contraction on VB is negligible are also considered [32, 33].

Furthermore, the possibility of a spiral VB topology forming in [20] rather than the double helix VB observed in [32] and [34] cannot be dismissed since the value of  $SN_c$  among these studies differ significantly. Other VB topologies may also form in swirl combustors with  $Re_{inlet} \geq 10^4$  at swirl strengths different from those considered in [20, 32, 34]. Examining flow fields across a wide range of swirler vane-angles in the setup of [20], with other variables held constant, will resolve the dependence of VB topologies on swirl strength. This examination would also reveal the VB topologies that predominate

under those fixed conditions. As discussed earlier, the identified VB topologies would also predominate in any swirl combustor operating at  $Re_{inlet} \geq 10^4$  with a typical geometry. Recall that a typical swirl combustor geometry corresponds to a combustor having two tubes connected by an expansion plane with a swirler placed in the smaller diameter tube. Although ER could also influence these dominant topologies, we will argue in the Results and Discussion section that its effect on VB topology can be delineated based on the available literature and the additional investigations proposed above. Further,  $ER \geq 1.5$  is common in reactor geometries from lab-scale to large-scale facilities [3-5, 20, 32, 34] and therefore we exclusively focus on this range in the present work.

Next, we examine the parameters governing the onset of VB in swirl combustors. As stated earlier, Sarpkaya [11] as well as Syred and Beer [21] demonstrated that the interplay of swirl strength and Re governed the onset of VB in diverging tubes. However, the onset of VB in swirling jets issuing from straight nozzles with  $Re_{nozzle} \geq 1200$  depended only upon swirl strength [21, 39]. Hallets and Toews [40] confirmed the applicability of this behaviour to swirl combustors for a given ER when  $Re_{inlet} \geq 10^4$ . They also found the critical value of swirl strength to depend on the inlet velocity profile. However, we do not focus on this aspect in the present work for conciseness. Furthermore, the critical value was found to be almost independent of ER in swirl combustors with  $ER \geq 1.5$  [40]. Notably, this observation is of importance since our focus in the present work is only on reactor geometries with  $ER \geq 1.5$ , as mentioned earlier. Hallets and Toews [40] measured the swirl strength in the experiments using a simplified formulation of SN,  $SN_s$  [Eq. (7)], at a location well-upstream of the expansion plane.

$$SN_S = \frac{2\int_0^{R_0} 2\pi\rho \bar{U}_a \bar{U}_t r^2 dr}{d_{inlet} \{\rho_{inlet}(\pi r_{inlet}^2) U_{a,mean-inlet}^2\}}$$
(7)

here  $U_{a.mean-inlet}$  is the mass flux weighted mean axial-velocity.

Further, we anticipate that the critical value of any other swirl number formulation would also exhibit a similar degree of independence from ER and  $Re_{inlet}$  for swirl combustors with  $ER \geq 1.5$  operating at  $Re_{inlet} \geq 10^4$ . Both Terhaar et~al. [41] and Vanierschot et~al. [32] employed  $SN_c$  [Eq. (5)] to quantify swirl strength in their swirl combustors operating under conditions relevant to the present work. However, a comparison of their findings reveals substantially different critical values of  $SN_c$ . Terhaar et~al. [41] in an experimental-cum-numerical study measured the critical value of  $SN_c$  well above the expansion plane to be 0.47 for a non-reacting flow with  $Re_{inlet} = 5.0 \times 10^4$  in a swirl combustor with  $ER \approx 3.0$ . In contrast, Vanierschot et~al. [32] observed a well-developed internal recirculation zone in a swirling flow with  $Re_{inlet} = 1.4 \times 10^4$  within a combustor with  $ER \approx 20.0$  even at  $SN_c = 0.36$  measured just after the expansion plane (operating under conditions where effect of outlet contraction on VB is not substantial).

According to Vignat et~al. [29], the above-mentioned discrepancy arose because  $SN_c$  varies significantly within swirl combustors with a dramatic variation across the expansion plane. Further, the plane of measurement of  $SN_c$  in the two studies are arbitrary with no correspondence. The investigation of an isothermal swirl combustor with ER=100 operating at  $Re_{inlet}=1.1\times10^4$  in [29] indicates a similar behavior for other simplified SN formulations. They argued that a useful comparison of flow fields based on SN could be done through a SN formulation whose value does not vary

significantly, at least, in parts of combustors with no sudden geometric transition in between.

Vignat et al. [29] observed that  $SN_g$  remained nearly constant in two distinct regions: (i) the inlet tube and (ii) a region located downstream and sufficiently away from the expansion plane, with a different value in each region. This behavior is expected because  $SN_a$ , Eq. (3), is based on the conceptual basis of the SN proposition without any simplification, discussed earlier. In contrast, simplified swirl number formulations did not exhibit such behavior.  $SN_c$ , Eq. (5), was shown in [29] to undergo large non-monotonic spatial variations even in the above two regions, with a strong dependence on local geometrical changes and other flow parameters. Consequently, the values of  $SN_c$ measured at a corresponding location in two swirl-combustors with nearly the same value of  $SN_g$  in the surrounding region may differ significantly.  $SN_p$  [Eq. (4)], another simplified form of SN performs worse. It was discussed in [29] that since  $SN_p$  is obtained by omitting the turbulent fluctuation terms it could often yield negative swirl strengths, a clear physical inconsistency. Therefore, Vignat et al. [29] discarded  $SN_p$  and it is likewise excluded from the present investigation. Based on a similar argument, Vignat et al. [29] reported this generic formulation as the most appropriate measure of swirl strength in isothermal flows.

However, the work in [29] did not resolve the critical values of  $SN_g$  for swirl-combustors. Nor did they explore the dependence of its critical value on parameters like ER and  $Re_{inlet}$ , as addressed by the work in [40] for  $SN_s$ . The suitability of the  $SN_s$  formulation is not explicitly discussed in [29], which is notable given that its critical value

was reported to exhibit only weak dependence on other key parameters in [40]. Further, Vignat et~al. [29] did not specify how far the second suitable region for measuring  $SN_g$  should be from the expansion plane, nor did they clarify its possible dependence on key parameters. They also did not express any preference between the two suitable regions for evaluating  $SN_g$ , a choice that may impact its applicability—as discussed in the *Results* and *Discussion* section of the present work.

A key observation that supports the use of  $SN_g$  as the most appropriate formulation is its property of remaining nearly constant in certain regions of the flow.  $SN_g$  complies with the swirl number proposition described earlier. However, [29] reveals that the negligible variation in  $SN_g$  in the two identified regions was due to their short lengths, which allowed only limited decay of the fluxes involved in the formulation of  $SN_g$ . But what if these regions are relatively long?

This final point explains why  $SN_g$  appeared as the most appropriate swirl number formulation in isothermal flows in [29]. However, this expectation has so far only been supported by analysis of a single swirl combustor flow in [29]. A complementary analysis over a broader set of cases is required to verify the generalizability of its suitability, and this is presented in the present work. Our investigation also addresses, to some extent, the group of issues outlined in the preceding paragraph.

Finally, to address the gaps and dilemmas identified in the presented literature, a strategy based on numerical investigations is adopted in the present work. The isothermal swirl combustor flow in Taamallah *et al.* [20] is simulated by solving appropriately discretized Favre-filtered governing equations using a segregated, pressure-based

compressible solver of the OpenFOAM-v10 open-source CFD software. The predicted velocity field for this base case is validated against the corresponding experimental data [20]. Then the validated solver is employed to simulate five additional cases each with a different swirler vane-angle while keeping all the other flow and geometry parameters the same as in the base case [20]. The results are analysed to (1) quantify the critical swirl strength using the generic formulation,  $SN_g$  [Eq. (3)] [29], (2) verify the generality of its appropriateness over  $SN_c$ , Eq. (5), and  $SN_s$ , Eq. (7), and (3) address a group of related queries discussed two paragraphs earlier. Further, the 3-D structure of VCs in the simulated cases are examined to assess the dependence of VB topologies on swirl strength and to identify the dominant topologies. If we observe a stable double helix VC, we will investigate a possible mechanism for its formation to resolve a possible reason of its absence in confined swirling flows with no CB or a perfectly streamlined CB in [11-13]. The critical value of  $SN_g$  and the resolved VB topology characteristics may be applicable to any relevant swirl combustor flows. Notably, relevant swirl combustor flows in the present work signify swirl combustors with a sudden expansion such that  $ER \ge 1.5$  and a negligible outlet contraction operating at  $Re_{inlet} \geq 10^4$ .

# 2. Geometry and flow conditions

According to the present investigation strategy, we develop a computational model to reinvestigate the flow field in [20]. We adopt the computational domain and isothermal flow conditions in [20] as our base case. The domain is a truncated section of a lab-scale swirl combustor facility in the reacting gas dynamics lab at MIT [6, 7, 20]. Figures 1a and 1b show the 3-D geometry and a cross section of the computational domain. It comprises a  $38 \text{ mm } \emptyset \times 120 \text{ mm}$  long tube and a  $76 \text{ mm } \emptyset \times 225 \text{ mm}$  long tube connected via an expansion plane. An axial swirler with a sharp-edged center-body and eight vanes is mounted midway in the smaller tube. Figure 1c details the swirler geometry and highlights the key flow structures that typically form inside swirl combustors. The swirl vanes are inclined at  $45^{\circ}$  to the flow direction, not shown in figure 1c. The thickness and height of swirl vanes are not mentioned in [20] and therefore we estimated them through the scaling of a detailed swirler image in an earlier publication [42], yielding vane thickness and height of 1 mm and 24 mm, respectively.

Air at atmospheric pressure and temperature of 300 K enters axially into the computational domain through the smaller tube with a mean speed of 8.2 m/s, yielding  $Re_{inlet}=2\times10^4$  based on  $v_{air@300\,K}=1.56\times10^{-5}$  m²/s. Air then sweeps over the swirler to acquire swirl and subsequently expands into the larger diameter tube. The axial entry mimics the effect of choke plate positioned upstream of the computational domain in the experimental setup [20].

To validate the comprehensive model developed in the present work we compare its predictions for this base case to the corresponding experimental data [20]. Using the validated model, we further investigate the flow fields corresponding to various other vane-angles keeping intact other features of swirl combustor geometry and flow conditions.

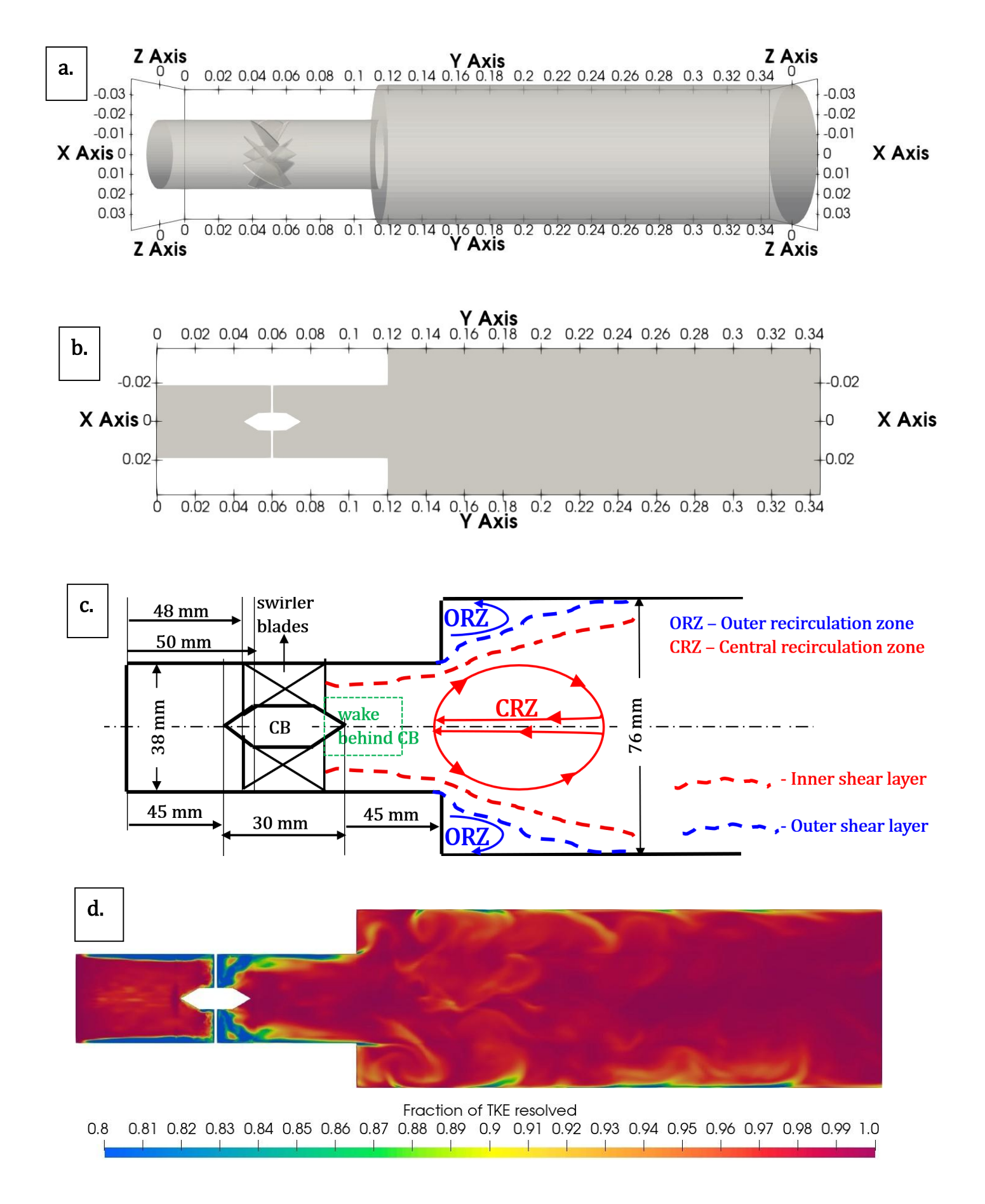


**Figure 1. (a)** Computational geometry of the base case with an expansion plane and a swirler comprising of a center-body (CB) & eight vanes each inclined at 45° from flow direction. It is truncated portion of a larger facility in [20] **(b)** a streamwise plane passing from the centreline of the computational domain **(c)** schematic of the typical flow structures that form in such configurations **(d)** contours of the fraction of resolved turbulent kinetic energy (TKE)

#### 3. Mathematical formulation and numerical solver

## 3.1. Governing equations and boundary conditions

The compressible flow governing equations are solved using the finite-volume method (FVM) for simulations in the present work. Although the inlet Mach number here is low  $(Ma = \frac{8.2}{222} \approx 0.025)$ , we retain the compressible formulation to capture the vorticoacoustic interaction, which is known to influence vortex structures even at such low Mach numbers [34].  $Re_{inlet} = 2 \times 10^4$  across all the cases simulated in the present work. A wide spectrum of length and time scales persist in each of these turbulent flows, where resolving nearly all the scales would incur a prohibitive cost [43]. Therefore, we adopt the LES approach that resolves energetic eddies. Technically, LES resolves scales up to a fraction of the inertial sub-range in turbulence spectrum and the effect of smaller scales on resolved scales is typically modelled [43]. This is achieved in LES by solving spatially filtered governing equations. Spatial filtering removes length-scales smaller than the filter width from flow variables and the corresponding temporal scales, owing to spatiotemporal coupling in turbulence [44]. However, it introduces some residual or sub-filtered quantities that either are modeled or neglected for closure, depending upon the inherent dissipation of the numerical schemes used in the solution of LES equations [37, 43]. We use here OpenFOAM-v10, an open-source CFD software, in which FVM discretization implicitly performs filtering operation with a filter width equivalent to the size of corresponding grid element [37]. Interestingly, the truncation error from lower-order accurate discretization schemes replaces the need for modeling of sub-filtered/sub-grid quantities [37, 43]. However, a second-order accurate or better numerical discretization schemes may be required to enhance numerical accuracy with which sub-grid modeling improves LES predictions [37]. To clarify, a version of *modified* governing equations, i.e., *PDEs* satisfied by the numerical solutions [43], retaining only the leading order truncation errors are given below [6, 45].

$$\frac{\partial \overline{\rho}}{\partial t} + \frac{\partial (\overline{\rho} \, \widetilde{u_i})}{\partial x_i} = 0 \tag{8}$$

$$\frac{\partial \overline{\rho} \widetilde{u_i}}{\partial t} + \frac{\partial (\overline{\rho} \widetilde{u_i} \widetilde{u_j})}{\partial x_j} = -\frac{\partial \overline{\rho}}{\partial x_i} + \frac{\partial}{\partial x_j} (\overline{\tau_{ij}} - \tau_{ij}^{\text{D}} - \tau_{ij}^{\text{SGS}})$$
(9)

$$\frac{\partial \overline{\rho}\widetilde{h}}{\partial t} + \frac{\partial (\overline{\rho}\widetilde{u_i}\widetilde{h})}{\partial x_i} + \frac{\partial \overline{\rho}\widetilde{K}}{\partial t} + \frac{\partial (\overline{\rho}\widetilde{u_i}\widetilde{K})}{\partial x_i} - \frac{\partial \overline{p}}{\partial t} = \frac{\partial}{\partial x_i} (-\overline{q_i} - H_i^{\text{D}} - h_i^{\text{SGS}})$$
(10)

These equations result from the Taylor series expansion of the FVM-discretized governing equations [43], where the time-derivatives in temporal-truncation errors are converted to spatial-derivatives.  $\overline{\phi(x)}$  represents filtered version of a scalar variable  $\phi(x)$ , x is a location vector. The tilde symbol ( $\sim$ ) denotes density-weighted filtering, also called Favre-filtering,  $\overline{\phi(x)} = \frac{\overline{\rho(x)\phi(x)}}{\overline{\rho(x)}}$ .  $K = \frac{u_lu_l}{2}$  denotes specific kinetic energy and standard notations are used for other flow variables and fluid properties.  $\tau_{ij}^{SGS}$  and  $h_i^{SGS}$  are the sub-grid terms arising from filtering the convective fluxes of u and u, respectively. In the energy equation for sub-sonic flows in OpenFOAM-v10 [34, 45], the analogous sub-grid term of u and the viscous-work term are neglected, likely because they approximately balance each other in such flows [34, 45]. The derivatives of u and u is other truncation errors. The filtered fluxes in an isothermal flow can be reasonably modeled as [34, 45]

$$\overline{\tau_{ij}} = 2\bar{\mu}(\widetilde{S_{ij}} - \frac{1}{3}\delta_{ij}\widetilde{S_{kk}}) \qquad \qquad \overline{q_i} = -\bar{\rho}\bar{\alpha}\frac{\partial \tilde{h}}{\partial x_i}$$
 (11)

here  $\alpha$  and k of air are treated as a constant in the isothermal flow being simulated and  $S_{ij}=\frac{1}{2}(\frac{\partial u_i}{\partial x_j}+\frac{\partial u_j}{\partial x_i})$  is the strain rate tensor. We use the classic k-equation transport model approach in OpenFOAM-v10 for closure of other sub-grid quantities. Here  $\tau_{ij}^{\rm SGS}$  and  $h_i^{\rm SGS}$  are modelled using eddy-viscosity/eddy-diffusivity hypothesis.

$$\tau_{ij}^{\text{SGS}} = \frac{2}{3}\bar{\rho}k_{\text{SGS}}\delta_{ij} - 2\bar{\rho}\nu_{\text{SGS}}(\widetilde{S}_{ij} - \frac{1}{3}\delta_{ij}\widetilde{S}_{kk}) \qquad h_i^{\text{SGS}} = -\bar{\rho}\frac{\nu_{\text{SGS}}}{Pr_{\text{SGS}}}\frac{\partial \tilde{h}}{\partial x_i}$$
(12)

$$\widetilde{K} = \frac{\widetilde{u_l}\widetilde{u_l}}{2} + k_{\text{SGS}} \tag{13}$$

with sub-grid Prandtl number,  $Pr_{\rm SGS}=1.0$  [46].  $k_{\rm SGS}=\frac{1}{2}(\widetilde{u_lu_l}-\widetilde{u_l}\widetilde{u_l})$  is sub-grid kinetic energy and  $\nu_{\rm SGS}$  is sub-grid kinematic viscosity.  $\nu_{\rm SGS}$  is modeled as

$$v_{\rm SGS} = C_K \Delta \sqrt{k_{\rm SGS}} \tag{14}$$

where, coefficient  $C_K=0.094$  and  $\Delta$  is filtered width for which cube-root-of-cell-volume,  $\sqrt[3]{V}$ , formulation with Van-Driest damping is used since this damping improves predictions in the vicinity of wall [47].

$$\Delta = \min(\frac{\kappa y}{C_S}D, \sqrt[3]{V}) \qquad \qquad D = 1 - e^{-\frac{y^+}{A^+}}$$
 (15)

here D is damping factor.  $A^+=26$ ,  $\kappa=0.41$ ,  $C_S=0.158$  are model constants [47] and y is the distance from wall. Finally, the transport equation of  $k^{SGS}$  for closure is

$$\frac{\partial \bar{\rho} k_{\text{SGS}}}{\partial t} + \frac{\partial [\bar{\rho} \widetilde{u_i} k_{\text{SGS}}]}{\partial x_i} = \frac{\partial}{\partial x_i} (\bar{\rho} (\nu + \nu_{\text{SGS}}) \frac{\partial k_{\text{SGS}}}{\partial x_i}) + -\bar{\rho} \tau_{ij}^{\text{SGS}} : \widetilde{S_{ij}} - \bar{\rho} C_e \frac{k_{\text{SGS}}^{3/2}}{\Delta}$$
(16)

where 
$$-\bar{\rho}\tau_{ij}^{\text{SGS}}:\widetilde{S_{ij}} = \bar{\rho}[\nu_{\text{SGS}}\{(\frac{\partial \widetilde{u_i}}{\partial x_j})^2 + \frac{\partial \widetilde{u_l}}{\partial x_j}\frac{\partial \widetilde{u_j}}{\partial x_i} - \frac{2}{3}(\frac{\partial \widetilde{u_l}}{\partial x_l})^2\} - \frac{2}{3}k_{\text{SGS}}\frac{\partial \widetilde{u_l}}{\partial x_l}]$$
 models the

production of  $k^{\rm SGS}$ . The last term in Eq.(16) models the destruction of  $k_{\rm SGS}$  with

coefficient  $C_e=1.048$  [47]. Readers are suggested to visit OpenFOAM-v10 documentation [48] and related resources for more details about the model.

The main boundary conditions (b. cs.) for the base-case simulation, consistent with the experimental flow conditions reported in [20], are summarized in table 1.

**Table 1.** Boundary conditions considered in the present study [20].

B. Cs.	$ar{p}$	ũ	Ĩ	k <sup>SGS</sup>
Inlet	Zero gradient	Turbulent inlet;	Fixed value;	Fixed value;
		$<\tilde{u}>_{noise-mean}=8.2$ m/s;	300 к	$10^{-5}  \mathrm{m^2/s^2}$
		turbulence intensity = 5%		
Outlet	Wave transmissive	Zero gradient	Fixed value;	Zero gradient
			300 К	
Wall	Zero gradient	No slip;	Fixed value;	Fixed value;
(every)		0 m/s	300 к	0 m <sup>2</sup> /s <sup>2</sup>

In the experimental setup [20], a choke plate was placed upstream of the domain that is computationally investigated in the present work to stabilize the mass flow rate entering the domain against acoustic fluctuations. We apply a velocity b. c. along with a zero-gradient pressure b. c. at the inlet to reproduce this effect numerically. Specifically, turbulentInlet fvPatch in OpenFOAM-v10 [49] is selected as the inlet velocity b.c., since apart from mean velocity it also imposes desirable spatio-temporal fluctuations to replicate turbulent characteristics of flow entering into the domain. The spatio-temporal

fluctuations are generated using a random number generator, which we set to yield a turbulent intensity (T.I.) of 5% in the present work. This value of T.I. is based on the empirical correlation  $T.I. = \frac{0.16}{Re_{inlet}^{1/8}}$  [50] since turbulent characteristics of flow entering the domain are not reported in related earlier publications [6-8, 20, 42]. Wave transmissive b. c. is employed for pressure at the outlet, following Poinsot and Lele [51], to minimize spurious reflection of wave into the computational domain. At the inlet, a quite small value is assigned to  $k^{\rm SGS}$  rather than zero to prevent the simulations from crashing [52]. The value of  $k^{\rm SGS}$  at the wall is set to zero since  $y^+ < 4.5$  in the mesh [53] across all the cases simulated in the present work. More details about the mesh are mentioned in the next section.

### 3.2. Numerical solver

The physical behavior of each term in the governing equations (GEs), Eqs. (8) - (10) and (16) in the present work, categorizes the numerical schemes appropriate for their FVM-discretization. A set of appropriate schemes are used for the collocated FVM-discretization in the present work, where each scheme is at least second order accurate. The use of higher order, sixth- or seventh-order, reconstructions is restricted from the employment of tetrahedral grid elements around the swirler to fully capture its geometrical details in the present computational mesh [54]. The temporal terms are discretized using the *pure Crank-Nicolson* scheme. The convective terms are discretized using the *van-Leer* interpolation scheme, owing to its TVD behavior that minimizes numerical dispersion arising from spatial-truncation errors. Gradients at cell nodes are

discretized using the *cell-limited least-squares* scheme. The *cell-limited* aspect ensures bounded interpolation of any variable to neighboring faces. The gradient of enthalpy at cell-faces in the FV integration of effective heat flux term, Eqs. (11) and (12), is discretized using a *central-difference* scheme. The scheme is augmented by a non-orthogonal correction, the *snGrad* scheme, in the regions of computational mesh with skewed elements. The mesh in the present case has a skewness below 0.8, and therefore only a limited correction is applied. The strain rate at cell-faces in the FV integration of effective stress tensor, Eqs. (11) and (12), is interpolated to adjacent cell nodes using a *linear* interpolation scheme. These strain rates are then discretized using the predefined gradient scheme, here it is the *cell-limited least-squares* scheme. Mass flux and fluid properties are interpolated to cell nodes using a *cubic* scheme and the *Rhie-chow* correction is applied to avoid pressure-velocity decoupling on collocated grid arrangement used in OpenFOAM-v10.

The resulting algebraic equations are solved using the rhoPimpleFoam solver, which is an integration of the PIMPLE algorithm with the iterative linear solvers appropriate for the discretized GEs. PIMPLE is a pressure-based, transient, segregated-algorithm suitable for compressible flows with  $Ma \leq 1$  [55]. It combines the inner-corrector loops of the PISO algorithm and the outer-corrector loop structure of the SIMPLE algorithm [55] to achieve fully converged solution at each timestep. Two inner-corrector loops—for pressure equation, flux and momentum corrections—five outer-corrector loops—for energy and turbulence equations along with momentum and density predictions apart from inner-loop content—and a non-orthogonality-corrector loop are used in the present

work. Please refer to OpenFOAM-v10 documentation [48] and [55] for more details about the solver. All the equations are solved with full relaxation (relaxation factor = 1.0) in the present work.

Usually, the above comprehensive solver, the along with numerical schemes, remains stable even if the maximum Courant number,  $Co_{max}$ , exceeds 1.0 [55]. However, enforcing  $Co_{max} < 1.0$  enhances temporal accuracy and boundedness of the solution, especially for boundedness with second and higher-order temporal schemes [56]. The timestep is accordingly constrained in the present work and more about it is discussed in the next section.

## 4. Computational grid, grid resolution and solver validation

Next, we describe the spatial mesh and timestep used to discretize the GEs in the present simulations. We use hexahedral mesh elements throughout the investigated computational domains, except in their swirlers—where tetrahedral elements are used to capture the geometric details. The mesh size and timestep are constrained by the LES requirement of resolving at least 80% of turbulent kinetic energy (TKE) locally [43]

Fraction of 
$$TKE_{resolved} = \frac{TKE_{resolved}}{TKE_{resolved} + k_{SGS}} \ge 0.80$$
 (17)

 $\text{here } TKE_{resolved} = \frac{<\widetilde{u}_i\widetilde{u}_i> -<\widetilde{u}_i><\widetilde{u}_i>}{2} \text{ and } <\cdot> \text{ denotes temporal mean}.$ 

Pope's criterion [43] for LES in an isotropic turbulence stipulates resolving eddies larger than one-sixth of the integral length scale  $l_0$ . It is valid up to  $R_\lambda \approx 1000$ , where  $R_\lambda$  is Re based on Taylor micro-scale.  $R_\lambda \approx 200$  in the present work based on the correlation  $R_\lambda \approx \sqrt{2Re_{inlet}}$  from [43] and considering  $l_0 \approx r_{inlet} = 19$  mm we get a cut-off eddy

size  $(l_0/6)$  of approximately 3.2 mm that requires a mesh size not larger than 1.6 mm for appropriate resolution. Conservatively, we limit the maximum cell edge length to 1.2 mm since our entire flow field would not be isotropic. Additional refinements are employed around the regions highlighted in figure 1c to resolve shear layers and wakes downstream of the swirler's center-body. The mesh is also refined in the near-wall region with the first node height of 0.04 mm from the wall, resulting in  $y^+ < 4.0$  in the base case and below 4.5 across all the investigated cases. Typically,  $y^+ \le 5.0$ , with lower computational requirement, is reasonable in LES for engineering applications [29, 53]. We do not attempt to resolve the region around swirler vanes owing to prohibitive computational costs. The smallest mesh element appears in the swirler of size 0.034 mm. Each swirl-combustor geometry investigated in the present work contain approximately 1.61 million mesh elements, respectively. The overall metrics of computational grids are, minimum orthogonality = 0.18, maximum aspect ratio  $\approx 25$  and maximum skewness = 0.8.

Time-step selection references the cut-off eddy time scale, which we estimate using the correlations in [43] to be approximately 1 ms. However, finer structures may appear in shear layer and the wake of the swirler's CB, whose resolution demands a smaller timestep—may be around, 0.05 ms. To evaluate physical consistency of the solution at this candidate timestep, we monitored  $Co_{max}$  using OpenFOAM-v10. The timestep of 0.05 ms yields  $Co_{max} >> 1.0$ . Reducing it to 2.50  $\mu$ s brought  $Co_{max}$  below 0.9 in all simulations performed in the present work.

The scaled residuals of all variables dropped below  $10^{-6}$  every timestep, before or in the fifth outer-corrector loop across all the cases simulated in the present work. The

convergence at each timestep is ensured by monitoring the variation of pressure and axial-velocity with iterations at two points within the computational domain. The flow-through times are approximately  $0.120\,\mathrm{s}$  in the investigated cases. The mean flow fields are obtained by averaging computational data over ten flow-through times, discarding the first three flow-through times.

Figure 1d shows a contour of the fraction of TKE-resolved in the base case, confirming more than 80% resolution in the regions of interest. Analogous contours for other investigated cases are presented in the subsequent sections.

## 5. Validation

To validate the developed comprehensive computational model, we first compare its temporal-mean predictions of the normalized axial-, radial- and tangential-velocity components with the corresponding experimental data reported in [20]. Figure 2 presents the radial distributions of these velocity components at four streamwise locations, where y denotes the distance downstream from the expansion plane. The present solver reproduces these radial-profiles with reasonable accuracy. Notably, it correctly captures the location of the upstream stagnation point of the IRZ in the mean flow-field, i.e., it accurately predicts the mean axial-velocity on the centerline at y/R = 0. This value was ill-predicted in simulation results of [20]. The experiments in [20] also report the presence of a precessing vortex core (PVC) with a frequency of 120 Hz [7] in the investigated isothermal flow. To determine the corresponding precession frequency in our simulated base flow, we perform a Fast Fourier Transform (FFT) on the time-series of the x-velocity

fluctuations. The velocity fluctuations are recorded for more than three flow-through times, sampled every 250<sup>th</sup> timestep, at a point on the domain axis located 5 mm upstream of the expansion plane. The resulting frequency spectrum in figure 3 exhibits a single sharp peak at 128 Hz, yielding a Strouhal number  $St = \frac{f \times d_{inlet}}{U_{inlet}} = 0.59$ . This value is an acceptable deviation from the experimental result, since certain geometrical and flow details are not reported in [7, 20]. The rationale for choosing this probe location will be evident in the *Results and Discussion* section of the present work.

Overall, the developed computational model reproduces both the mean flow field and its dominant unsteady dynamics with good fidelity. Having established this level of accuracy, we proceed with our computational investigation using the validated solver.

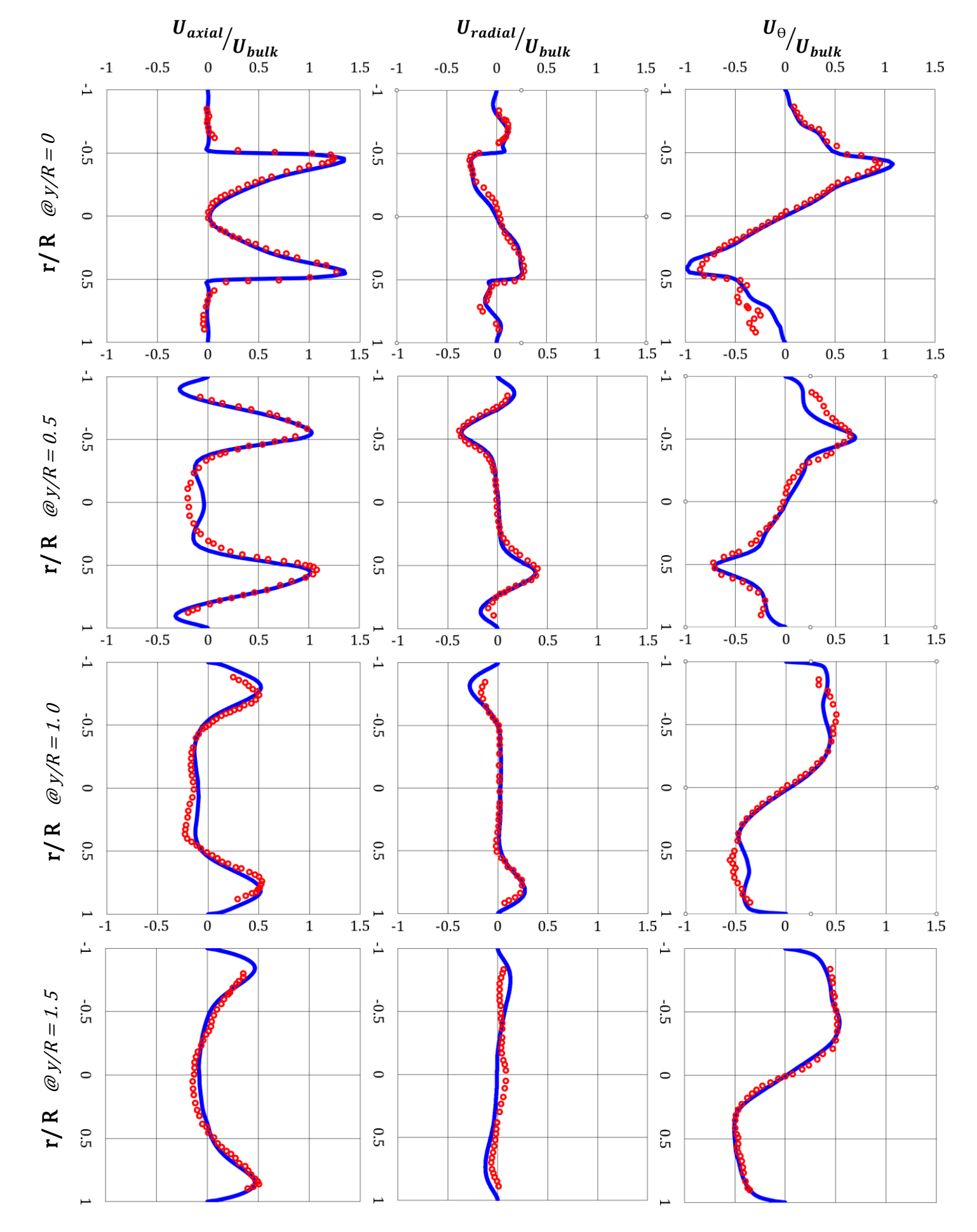
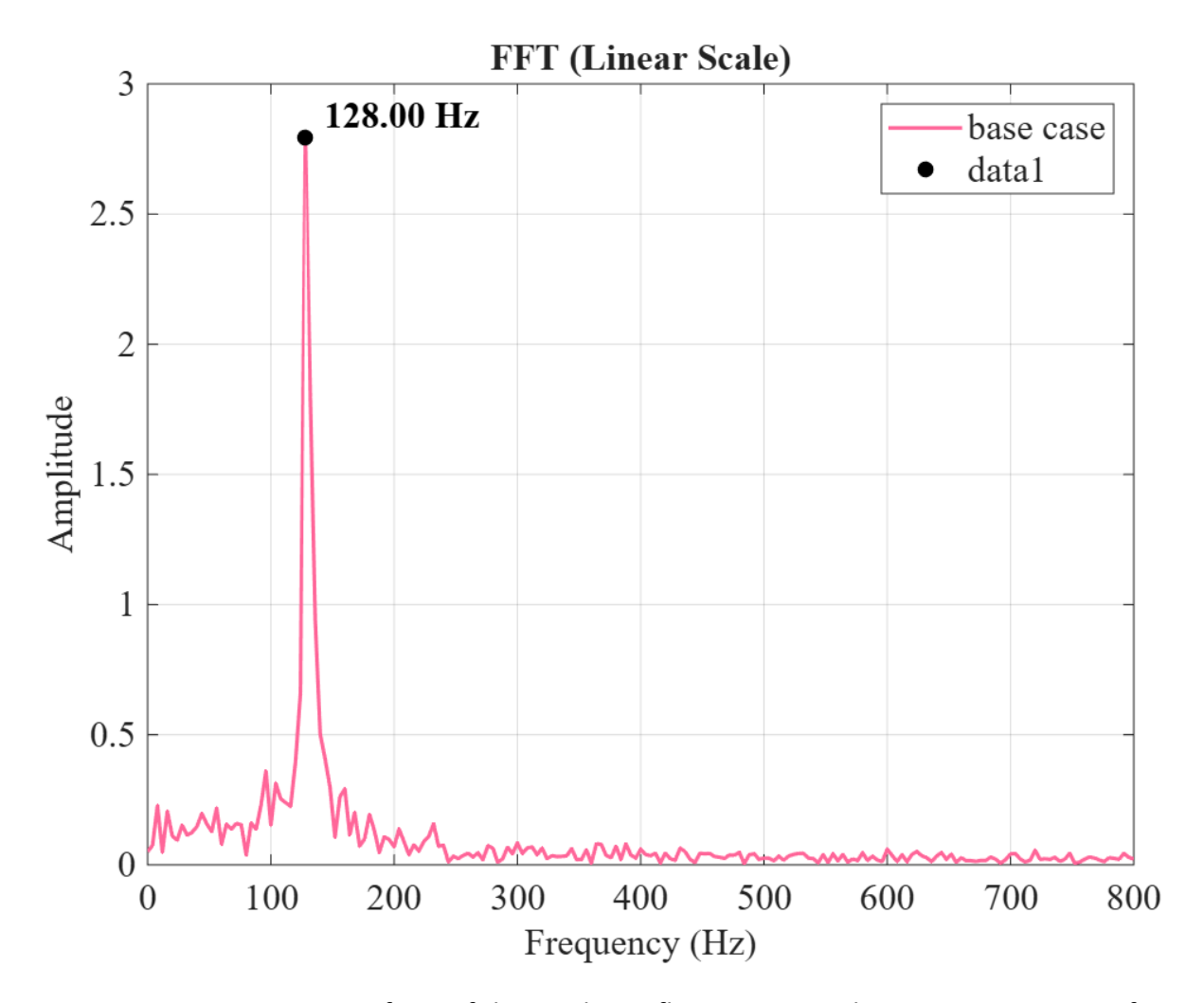


Figure 2. Radial plots comparing the experimental data [7, 20] (red circle) with numerical results (by line) of the present paper. y/R is the normalized location from the expansion plane and R is the radius before the expansion plane.



**Figure 3.** Fast Fourier Transform of the x-velocity fluctuations at the geometric center of the cross-stream plane located 0.115 m downstream from the inlet, i.e., 5 mm upstream of the expansion plane.

### 6. Results and Discussions

Apart from the base case that has a vane-angle of  $45^{\circ}$ , used in the validation studies, we simulate five additional cases with vane-angles of  $17^{\circ}$ ,  $25^{\circ}$ ,  $40^{\circ}$ ,  $50^{\circ}$  and  $60^{\circ}$  using the validated solver developed in the present work. All flow and other geometric parameters in these cases are identical to those in the base case, which is described in Section 2.

We assess the onset of VB in the investigated swirl combustor in Section 6.1 to quantify the corresponding critical swirl strength in terms of  $SN_q$  [Eq. (3)]. The onset of VB is identified by the disruption in coherency of a VC structure or by the appearance of IRZ(s). We inspect only the slices of IRZ(s) on a plane in the present work instead of its (theirs) full 3-D structure. These slices correspond to regions of non-positive axial-velocity in the core of a flow bounded by iso-contours of zero axial-velocity. These iso-contours are marked by black colour curves to easily locate the slices of IRZ(s) in the present work [57]. IRZ(s) typically start forming at very low swirl strengths but exhibit such high spatiotemporal intermittency until a critical swirl strength that they do not appear in the mean flow fields [58], which is undesirable for flame-stabilization. Hence, to identify flows in which VB possesses weak intermittency, stable-VB state [58], it is common to investigate IRZ formation in mean flow fields [58]. Accordingly, in Section 6.1, we determine the critical swirl strength by locating the first appearance of IRZ in the mean flow field. Next, using the data set from the present simulations we examine the degree of generality by which  $SN_q$  is more appropriate in representing swirl strength. Here we compare the axial variation of  $SN_q$  with other prominent SN formulations over the simulated cases. Further, based on the data, we address a group of queries on  $\mathit{SN}_g$  specified in the  $\mathit{Introduction}$ 

section of the present paper. In Section 6.2, we filter out the investigated cases in which the IRZ(s) forms but possess a high degree of spatio-temporal intermittency by investigating instantaneous flow fields.

Next, we determine the VC topologies forming in the investigated cases and their dynamics in Section 6.3. The VC in a swirl combustor is commonly visualized using the isosurface of a suitable Q-criterion value that coherently extends from the swirler through regions of elevated streamwise vorticity [20, 32, 38]. Q represents the second invariant of the velocity gradient tensor, Eq. (18) [38, 59]. Its appropriate value is case dependent.

$$Q = \frac{(trace(\nabla \vec{u}))^2 - trace((\nabla \vec{u})^2)}{2}$$
 (18)

Another commonly used quantity for vortex core visualization is the  $\lambda_2$ - criterion, where  $\lambda_2$  is the second largest eigen value of the tensor  $S^2 + \Omega^2$  with S and  $\Omega$  denoting the strain-rate and rotation-rate tensors [20]. This criterion has been reported to provide comparable or slightly improved accuracy relative to the Q-criterion [38]. However, the Q-criterion remains more popular for swirling flows and in general [32, 59]. To strengthen our choice, both criteria were applied to a randomly selected instant in each case, and the resulting iso-surfaces were found to be nearly identical for suitably chosen values. Hence, further use of the  $\lambda_2$ -criterion was deemed unnecessary for the present study. Here, we first visualize the VC structures at a few instances in our present work using the Q-criterion. However, the structures may decay or evolve over time, and therefore we examine the footprints left by the coherent dynamics of the VC over several timesteps to gain a preliminary assessment of the prevailing VC topologies. Finally, spectral methods

are employed to identify the dominant VC topologies and the temporal evolution of their coherent dynamics in greater detail.

## Spectral approach

We first perform a spatial cross-spectral analysis of axial-velocity fluctuations recorded for more than three flow-through times at two diametrically opposite locations on the footprints of VC's dynamics, as in [58, 60]. Let these two simultaneous time-series of axialvelocity fluctuations be denoted as X(t) and Y(t). The two point cross-spectral analysis isolates frequencies at which oscillations are phase-coherent between the two timeseries and quantifies their correlated energy [58, 60]. The data in each time-series is recorded at the sampling frequency  $(f_s)$  of 1600 Hz in the present work. Each time-series for the two-point cross-spectral analysis is split into 9 overlapping ensembles,  $N_e$ , of 128 samples each,  $N_{sea}$ , with 50% overlap between consecutive ensembles and a Hann window is applied on each ensemble to suppress spectral leakage around the peaks [60]. Accordingly, the frequency bin, discrete frequency slot, spacing,  $\Delta f = \frac{f_S}{N_{Sed}}$ , in the investigated cases is 12.5 Hz. We could not push  $N_{seg}$  to a higher value to sharpen the peak in the present spectral results due to resource constraints. However, we ensured lower variance in the present results with a reasonable number of ensembles [60]. The Hann window in discrete time is  $w[n] = \frac{1}{2} \left( 1 - cos\left(\frac{2\pi n}{(N_{seg} - 1)}\right) \right)$ ,  $0 \le n \le N_{seg} - 1$ . It reduces sidelobes, small leakage lobes next to a main peak, at the expense of a modest widening of the main lobe. Hence, peaks in some of the spectral figures in Section 6.3 appear slightly wider but with much lower leakage into neighboring bins. The cross-spectrum,  $S_{XY}(f)$ , is evaluated by Fourier transforms (DFTs computed using FFT algorithm) of X(t) and Y(t) on each overlapped ensemble, forming the ensemble-level cross-periodogram,  $X_r(f)Y_r^*(f)$ , and averaging these over all the ensembles r, see Eq. (19).

$$S_{XY}(f) = \frac{1}{N_e} \sum_{r=1}^{N_e} X_r(f) Y_r^*(f)$$
 (19)

here  $Y_r^*(f)$  is the complex-conjugate of  $Y_r(f)$ . The magnitude-squared coherence,  $\gamma_{XY}^2(f)$ , in Eq. (20) is a normalized measure of narrow-band phase consistency between the two time-series at any frequency f.

$$\gamma_{XY}^{2}(f) = \frac{|S_{XY}(f)|^{2}}{S_{XX}(f)S_{YY}(f)}$$
 (20)

here  $|S_{XY}(f)|$  is the magnitude of  $S_{XY}(f)$ . It reflects the corresponding correlated energy. A threshold of  $\gamma^2$  is widely used to sort out the coherent oscillations from the noise. Manoharan et~al.~[58] used it for the purpose in swirling jets where it performed well. Further, we quantify the azimuthal mode number, m, [58] associated with the resolved coherent oscillations to identify their azimuthal symmetry or the shape of the associated flow structure. The structure associated with these coherent oscillations in our setting would ideally be the VC since the probes of X(t) and Y(t) are positioned in the footprints of VC's coherent dynamics. Note that m=0 corresponds to axisymmetric oscillations, |m|=1 to single-helical oscillations and m=2 to double-helical oscillations. The azimuthal mode index (m) can be estimated from the unwrapped cross-phase,  $\Phi_{XY}(f)=arg\{S_{XY}\}$ , via  $m=\frac{\Phi_{12}(f)}{\Delta\theta}$ , as in [58]. Here  $\Delta\theta$  is the azimuthal separation between the

probes and  $\Delta\theta=\pi$  radian in the present case. Note that any two-point phase cannot distinguish m=0 from m=2 [58] and since VC structures up to m=2 exist in swirling flows [9], we adopt the four-probe azimuthal FFT analysis described next [61].

Azimuthal symmetry of coherent oscillations is resolved using the four simultaneous time-series,  $X_k(t)$  for k=1 to 4, collected at the four probes, each located at a different azimuthal angle  $\theta_k \in \{0,\frac{\pi}{2},\pi,\frac{3}{2}\pi\}$  radian but at the same radius. Two of these four locations are the same as in the two-point cross-spectral analysis. We use the same framing as in the two-point cross spectral analysis; 9 ensembles,  $N_{seg}=128,50\%$  overlap and Hann window; for splitting each time-series. We form short-time spectra, i.e., a windowed FFT on each overlapping ensemble for every probe. The FFT coefficient for each pair of frequency bin, f, and ensemble index, r, are stacked into a column vector  $z_r(f)$  shown in Eq. (21).

$$z_r(f) = [Z_1(f,r), Z_2(f,r), Z_3(f,r), Z_4(f,r)]^{\mathrm{T}}$$
(21)

Then, a  $4 \times 4$  cross-spectral matrix, S(f), is obtained by averaging the ensemble-level outer product of  $z_r(f)$  with itself, given in Eq. (22). S(f) distributes energy across azimuthal pattern at the frequency f through quadratic form in Eq. (22).

$$S(f) = \langle z_r(f)z_r(f)^{\dagger} \rangle_r \tag{22}$$

where (.)<sup>†</sup> denotes conjugate transpose and <.><sub>r</sub> denotes averaging over ensemble r. The projection of S(f) onto the discrete azimuthal basis,  $\{v_m\}$ , gives the modal energy distribution,  $E_m(f) = Re\{v_m^\dagger S(f)v_m\}$ . Here  $v_m$  is a complex column vector, given in Eq. (23), that represents ideal m-lobed patterns sampled at the four probe angles. Accordingly, the modal energy fraction, F(m, f), is as given in Eq. (24).

$$v_m = \frac{1}{4} [e^{-jm\theta_1}, e^{-jm\theta_2}, e^{-jm\theta_3}, e^{-jm\theta_4}]^{\mathrm{T}}$$
 (23)

$$F(m,f) = \frac{E_m(f)}{\sum_{m \in \{0,\pm 1,2\}} E_m(f)}$$
 (24)

F(m,f) identifies the energy distribution across modes at any frequency and so can be used to sort out the symmetry or flow structure that dominates at the frequencies where coherence,  $\gamma^2$ , is beyond a threshold value, coherent frequencies. We use  $\gamma_{XY}^2(f) \geq 0.7$  to identify coherent frequencies and F(m,f) at those frequencies indicates the dominant symmetry.

Next, we examine the temporal evolution of the coherent modes in the time domain for a selected pair  $(m_0, f_0)$ . We first form the modal time-series,  $c_m(t) = Re\{v_m^{\ \ t}x(t)\}$ , where  $x(t) = [X_1(t), X_2(t), X_3(t), X_4(t)]^{\mathrm{T}}$  and then use the Hilbert approach without segmenting the time-series. Specifically, we isolate the oscillation about the selected  $f_0$  by applying a narrow-zero-phase band-pass  $f_0 \pm 10.0$  Hz, a small band is a contiguous frequency interval, to get  $\widetilde{c_m}(t)$ .

$$\widetilde{c_m}(t) = \mathcal{B}_{f_0, 10.0}\{c_m(t)\} \stackrel{\text{def}}{=} \mathcal{F}^{-1}\{\mathcal{B}_{f_0, 10.0}(f) C_m(f)\}$$
 (25)

where  $C_m(f)=\mathcal{F}\{c_m(t)\}$  with passband  $[f_0-10.0~{\rm Hz},f_0+10.0~{\rm Hz}]$ . In practice we realize  $\mathcal{B}_{f_0,\Delta f}$  as a 4<sup>th</sup> order Butterworth band-pass in SOS, second-order sections, form with forward–backward filtering, zero phase. The analytic signal is then  $a_m(t)=\widetilde{c_m}(t)+j\,\mathcal{H}\{\widetilde{c_m}(t)\}$  where  $\mathcal{H}\{.\}$  is the Hilbert transform. The magnitude of  $a_m(t)$  is the modal narrowband amplitude (envelope),  $|a_m(t)|$ . The band-passed modal signal  $\widetilde{c_m}(t)$ , oscillatory trace, and the envelope  $\pm |a_m(t)|$  are plotted for the chosen azimuthal mode at the chosen frequency. The envelope  $|a_m(t)|$  shows the time-varying amplitude of

 $(m_0,f_0)$  at the native sampling resolution without ensemble averaging, while  $\widetilde{c_m}(t)$  depicts the oscillation itself at the frequency. The band-passed modal signal is sensitive to end effects caused by filtering. To mitigate these, we apply reflection padding to the modal scalar  $c_m(t)$  and a Tukey taper to the padded  $c_m(t)$  prior to filtering, then compute and apply a frequency-aware internal validity mask to the band-passed analytic signal  $a_m(t)$ , and finally trim 30 ms from each end of  $\widetilde{c}_m(t)$  and  $|a_m(t)|$  for presentation.

Furthermore, coherent oscillations with distinct m may be simultaneously present and interact. To assess this behavior, we compute the squared cross-bicoherence  $XX \to Y$  as in [62] on triads  $(f_a, f_b, f_c)$  with  $f_c = f_a \pm f_b$  using the same two-point time-series in cross-spectral analysis [58, 60]. The purpose here is to test whether two frequency bands in X(t) combine through quadratic coupling to populate a third frequency band observed in Y(t). This helps decide whether apparently separate spectral lines should be interpreted as mutually dependent rather than independent. We report only the squared cross-bicoherence corresponding to the permutation  $X_{fa}$  and  $X_{f_2}$  influencing  $Y_{fc}(t)$  in the frequency-domain  $b^2(X_{fa}X_{fb} \to Y_{fc})$ , since the squared cross-bicoherence for the reverse permutation  $b^2(Y_{fa}Y_{fb} \to X_{fc})$  showed similar values. The  $b^2(X_{fa}, \sigma X_{fb} \to Y_{fa+fb})$  is defined as

$$b^{2}(X_{f_{a}}, \sigma X_{f_{b}} \to Y_{f_{a}+f_{b}}) = \frac{|\langle X(f_{a})X(\sigma f_{b})Y^{*}(f_{a}+\sigma f_{b})\rangle|^{2}}{\langle |X(f_{a})X(\sigma f_{b})|^{2}\rangle\langle |Y(f_{a}+\sigma f_{b})|^{2}\rangle}$$
(26)

here  $\sigma$  can be +1 and -1. Two frequency bands taken from X(t) act as predictors and their effect is measured on the third band in Y(t). We evaluate the strength of quadratic interaction on both sum and difference triads and display them together on a signed

frequency layout. The  $f_2$ -axis is drawn positive for sum triads ( $f_a$  ,  $f_b$  ,  $f_a + f_b$  ) and negative for difference triads ( $f_a$ ,  $f_b \rightarrow |f_a - f_b|$ ).

Before proceeding to Sections 6.1, 6.2 and 6.3, we inspect figure 4 that presents contours of the fraction of TKE-resolved in the investigated cases. The results confirm over 80% resolution in the regions of interest, excluding the swirler vicinity and near-wall zones. Such resolution is considered appropriate in LES [63, 64] and has been shown to yield accurate results [63, 64]. Given these precedents and the validation of our numerical model in Section 5, we expect the simulations to adequately resolve the mean flow as well as the topology and dynamics of coherent structures in the investigated cases.

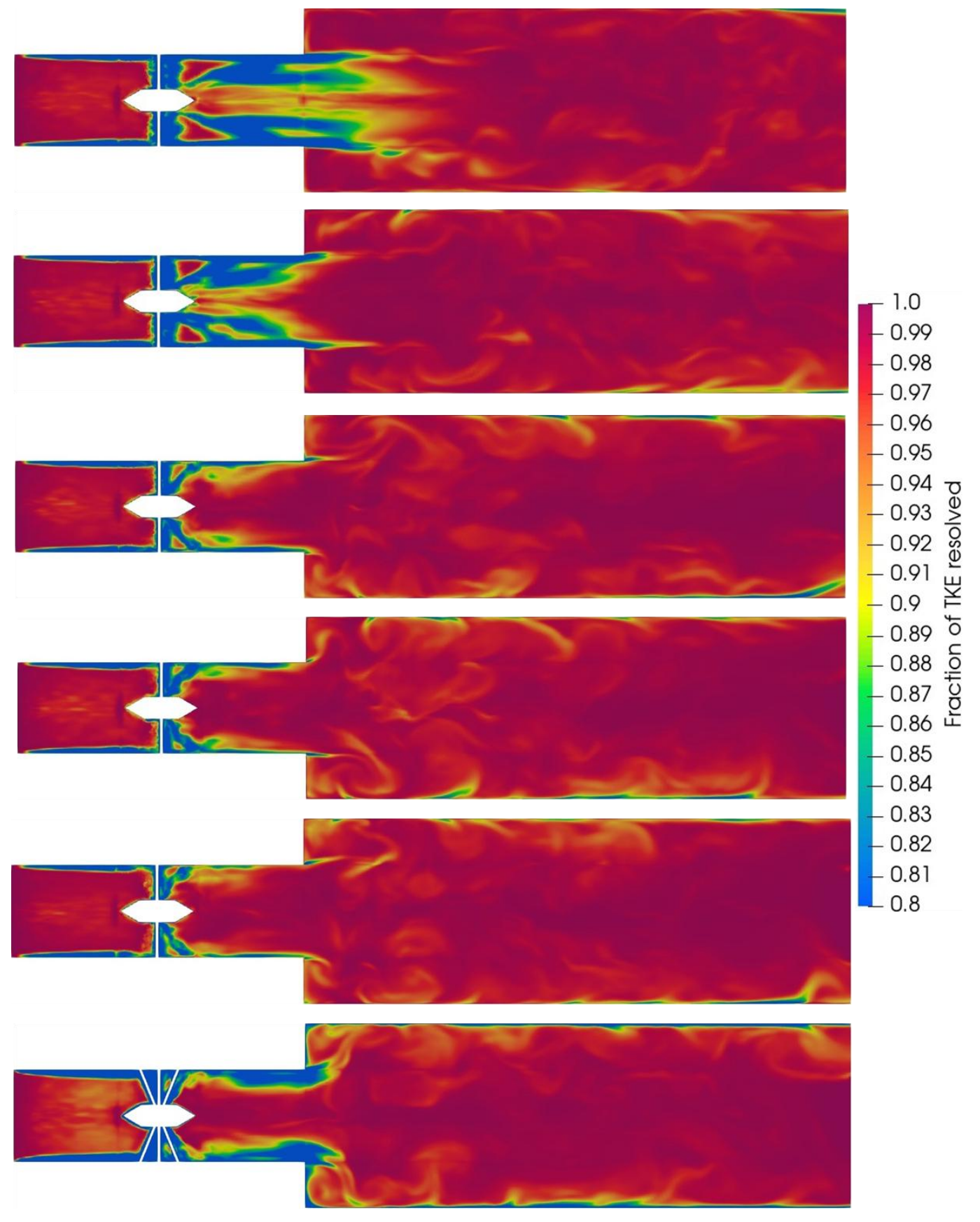
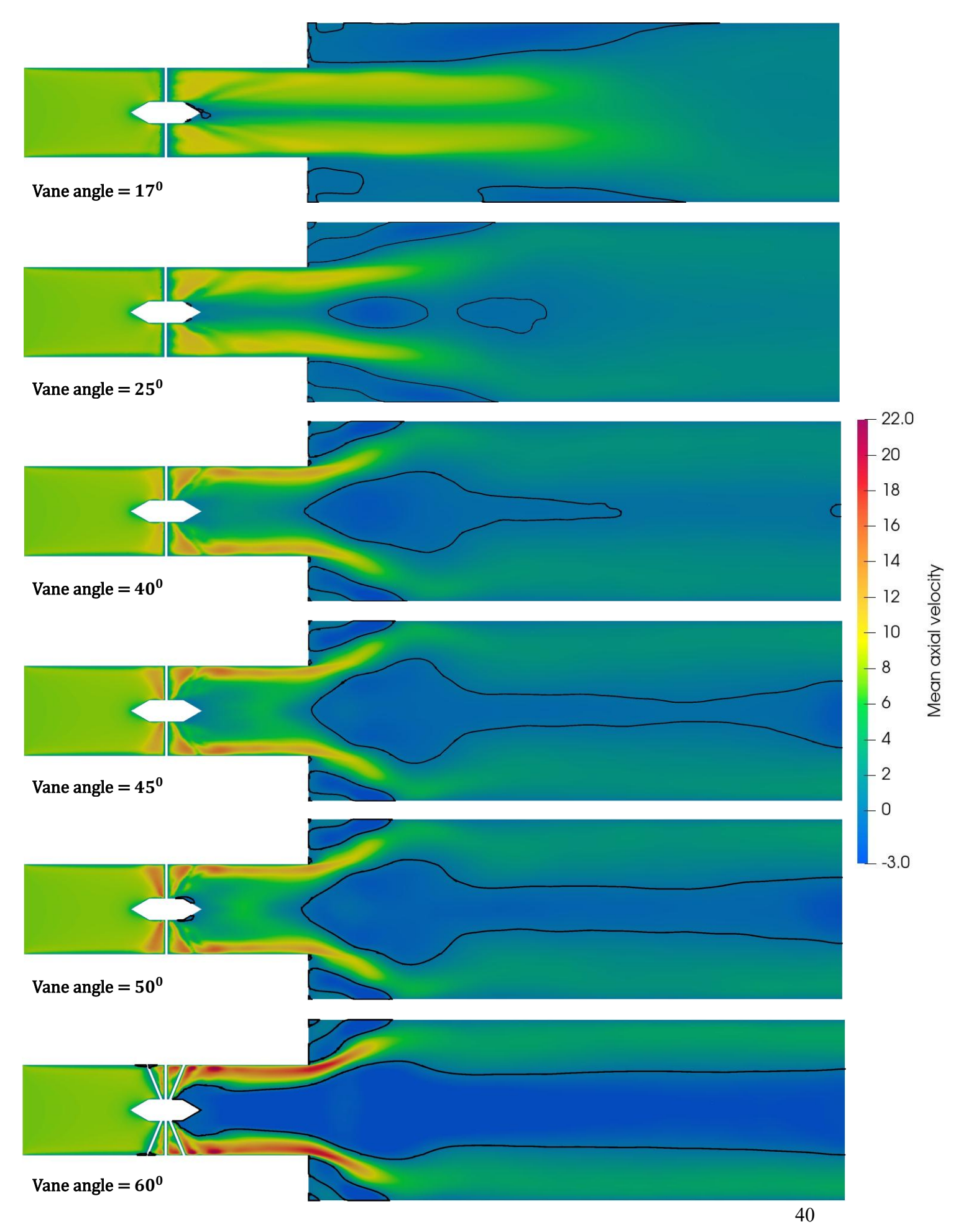


**Figure 4.** Contours of the fraction of resolved turbulent kinetic energy (TKE) for the cases with different swirler vane-angles. The resolved fraction is mostly greater than 0.8 in the core of the flow.

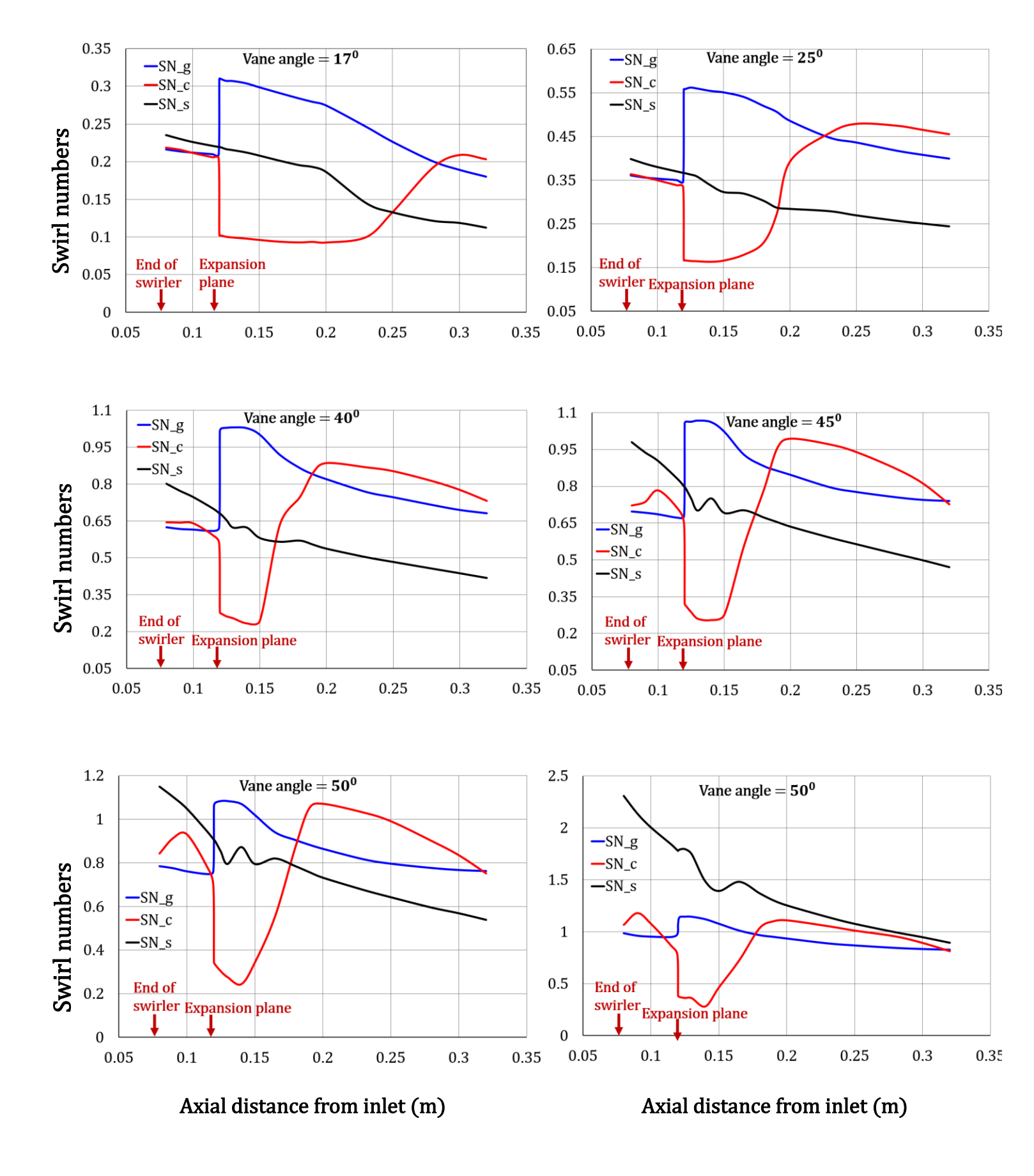
### 6.1. Onset of VB and most-suitable swirl number formulations

Figure 5 presents the contours of mean axial-velocity for the investigated cases with the boundary(ies) of IRZ(s) appearing as black color curves in the core of the domain. The presence of IRZ(s) in a mean flow indicates the occurrence of a stable-VB [57, 58]. It is evident from figure 5 that a stable-VB occurs in the investigated swirl combustor when the vane-angle equals or exceeds  $25^{\circ}$ . Accordingly, the onset of stable-VB in the swirl combustor seems to occur for a vane-angle between  $17^{\circ}$  and  $25^{\circ}$ . The IRZ spans across the larger-diameter section of the combustor for the vane-angle of  $45^{\circ}$  and the entire combustor length downstream of the swirler for the vane-angle of  $60^{\circ}$ .

Next, we analyze the streamwise variations of three swirl number formulations,  $SN_g$ ,  $SN_c$  and  $SN_s$  [Eqs. (3), (5) & (7)] for the investigated cases shown in figure 6. The aim is to assess which formulation best represents swirl strength. The reference pressure,  $p_{ref}$ , required to evaluate  $SN_g$ , Eq. (3), is selected based on the guidelines in [29]. Recall that an appropriate SN formulation should remain constant when viscous dissipation is negligible. Otherwise, it should exhibit a net decay along the flow, with weak variation rates, in a region of fixed cross-section away from flow transitions. Figure 6 shows that  $SN_g$  is nearly flat in the inlet tube for all the investigated cases. Downstream of the expansion  $SN_g$  decays monotonically; the decay rate is small sufficiently far downstream and becomes even smaller with increasing downstream distance. In contrast, the values of  $SN_c$  and  $SN_s$  vary significantly within each region of constant cross-section away from the expansion plane, with  $SN_c$  even showing non-monotonic variations. Their variation rates do not reduce appreciably with distance from the expansion plane.



**Figure 5.** Contours of mean axial velocity for the cases with different swirler vane angles. Black colour curves are isocurves of zero axial velocity.



**Figure 6.** Variations in the values of different swirl number definitions along the axial direction for the cases with different swirler blade angles in the geometry with expansion plane.

Hence,  $SN_g$  satisfies the criteria of an appropriate SN formulation for the investigated cases and therefore, its suitability in representing swirl strength in isothermal flows appears broader than that established for the single case in [29]. The inconsistent behaviour of  $SN_c$  and  $SN_s$  arises from the simplifications adopted in their respective formulations, as discussed partly in the *Introduction* and elaborated in [29]. The weak variation rates in the values of  $SN_g$  in the inlet tube and at locations far downstream provides flexibility in the location of its measurement within these regions. Vignat et al. [29] did not specify the distance of the second region from the expansion plane. Figure 6 in the present work shows that the distance of this region increases as the vane-angle decreases. We do not pursue a detailed analysis here because measuring  $SN_g$  in the inlet tube provides a more robust and practical quantification of swirl strength and it is discussed in the next paragraph.

Here, we compare the  $SN_g$  profiles for the vane-angle of  $60^0$  shown in figure 6 and the case studied in [29]. It is apparent that the values of  $SN_g$  in the inlet tube of these cases are approximately 1, while its values in the downstream sufficiently away from the expansion differ considerably. This implies a dependence of the  $SN_g$  values in the downstream region on ER and  $Re_{inlet}$ , which are significantly different between the two cases. Accordingly, using the downstream value of  $SN_g$  for comparing different combustors can obscure the differences caused by these parameters. Therefore,  $SN_g$  should be measured in the inlet tube of the combustor, i.e., in the region upstream of the expansion plane.

Moreover, the value of  $SN_g$  changes only marginally within the inlet tube in all the cases shown in figure 6. This behavior is attributed to the short length of the inlet tube [29]. If the inlet tube would have been long, measuring  $SN_g$  at widely spaced axial positions among cases with different vane-angles may lead to incorrect comparisons. Figure 6 indicates that measuring  $SN_g$  within a short region, no more than 40 mm (it may depend on  $\frac{L}{D}$  of inlet tube and weakly on  $Re_{inlet}$ ), just downstream of the swirler provides a suitable measure of swirl strength. Consistency in the measurement location, even with this degree of flexibility, appears sufficient to ensure meaningful comparisons across cases. Consequently, the values of  $SN_g$  measured within 40 mm downstream of the swirler in the inlet tube are 0.21, 0.35, 0.61, 0.69, 0.77 and 0.98 for the swirl combustor cases with vane-angles of  $17^0, 25^0, 40^0, 45^0, 50^0$  and  $60^0$ , respectively. Referring to the earlier discussions, the critical value of  $SN_g$  for the onset of stable-VB in the investigated swirl combustor lies between 0.21 and 0.35.

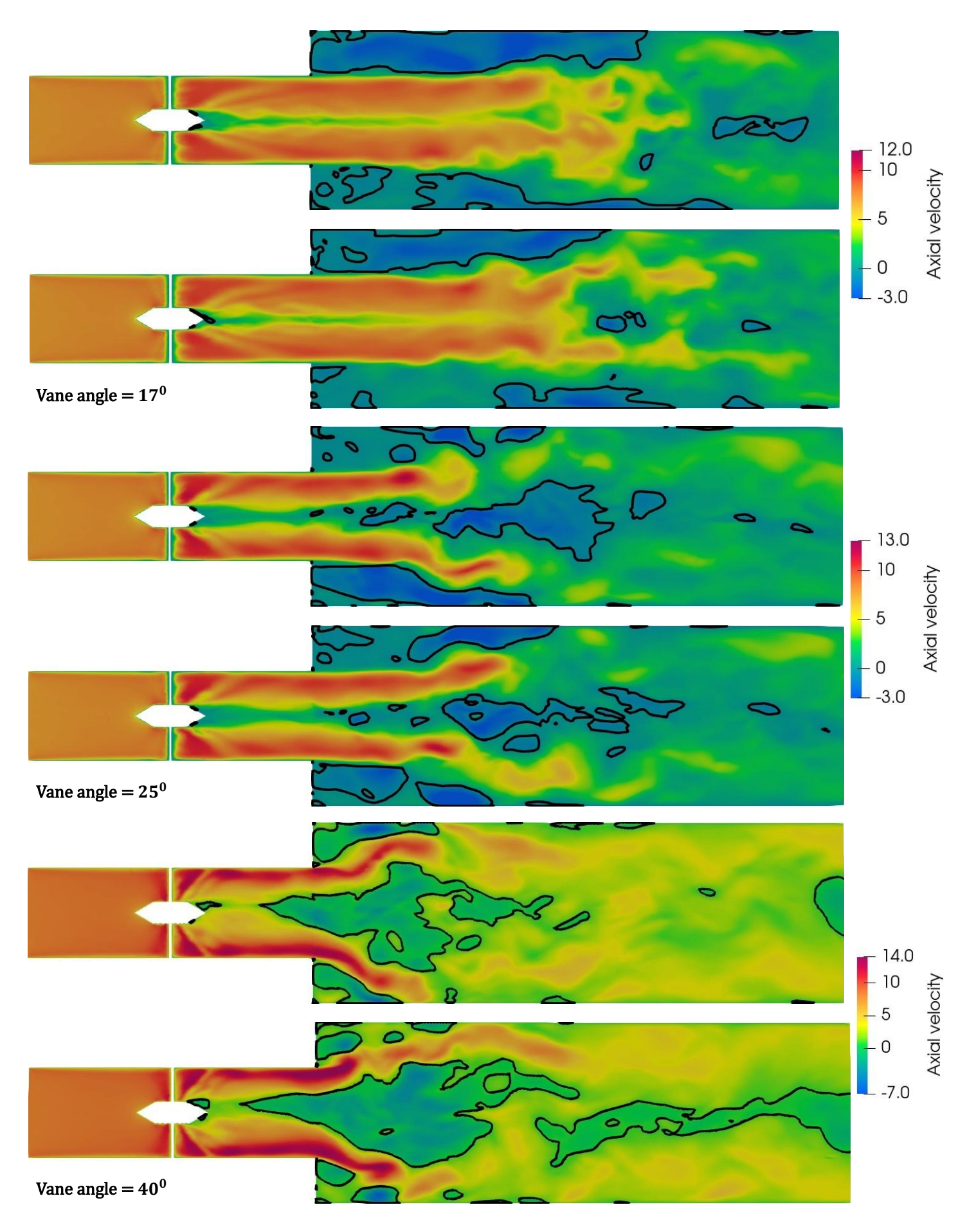
A numerical study of the dependence of this critical value of  $SN_g$  on ER and  $Re_{inlet}$  would require simulations over a wide range of these parameters. However, LES at higher inlet Reynolds numbers are computationally expensive and beyond our available resources. Hallets and Towes [40], instead of numerical simulations, adopted an experimental approach to examine the dependence of the critical value of  $SN_s$ , measured in the inlet tube, on ER and  $Re_{inlet}$  for  $Re_{inlet} \leq 1.6 \times 10^5$ . They reported only a weak dependence for  $ER \geq 1.5$  and  $Re_{inlet} \geq 10^4$ . Given our computational limitations, and in the absence of an experimental setup, we rely on reasoning and trends observed in our available simulations to infer the expected behavior of  $SN_g$  under similar conditions.

Figure 6 shows the profile of  $SN_s$  for the case with a vane-angle of  $25^0$ , in which the stable-VB state first appears in the swirl combustor. This profile in the inlet tube is nearly flat. Suppose its slope is relatively insensitive to ER and  $Re_{inlet}$  in the range  $ER \geq 1.5$  and  $10^4 \leq Re_{inlet} \leq 1.6 \times 10^5$ . Then a weak sensitivity of critical  $SN_s$  reported in [40] would suggest that the onset of VB in the present configuration occurs at roughly the same swirler angle. Subsequently, if the slope of  $SN_g$  curve in the inlet tube also varies weakly with  $Re_{inlet}$  and ER within their ranges given above, then the critical value of  $SN_g$  would also exhibit only a weak dependence on these parameters. The latter insensitivity is expected, as the slope of  $SN_g$  curve in the inlet tube of the present cases closely matches that observed in [29], despite significant differences in ER and  $Re_{inlet}$  between the configurations.

In conclusion,  $SN_g$ , the generic swirl number formulation for isothermal flows, exhibits streamwise variation consistent with the theoretical expectations. It remains nearly constant in the short inlet-tube of swirl combustors and is ideally suited for quantifying swirl strength through its values measured just downstream of the swirler. When such values of  $SN_g$  are used for comparing swirl strength across different flows, the likelihood of physically incorrect conclusions is minimized. The critical value of  $SN_g$  for the onset of stable-VB in the investigated swirl combustor lies between 0.21 and 0.35, and is expected to exhibit only weak sensitivity to ER and  $Re_{inlet}$  for  $ER \geq 1.5$  and  $10^4 \leq Re_{inlet} \leq 1.6 \times 10^5$ . Next, we investigate the VC structure and its dynamics in the investigated cases.

## 6.2. Vortex breakdown states

Figure 7 presents axial-velocity fields at two randomly selected instances after ten flowthrough times for the investigated cases. Black curves along the core of a flow represent the boundary of the slices of instantaneous IRZ(s). The IRZ in the smallest vane-angle case in figure 7 appears as a small pebble and displays high spatio-temporal intermittency across the two shown instances. Because of this level of intermittency, no IRZ appears in the corresponding mean flow field in figure 5. The observed flow corresponds to the near-VB state of [58]. The slices of IRZ(s) in the other cases display an overall weak intermittency across the instances shown in figure 7. Further, the recirculation bubble emanating from outlet appears strongly interacting with the recirculation bubble near the expansion in cases with vane-angles equal to or greater than  $45^{\circ}$ . A separation bubble appears attached to the downstream portion of the CB of swirler across the instances shown in figure 7. However, a high intermittency in the location of separation bubble in the cases with  $40^{0}$  and  $45^{0}$  vane-angle leads to its absence in the corresponding mean fields in figure 5. The above-mentioned recirculation bubbles forming near the expansion plane and the outlet merge smoothly with each other and the separation bubble in the largest vane-angle case. It results in an IRZ expanding over the length of combustor downstream of swirler. These swirl combustor flows except the smallest vane-angle flow correspond to the steady-VB state.



**Figure 7a.** Contours of axial velocity at two instances for the cases with  $17^0$ ,  $25^0$  and  $40^0$  vane angles. By ack colour curves are isocurves of zero axial velocity.

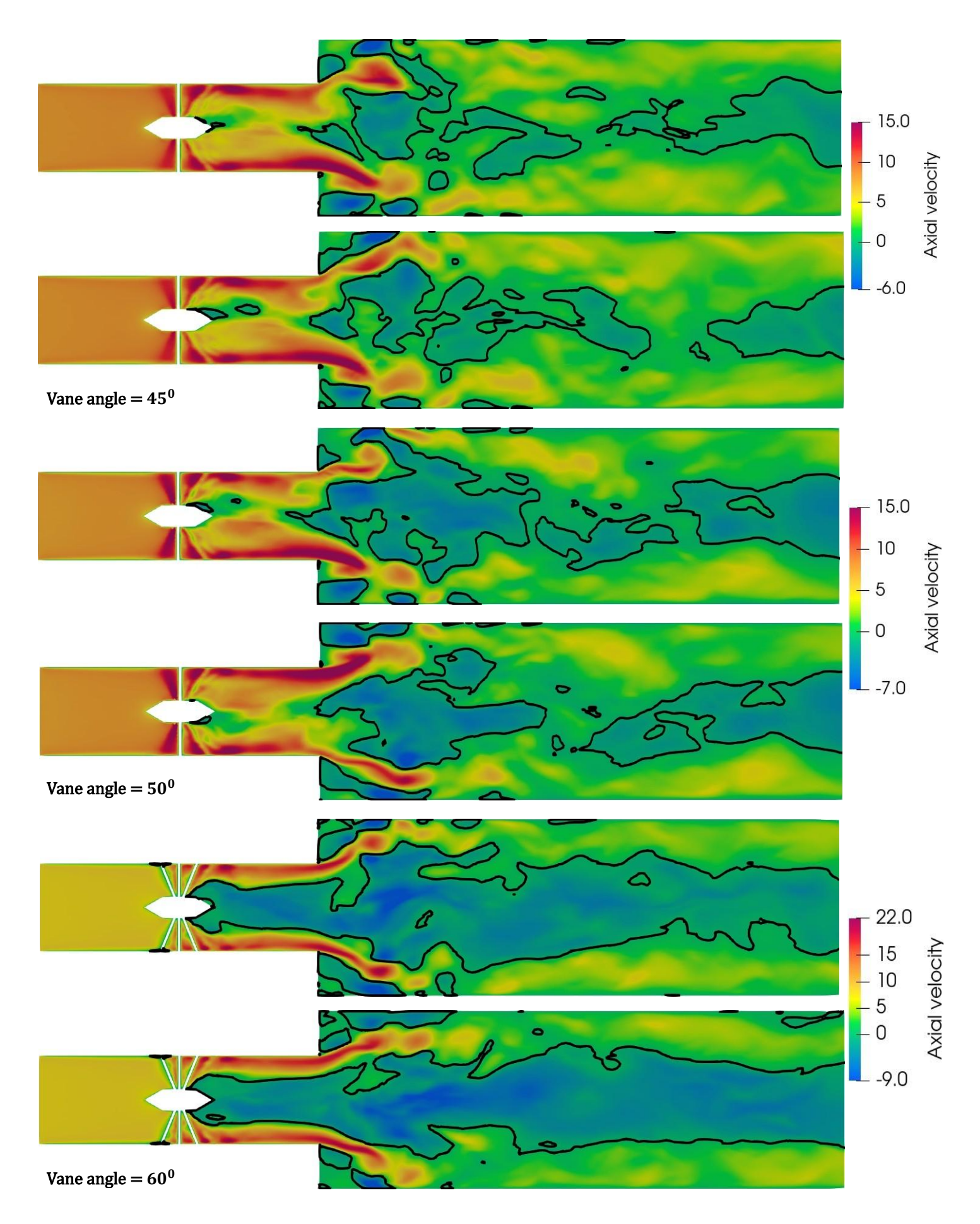


Figure 7b. Contours of axial velocity at two instances for the cases with  $45^{\circ}$ ,  $50^{\circ}$  and  $60^{\circ}$  vane angles 4B lack colour curves are isocurves of zero axial velocity.

## 6.3. Topology of vortex core and its dynamics

As stated earlier, in this section, we first visualize the VC structures at few instances and then evaluate their temporal evolution over several timesteps to assess their sustainability or transformations. Further, we locate and identify the response of inner shear layer and outer shear layer to VC dynamics, when need arises.

#### A. Topology of Vortex core

Figure 8 shows iso-surfaces of the Q-criterion for the investigated cases, except  $50^{\circ}$  vaneangle case for brevity. Here the Q-value, which differs between cases, isolates an ensemble of flow structures of which a coherent structure is expected to correspond to the VC. The suitable Q-value is identified using trial-and-error. Lowering the value by ten percent produced a proliferation of small iso-surfaces apart from coherent structures, whereas increasing it by ten percent led to fragmentation of the expected coherent VC structure. Recall that the VC in a swirl combustor corresponds to the particular iso-surface of a suitable Q-value that coherently extends from the swirler through regions of elevated streamwise vorticity [20, 32, 38].

A coherent Q iso-surface with two helical strands twisted in the same sense appears to emanate from the swirler in each of the flow fields in figure 8. More specifically, the two helical strands appear to emanate from the CB of the swirler in the cases with vane-angle  $< 60^{\circ}$ . These strands twist in the direction opposite to the rotation of the flow, as evident from comparing their twists with the inclination of swirler-vanes in figure 8. The strands in the largest  $(60^{\circ})$  vane-angle case have elliptically deformed

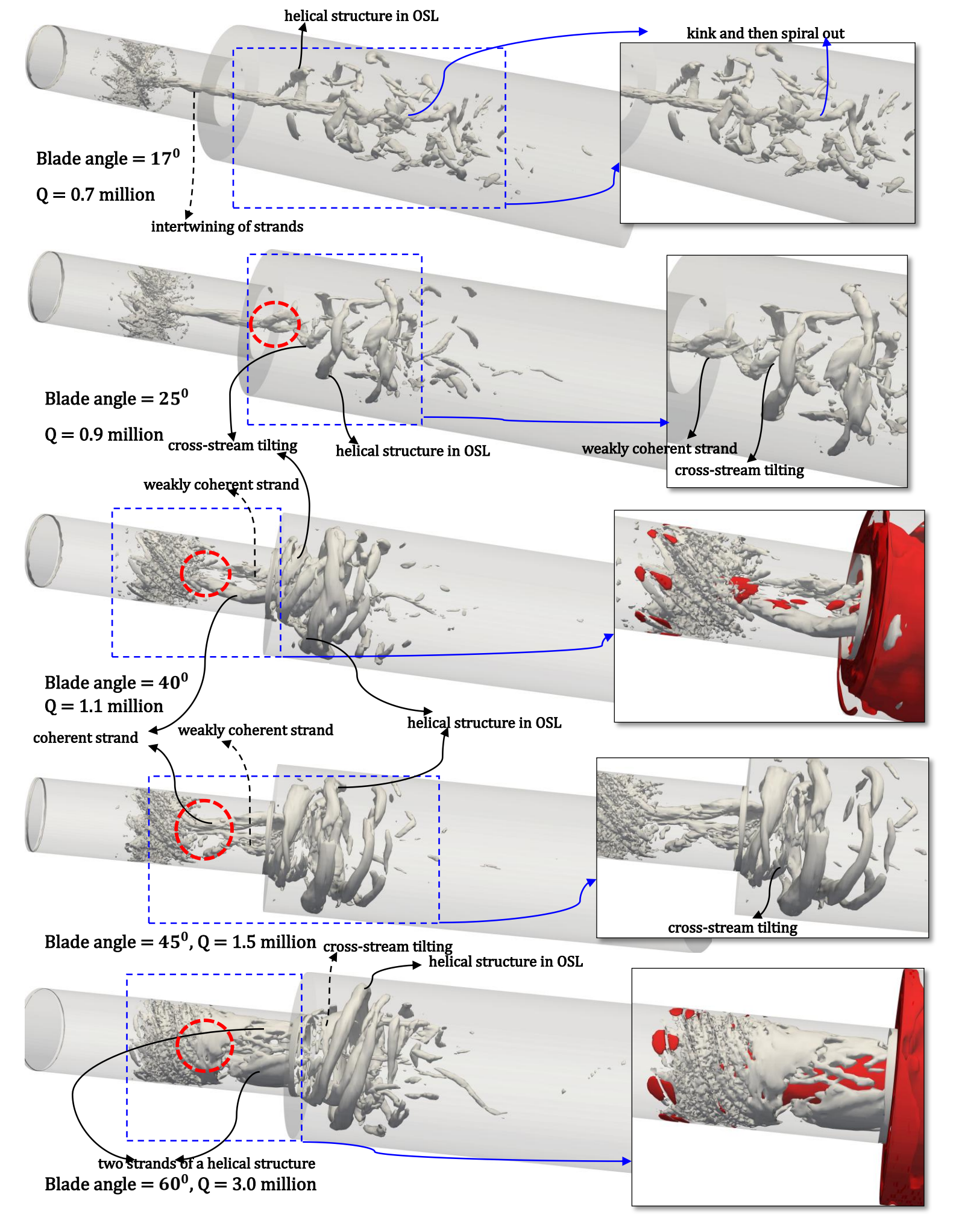


**Figure 8.** Iso-surfaces of Q-criterion (**grey**) and zero axial velocity (**red**, shown only in two cases) for the cases with different vane angles.

cross-sections. The two strands in the cases with vane-angle of  $17^{0}$  and  $25^{0}$  in figure 8 first intertwine up to some downstream distance from the swirler and then separate out. One of the strands kinks and coherently spirals out into a larger helix after separation in both the cases. The other strand disappears immediately after separation in the former case, while it persists for a short distance after separation in the latter case but with a poor coherency. This aspect is marked in figure 8 and is shown later in this section with better clarity.

The two strands in the other investigated cases shown in figure 8 separate out from or just after the swirler and then interlace. One of the two strands appears only weakly coherent in these cases except for the largest vane-angle case. A dashed red-color circle highlights the separation region of the two strands in all cases except the smallest (17°) vane-angle case, where the region is already clouded by proliferation of smaller isosurfaces. Note that the shown coherent structure expected to represent VC breaks down even in the smallest vane-angle case, where the flow corresponds to the near-VB state, as discussed earlier.

Vortical structures in the region outside the core of the flow after expansion appear tilted towards the cross-stream. They are coherent in the investigated cases except for the two smallest vane-angle cases. Similarly, the coherent strand of the double helix structure, in the core of investigated flows, begins to tilt towards the cross-stream just after the expansion plane except for the smallest vane-angle case. On the other hand, the weakly coherent strand does not tilt and dissipates within a short distance from the beginning of this tilting of the coherent strand. The tilting of the coherent strand in the

smallest vane-angle case occurs further downstream in figure 8. Note that both strands appear coherent in the largest vane-angle case in figure 8. They both tilt towards the cross-stream after expansion, unlike the other investigated cases. Although we have isolated the cross-stream tilting of the coherent strand of the double helix structure by markings, observing the disappearance of the weakly coherent strand in figure 8 is difficult for many cases. Later in figure 12 we present both these aspects clearly.

Although a double helix structure appears to represent the VC in each investigated case in figure 8, a closer examination of these structures discussed above reveals that only one of their strands is coherent, except in the largest vane-angle case. The observed difference in coherency between the two strands indicates a possible difference in their origin/formation. Only the coherent strand can be expected to represent the VC, since VC is a characteristic of swirling flows and loses coherency downstream of the VB region.

As mentioned at the beginning of this section, the next check for these strands to be a part of the VC is whether they pass through regions of high streamwise vorticity; the converse may not be true. Figures 9 to 11 present the slices of the Q-surfaces of figure 8 as white-color curves over the contours of streamwise vorticity on a cross-stream plane at three different instances. The plane is at a distance of 0.115 m from the inlet for the cases with vane-angles equal to or greater than  $40^{\circ}$ . This plane lies within the inlet tube, where the Q-surfaces of figure 8 only include the double helix structure, and the other corresponding structures are visible only after expansion. Accordingly, the white-color curves on the selected planes in figures 10 and 11 arise only from slices of the double helix structures of figure 8. The plane in the two smallest vane-angle cases is positioned

downstream of the separation of the double helix strands so that the slices of the two strands are distinguishable. Accordingly, the planes in figure 9 are at the distance of 0.200 m and 0.130 m from the inlet for the cases with vane-angles of  $17^{0}$  and  $25^{0}$ , respectively. Since these planes are located after expansion, the white-color curves on them arise also from the Q-surfaces located away from the core of the flow in figure 8 that are not a part of the double helix coherent structure. The slices in the core of these planes arise from the double helix coherent structure.

These white-color curves arising from the double helix structure on the selected planes appear to pass through regions of higher streamwise vorticity at all the shown instances in figures 9 to 11. However, it is apparent that the eccentricities of the two strands of the helix are not the same in the investigated cases except in the largest vaneangle case. The double helix structure in the two smallest vane-angle cases in figure 8 appears close to the centerline before its strands separate. One of the strands disappears, while the other, coherent strand, kinks and spirals outward after the separation. Accordingly, this coherent strand intersects the selected plane in figure 9, positioned downstream of the separation, at an eccentric location. Similarly, the slice of one of the strands of the double helix structure in the other cases, except the largest vane-angle case, appears on a smaller circle, marked in blue-color, while that of the other strand appears on a larger circle, marked in pink-color, in figures 10 and 11. The markings are shown only for one instance to avoid overshadowing of the clarity of other features in figures 10 and 11. Even the slice of one of the two strands has poor coherency. These traits are not typical of a double helix VC topology. Note that slices of both the strands are located at similar eccentricities in the largest vane-angle case.

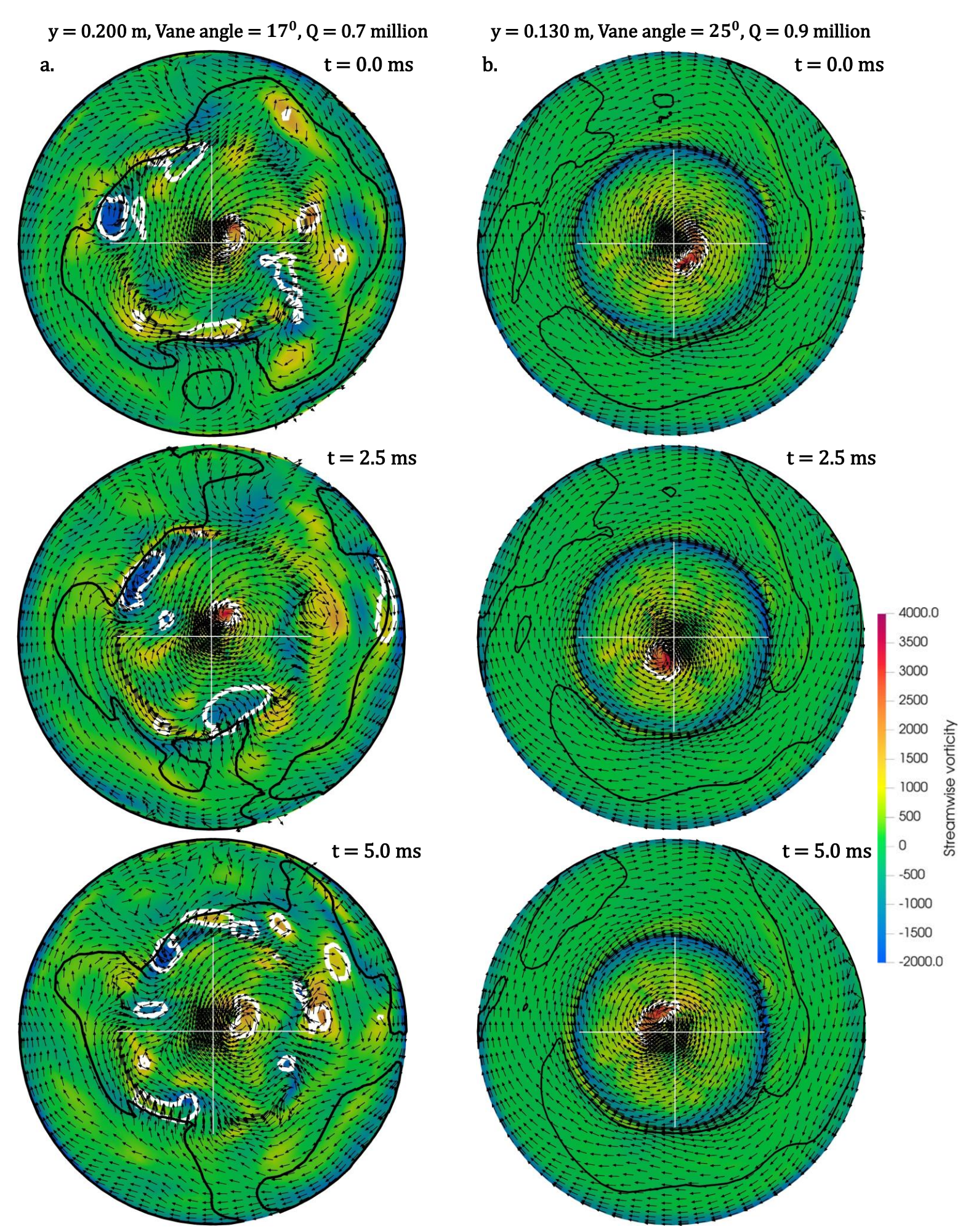


**Figure 9.** Contours of streamwise vorticity, projected velocity vector, zero-axial-velocity isocurves (**black**) & Q-isolines (**white**) on a cross-stream plane for the cases with  $17^0$  and  $25^0$  vane angles at three different instances, showing the relative VC, geometric-centre & negative axial-velocity zone. 'y' is the distance of plane from the inlet.

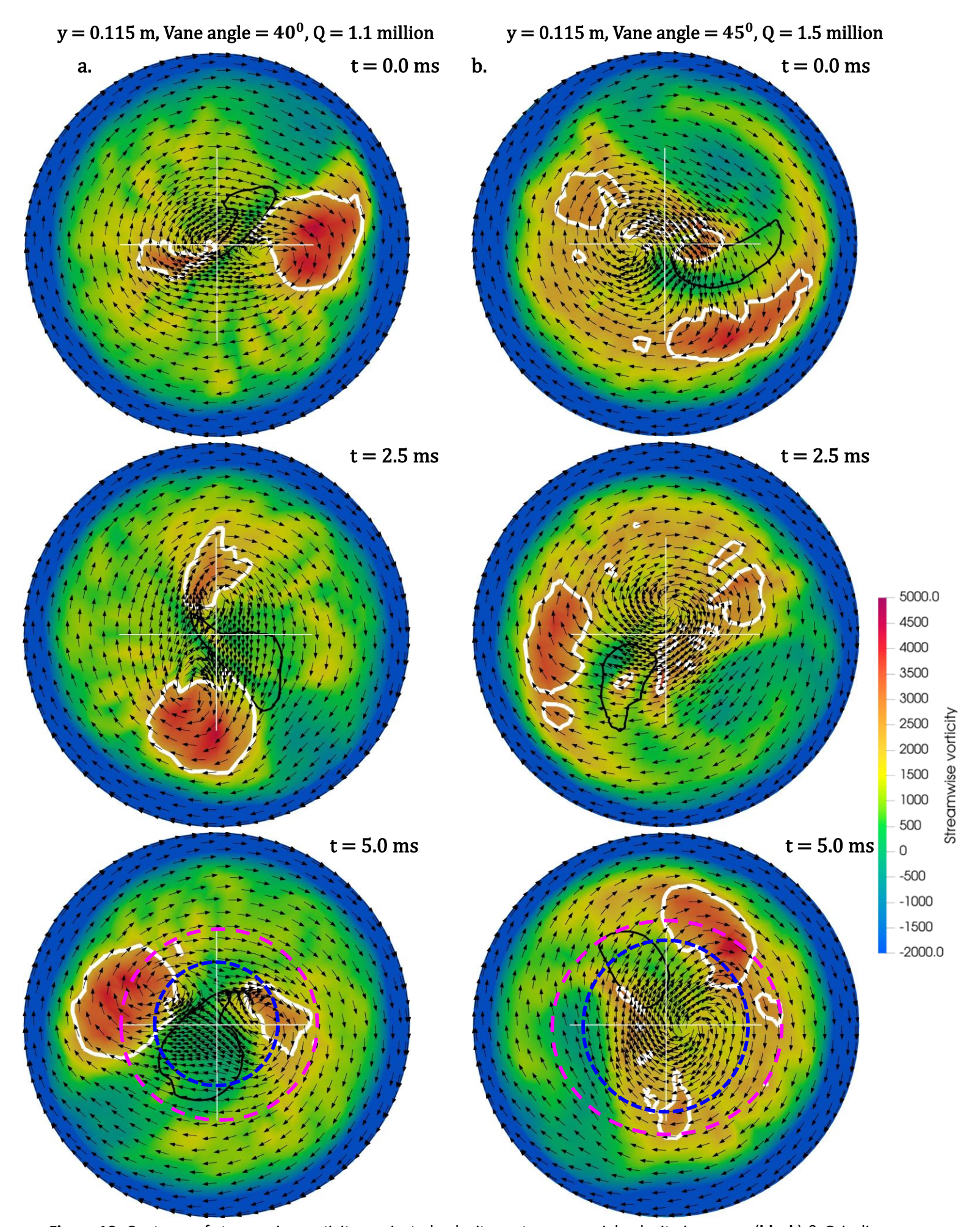


**Figure 10.** Contours of streamwise vorticity, projected velocity vector, zero-axial-velocity isocurves (**black**) & Q-isolines (**white**) on a cross-stream plane for the cases with  $40^{\circ}$  and  $45^{\circ}$  vane angles at three different instances, showing the relative location of VC, geometric-centre & negative axial-velocity zone. 'y' is the distance of plane from the inlet.

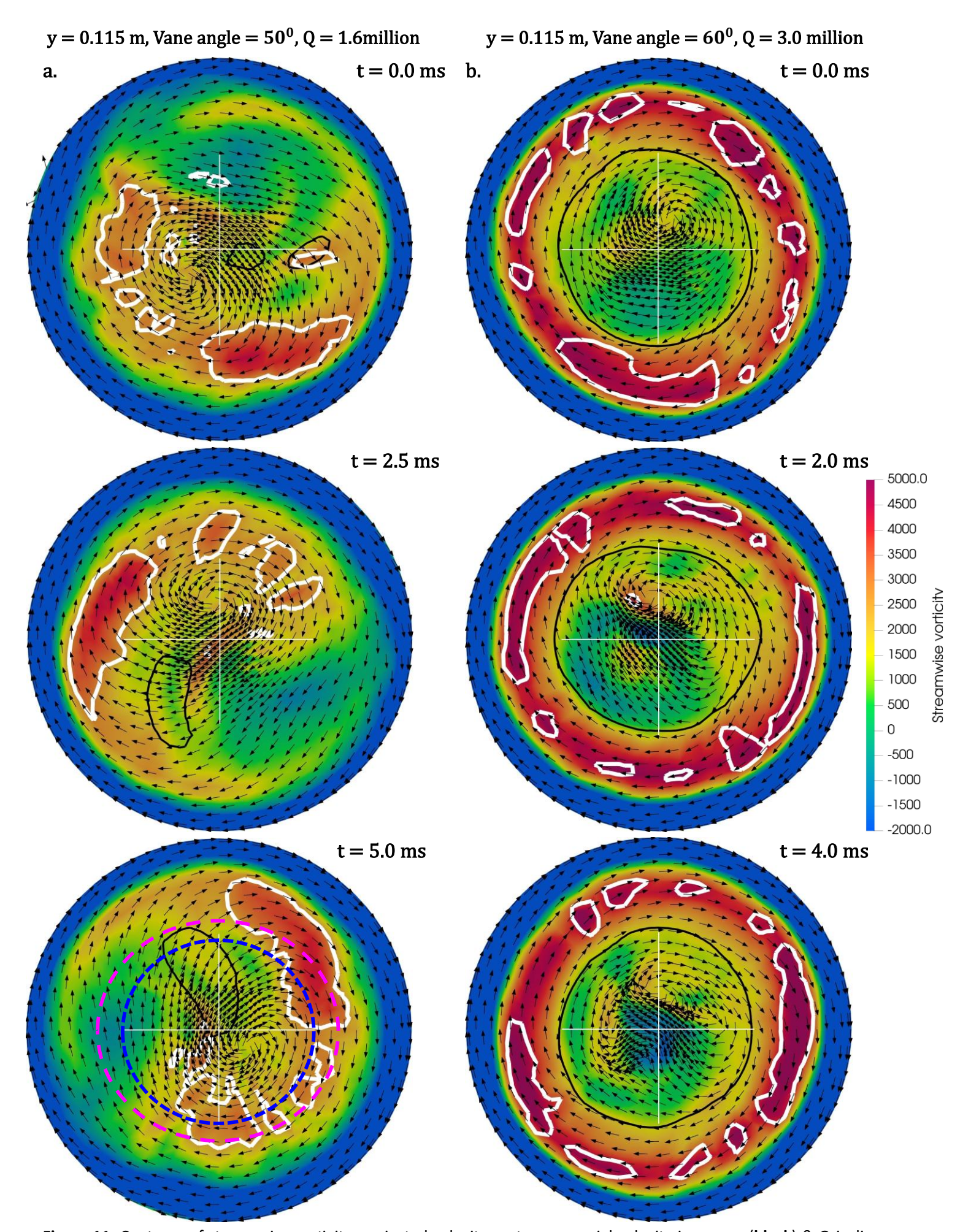


**Figure 11.** Contours of streamwise vorticity, projected velocity vector, zero-axial-velocity isocurves (**black**) & Q-isolines (**white**) on a cross-stream plane for the cases with  $50^{\circ}$  and  $60^{\circ}$  vane angles at three different instances, showing the relative VC, geometric-centre & negative axial-velocity zone. 'y' is the distance of plane from the inlet.

#### B. Relative position of ISL, OSL and VC

To resolve the dilemma of weakly coherent strand being a part of the VC, we investigate the origin of the two helical strands forming in the core of the flow fields in figure 8. However, we first present the two strands in a simplified manner in figure 12 so the flow aspects that could not be clearly presented in figure 8 are evident now. Figure 12 shows two images for each of the investigated cases. The right-hand images show Q-surfaces of figure 8 and black-color curves representing the outlines of recirculation zones over the contours of cross-stream vorticity, while two zig-zag dashed lines appear instead of the Q-surfaces in the left-hand images. Each zig-zag line connects the regions where the corresponding strand of the double helix structure in the investigated flow intersects with the plane in view in figure 12. The blue-color zig-zag lines correspond to the weakly coherent strands, and the white-color zig-zag lines correspond to the coherent strands. The left-hand images show that the weakly coherent strand in each case disappears within a shorter distance from the swirler than its corresponding coherent strand. The weakly coherent strands disappear around the location where the corresponding coherent strands begin to bend towards the cross-stream direction. Furthermore, the weakly coherent strands appear concentrated around the centerline of the domain, while each coherent strand after separating, red-color circle, from the weakly coherent strand forms a larger-diameter helix. This last observation appeared even in figures 9 to 11 but in a rather different manner. The bending towards the cross-stream of the coherent strand and the disappearance of the weakly coherent strand around its inception could not be clearly presented in figure 8. However, it is made clearly visible in figure 12 by

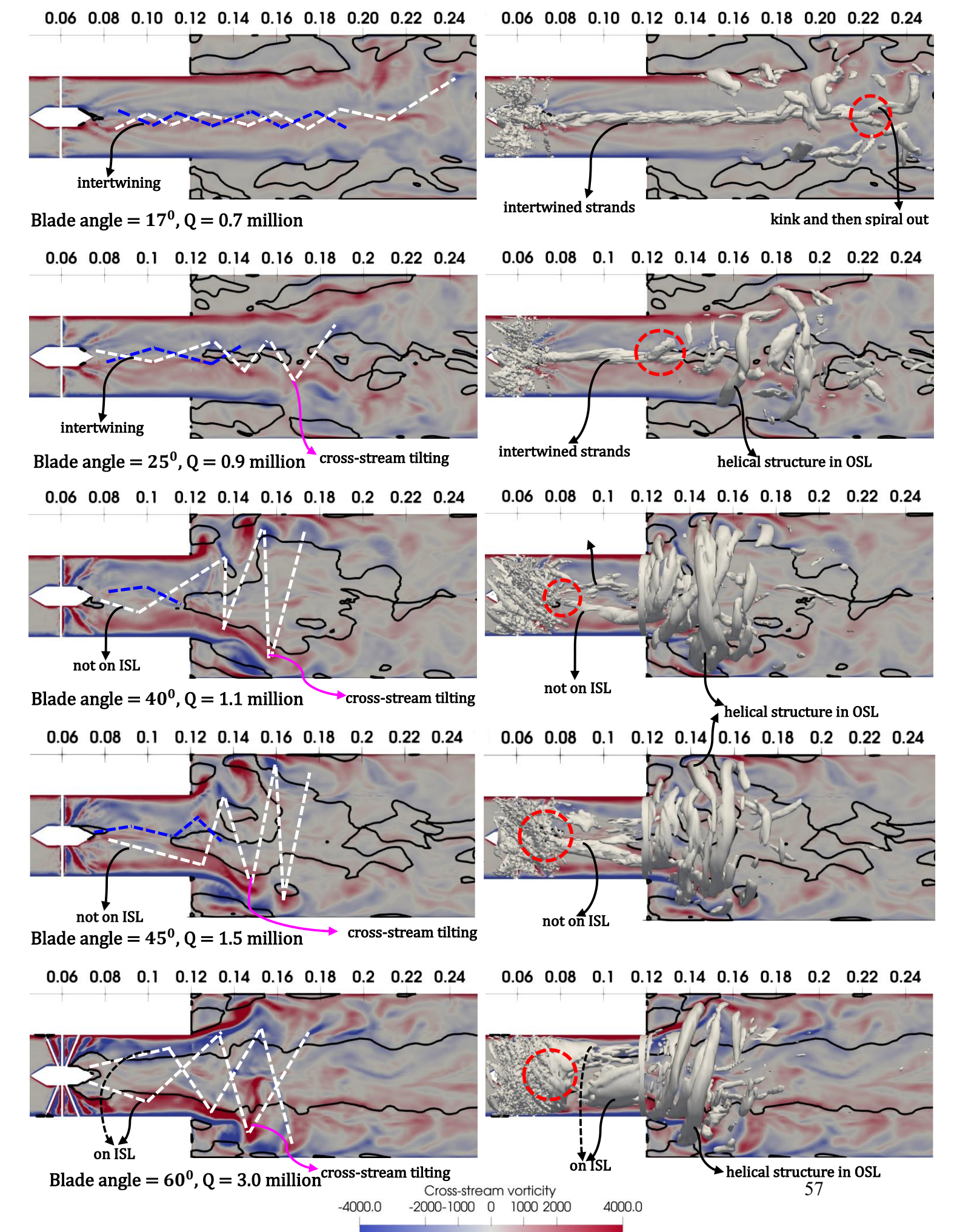


**Figure 12.** Contours of cross-stream vorticity, isolines of zero axial velocity (**black**) and iso-surfaces of Q-criterion (**grey**) for the cases with different swirler angles.

tracking the intersection of the strands with the plane in view. Furthermore, the kink and then the outward spiraling of the coherent strand in the two smallest vane-angle cases appear rather clearly in figure 12 than in figure 8.

We now resolve the origin of each strand of the double helix structure by investigating their relative position to the IRZ and the shear layers. The images in figure 12 corresponding to the  $40^{\circ}$  vane-angle case reveal different regions of high cross-stream vorticity that signify different shear layers. We also recall the velocity fields in figure 7 for better understanding of the following discussion. The boundary-layer in the inlet tube is apparent as the region of high cross-stream vorticity adjacent to the wall. High vorticity fluid from this region interacts with the ORZ downstream of expansion, resulting in a high cross-stream vorticity region on the inner periphery of the ORZ in figure 12. This region around the ORZ is referred to as the outer shear layer, OSL. The coherent structure near the ORZ is a depiction of rollup in the OSL.

Further, the vanes of the swirler in the  $40^{\circ}$  vane-angle case appear to direct higher-momentum fluid close to the wall in figure 7. This creates a region of high cross-stream vorticity adjacent to the boundary layer in the inlet tube in figure 12. High vorticity fluid from this region interacts with the IRZ resulting in a high cross-stream vorticity region on the periphery of the IRZ. This entire inner high-magnitude cross-stream vorticity region after the swirler is referred to in the present work as the inner shear layer, ISL. Here the portion of the coherent strand of the double helix structure upstream of the IRZ does not lie in the ISL or in fact in any shear layer as seen in figure 12, whereas its portion around the IRZ appears as a helical rollup in the ISL.

Based on previous studies [20, 58], helical rollup in the ISL is understood to result from the combined effect of IRZ precession and a convective instability of the ISL. Flows with a stable IRZ typically admit a global helical eigenmode about the time-averaged mean state, with the wavemaker located on or near the centerline close to the upstream end of the IRZ. This helical mode is marginally stable (growth rate  $\approx 0$ ); in flows with swirl strengths near the critical value for the onset of a stable IRZ it can be slightly stable (growth rate  $\lesssim 0$ ) yet persist via stochastic forcing from the flow [58, 65]. This eigenmode thus manifests as a precessing global hydrodynamic mode that is marginally stable (or slightly stable) on the mean-flow state [58, 65]. The overall flow precesses, with oscillation amplitudes usually largest within the IRZ [58]. Thus, precession of the IRZ is coupled with its formation in the mean flow and so is expected to seed the observed rollup in the ISL in the present case, where an IRZ in the mean flow is evident. We will later verify the precession in the present flow field by investigating the dynamics of the coherent strand of the double helix structure. This is because the coherent strand has been widely observed to lock spatially to the IRZ and move along with it [20, 58, 66]. The precession of the IRZ usually also seeds the rollup in the OSL [58], and a similar response of the OSL in the present case is expected. In summary, precession of the IRZ seeds azimuthal disturbances in the shear layers, ISL and OSL, which typically grow by a convective instability of these layers [67] into the corresponding helical rollups, similar to those observed above in the ISL and OSL of the present work. However, tilting away from the centerline of the portion of the coherent strand upstream of the mean IRZ in the present case cannot arise from shear-layer instabilities because it does not lie on any shear layer in figure 12, a point also discussed earlier. Thus, this tilting from the centerline likely arises because the marginally stable global helical eigenmode that causes the large-scale precession of the IRZ also has appreciable oscillation amplitude in this upstream region.

Further, note that the low velocity fluid moving downstream from the boundary layer of the CB of the swirler appears surrounded by only a nominally high-velocity fluid in the  $40^{0}$  vane-angle case in figure 7. This region of velocity gradients appears as a region of high cross-stream vorticity in the wake of the CB of the swirler in figure 12, commonly referred to as the shear layer in the wake of the CB of the swirler. The appearance of this shear layer in figure 12 might not be as clear as the other shear layers owing to its limited radial coverage. Therefore, we present it also using the radial plot of instantaneous axialvelocity at 0.1 m from inlet in figure 13. It shows the presence of a high-velocity-gradient region close to the centerline of the domain in the  $40^{\circ}$  vane-angle case, which corresponds to the shear layer in the wake of the CB of the swirler. The weakly coherent strand appears concentrated along this shear layer in figure 12. Additionally, due to its weak coherency it is expected to arise from a convective instability of the shear layer on which it appears. Perturbations to this CB-shear-layer from the dynamics of the tiltedcoherent-strand might be developing into a helical rollup. This rollup is apparent as the weakly coherent strand of the double helix structure. The perturbation may also arise from the dynamics of the separation bubble that forms behind the CB of swirler. A simple check would be to compare the dynamics of the weakly coherent structure with the dynamics of the source of perturbation. We evaluate the dynamics of the weaklycoherent structure and compare it to the dynamics of the coherent strand of the double

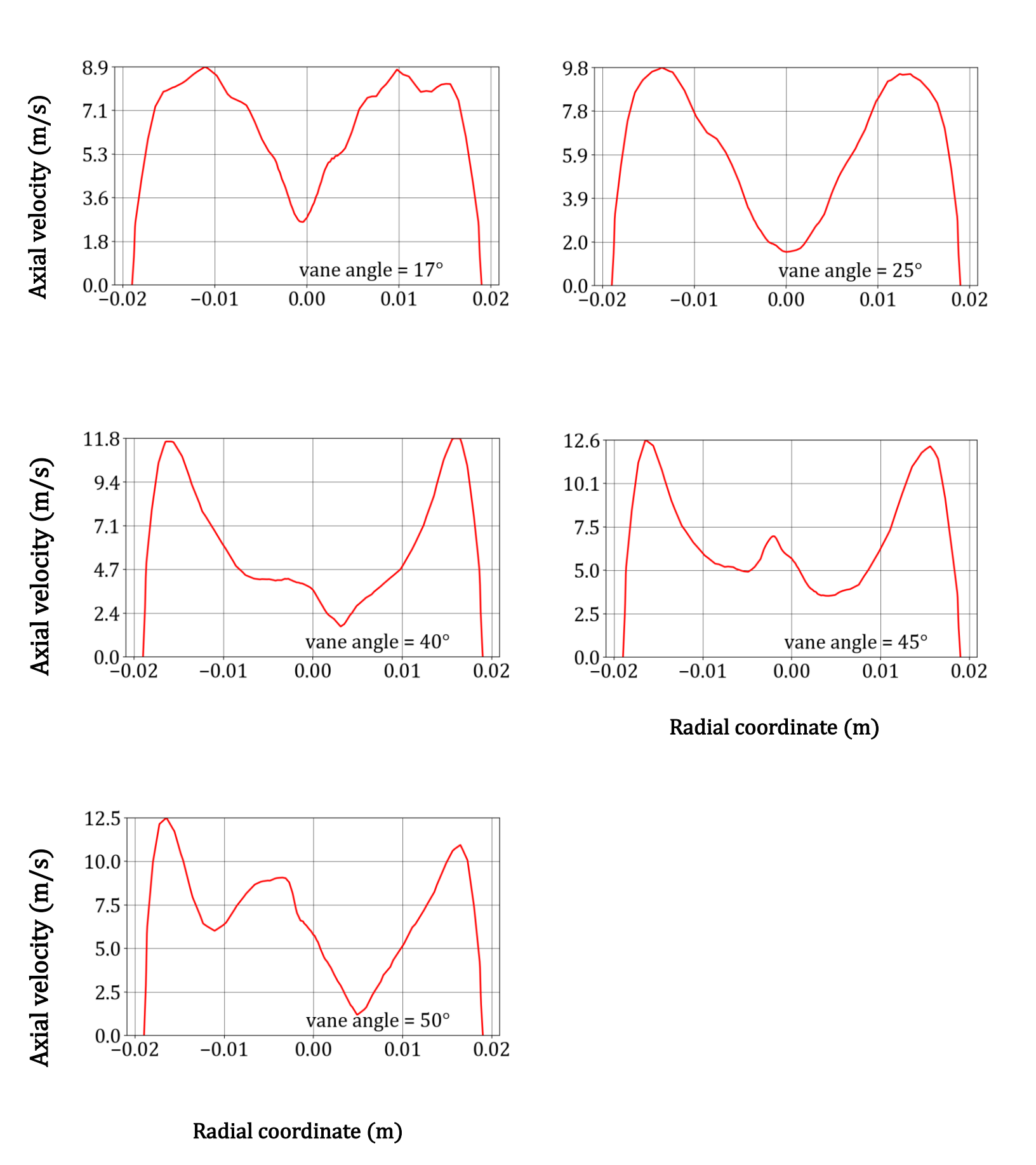


**Figure 13.** Radial variation in axial velocity at the location 0.1 m downstream from the inlet for the cases with different vane angles. An unusual dip in axial velocity appears close to the centreline in the three larger vane angles cases.

helix structure. Hence, in the  $40^{\circ}$  vane-angle case, only the coherent strand is a part of the VC and the weakly coherent strand seems to arise from the instability of the shear layer in the wake of the CB of the swirler.

Figures 8, 12 and 13 reveal similar observations for the case with vane-angle of 45°, which imply similar mechanistic conclusions for the case. The flow features of the  $50^{\circ}$  vane-angle case have not been shown in figures 8 and 12 for brevity of results. However, similar observations were noted for the case and therefore we can expect the reasoning resolved for the  $45^{\circ}$  vane-angle case to apply here as well. Further, the precession of the IRZ in these flows though expected is yet to be verified. We first visually confirm centerline oscillations of the IRZ on a cross-stream plane in each of these three cases, which typically indicates its precession at least over the visualized instances [20]. Accordingly, we revisit figures 10 and 11a, where slices of the IRZ appear asymmetric and perform an eccentric motion on each investigated plane over the shown instances. The slices of the double helix structure located around or outside the periphery of the IRZ move along with it almost locked in space relative to it. The IRZ appears to precess in the direction of rotation of the flow. Further, the instantaneous center of rotation of the bulk flow, marked as IC, in figures 10 and 11a does not coincide with any of the strands, nor is the streamwise vorticity high around this center. Note that the velocity vectors in figures 9 to 11 are not to scale for the convenience of visualization.

The vane-angles in the two smallest vane-angle cases seem ineffective in directing high-momentum fluid close to the wall in figure 7 resulting in the ISL indistinct from the shear layer in the wake of the CB of the swirler in figures 12 and 13. Both strands of the

double helix structure in these two cases appear on the ISL. The rollup appears in the ISL around the IRZ in the 25° vane-angle case induced possibly by the precession of the IRZ. The precession of this IRZ is apparent from figure 9b, although with a small eccentricity. Further, the kink and spiral out of the coherent strand into a larger helix in the smallest vane-angle case occurs well upstream of the IRZ in figure 12. Hence, a reasonable oscillation amplitude of globally unstable helical mode appears to be the cause. The precession of this coherent strand of the double helix after bending is clearly visible in figure 9a. The portion of the strands above the IRZ or the separation region does not appear tilted from the centerline for these two smallest vane-angle cases in figure 8, unlike the other investigated cases. This indicates that the helical twisting of this portion of the strands in the present two cases arises from convective instabilities of the ISL perturbed possibly by separation bubble dynamics.

On the other hand, both strands of the double helix structure in the largest vaneangle case portray similar coherency in figure 8 and their slices in figure 11b are located at similar distances from the center of the domain. Moreover, both these strands appear on the same shear layer, i.e., on the ISL in figure 12. Further, the IRZ extends over the entire length of combustor downstream of the swirler and so there is no portion of the strands lying upstream of the IRZ. The IRZ in the inlet tube appears almost axisymmetric, while its portion just after expansion appears asymmetric in figure 12. The movement of the slices of the IRZ on a plane in the inlet tube is apparent from figure 11b and we plot it in figure 14 for the plane just downstream of expansion. The slice of the IRZ on the cross-stream plane in figure 11b remains almost axisymmetric over time, whereas it displays a

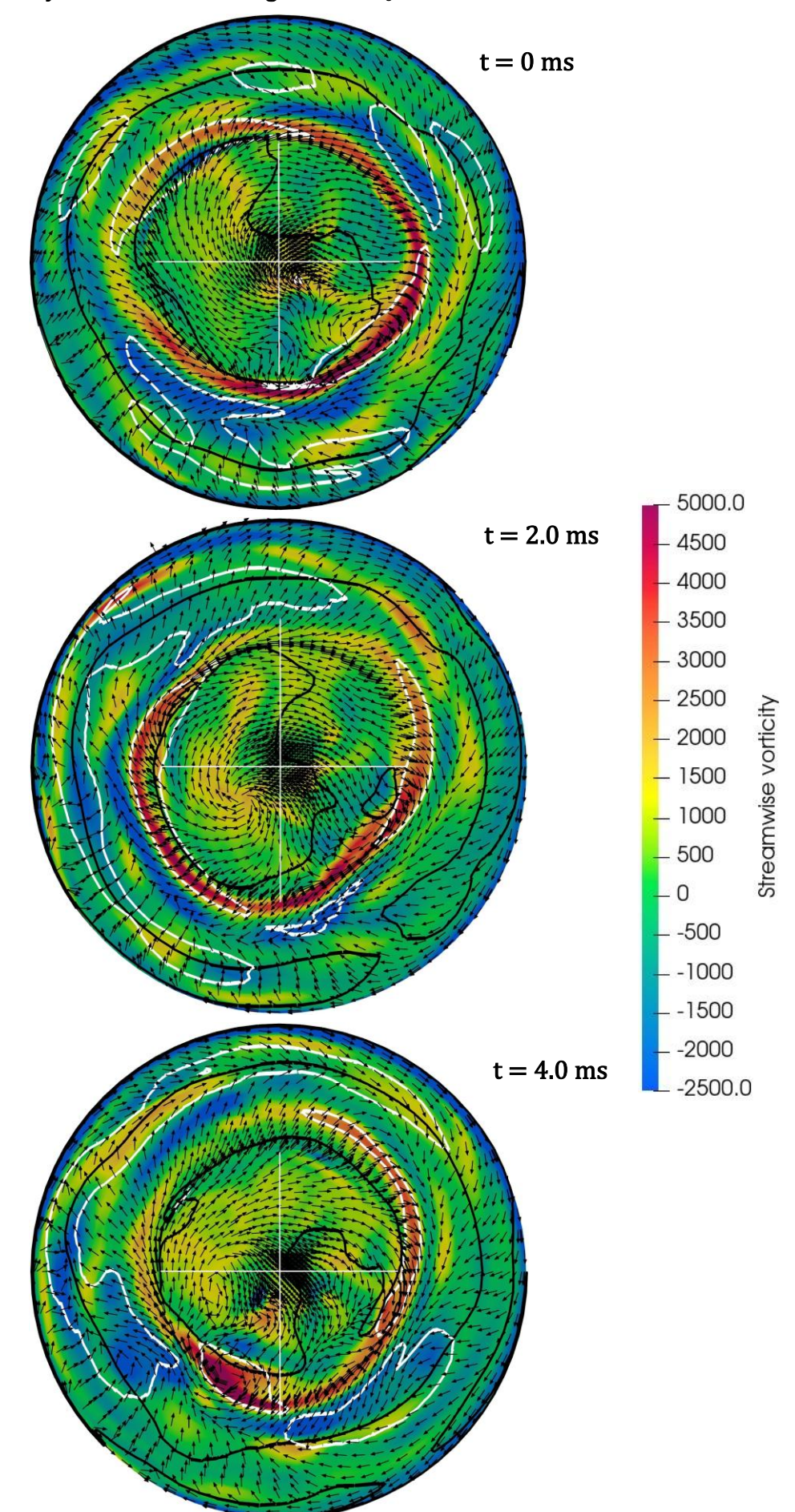


**Figure 14.** Contours of streamwise vorticity, projected velocity vector, zero-axial-velocity isocurves (**black**) &  $^{64}$  isolines (**white**) on a cross-stream plane for the  $60^{\circ}$  vane angle case at three different instances, showing the relative VC, geometric-centre & negative axial-velocity zone. '**y**' is the distance of plane from the inlet.

rotating asymmetry on the cross-stream plane in figure 14. This indicates that the centerline oscillations of the IRZ are not strongest around its uppermost end, a phenomenon rarely encountered [58, 66]. This uncommon behavior likely arises from the merging of the IRZ with the separation bubble of CB. The wavemaker of the global linear helical mode that causes precession of an IRZ sits upstream of the IRZ [58, 65]. The merger of the IRZ with the separation bubble in a similar combustor [68] was reported to disrupt the wavemaker and stabilize the linear helical (IRZ-precession) mode [68]. Precession was still observed in [68], but it was intermittent, driven by stochastic forcing of the stabilized helical mode by flow, more specifically by background turbulence. Moreover, both the strands of the double helix in the present case appear as rollups in the ISL across their entire length beginning from the swirler in figure 12. It is likely that the small amplitude of intermittent precession in the inlet tube and strong amplitude after expansion apparent from figures 11b and 14 are sufficient to excite this rollup.

# C. Dynamics of the flow

The above comprehensive discussion indicates that the VC has a spiral or a single-helix topology when the vane-angle  $\leq 50^{0}$  and a double-helix topology when vane-angle is  $60^{0}$ . Further, a weakly coherent spiral appears in the shear layer behind the swirler's CB when the vane-angle  $\leq 50^{0}$ . These conclusions are based on observations at the instant shown in figures 8, 12 and 13. The weakly coherent structure may persist, either continuously or intermittently, or decay, while the VC, though persistent in swirling flows, may change topology over time. By following the work in [65] and [66] we first verify

whether the VC and the vortical structure in the CB's shear layer predominate in a helical topology over time. Studies in [65] and [66] imply that the coherent precessing motion of a helical flow structure manifests as amplified azimuthal and radial velocity fluctuations along its path, with strong signatures at specific locations. Axial-velocity fluctuations are also amplified but primarily at off-axis locations along the same path, again with strong signatures at specific locations. A helical VC develops into rollups with a significant eccentricity in the ISL. Accordingly, a VC that predominates in a helical topology over time would produce footprints in all the components of mean turbulent kinetic energy (TKE). Further, the second vortical structure of concern in our work appears in the shear layer concentrated about the centerline and so its predominance in a helical topology would produce footprints only in the azimuthal and radial components.

Figures 15 and 16 show contours of the azimuthal component of mean TKE  $(TKE_{m,tang})$  and the axial component of mean TKE  $(TKE_{m,ax})$  for the investigated cases. Here the mean TKE is the result of averaging TKE over ten flow-through times. We first compare the images in figures 12, 15 and 16 for the  $25^{\circ}$  vane-angle case. The upstream maximum in  $TKE_{m,tang}$  arises around an intersection of the field with the double-helix strands, while the downstream maximum arises around an intersection of the field with the weakly coherent strand. The coherent strand or VC intersects the ISL at several locations. The maximum in  $TKE_{m,ax}$  occurs around two of these locations in the plane in figures 16. The value of  $TKE_{m,tang}$  is significant but not maximal at these ISL locations in the present case. Overall similar observations appear in the other cases with vane-angles greater than  $25^{\circ}$  upon comparison of corresponding images of figures 12, 15 and 16.

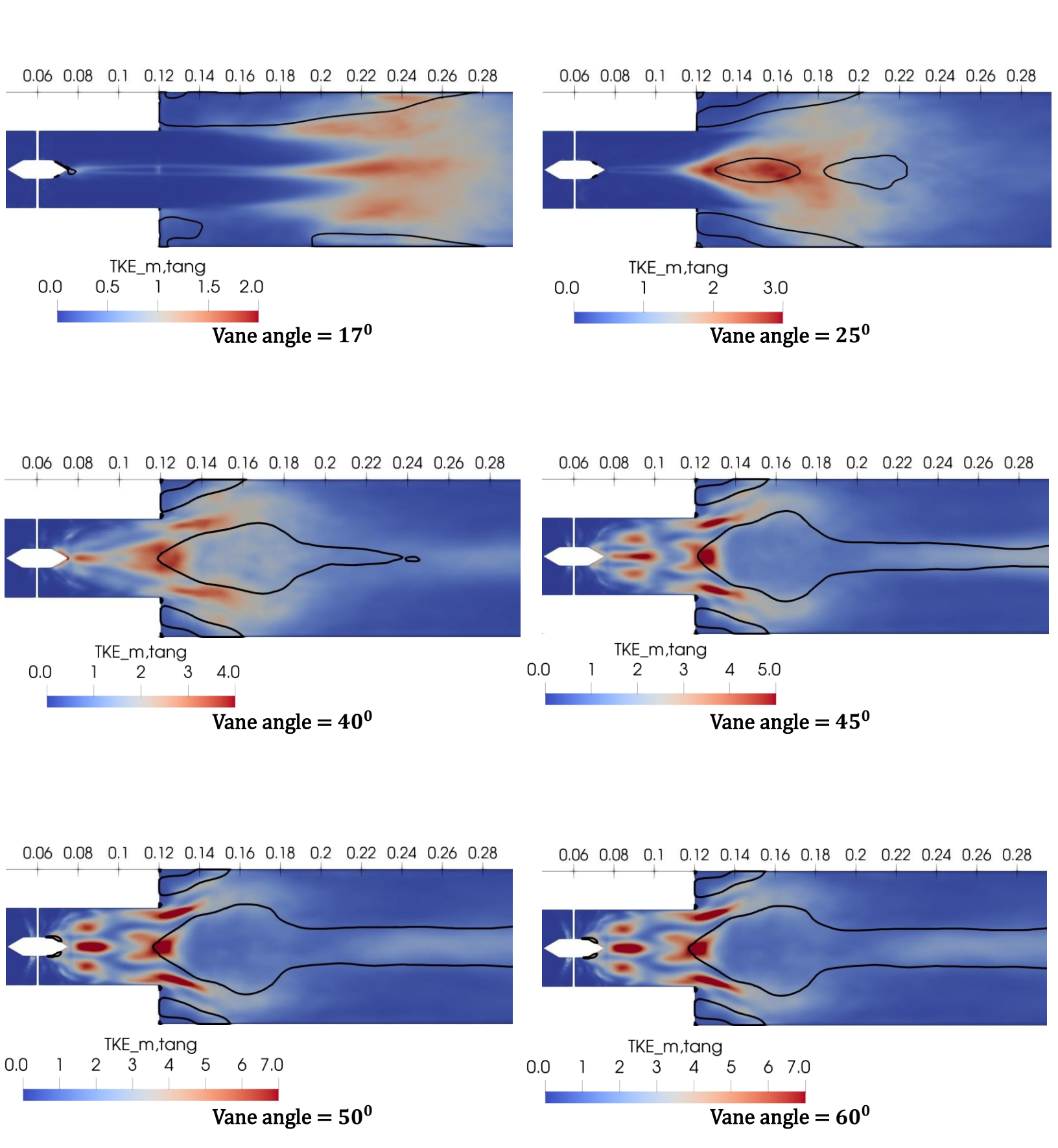


**Figure 15.** Contours of azimuthal component of resolved turbulent kinetic energy  $TKE_{m,tang}$ .

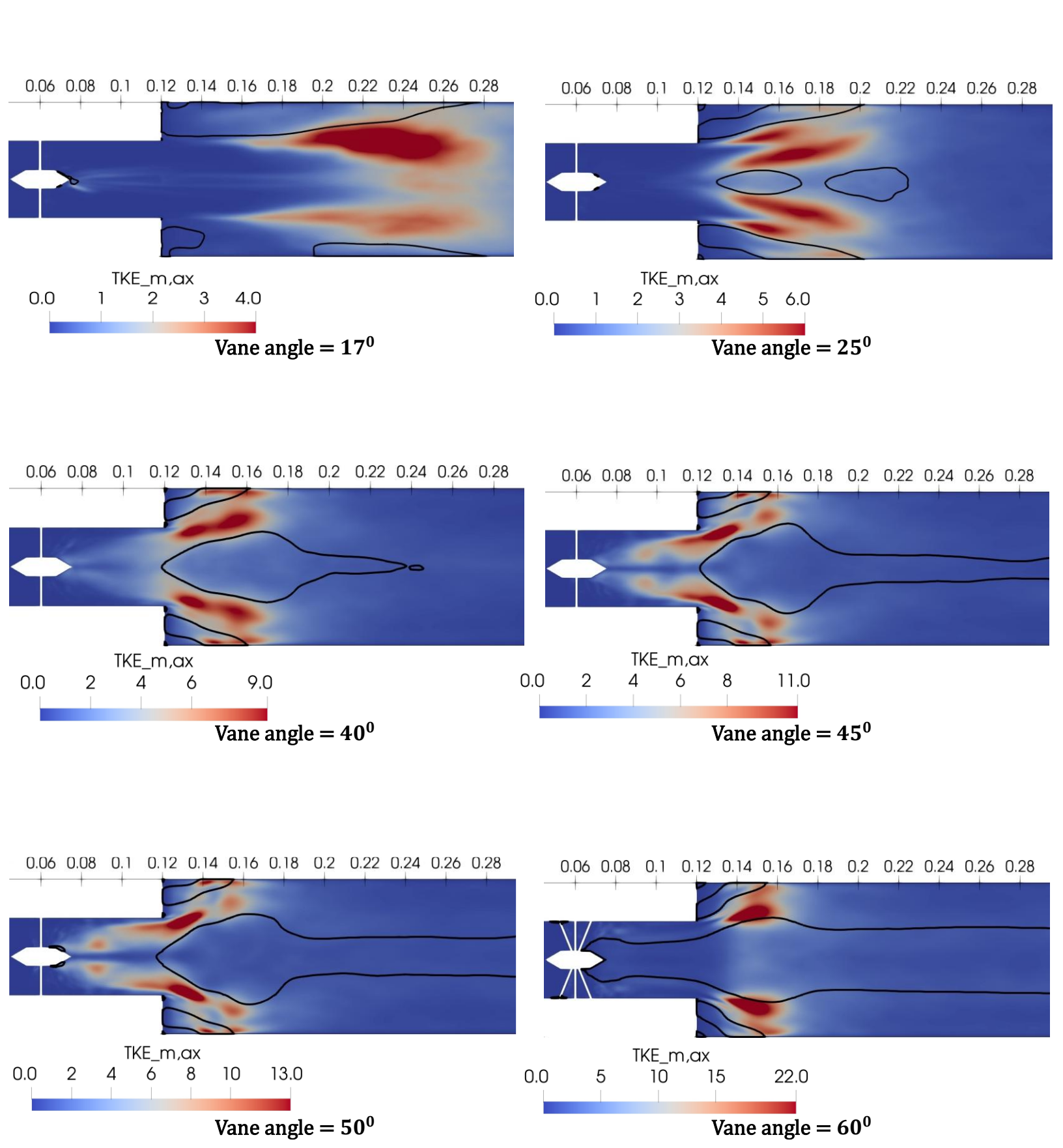


**Figure 16.** Contours of axial component of resolved turbulent kinetic energy  $TKE_{m,ax}$ .

A maximum in  $TKE_{m,tang}$  now starts appearing around the locations in the ISL where  $TKE_{m,ax}$  is maximum. A maximum in  $TKE_{m,tang}$  appears even at off-axis locations in the inlet tube for the cases with vane-angles  $\geq 40^{\circ}$ , because the coherent strand is tilted from the centerline in the inlet tube in these cases. The centerline maxima in  $\mathit{TKE}_{m,tang}$  in figure 15 of these cases appears where the weakly coherent strand intersects. No centerline maxima appear in  $TKE_{m,tang}$  in the largest vane-angle case as both strands lie along the ISL that is close to the wall. In the smallest vane-angle case,  $TKE_{m,tang}$  peaks around the location where the coherent strand kinks, while  $TKE_{m,ax}$ peaks in the vicinity of ORZ are likely caused by the dynamics of rollup in the OSL. The value of  $TKE_{m.ax}$  is significant though not maximal where the coherent strand intersects the plane in view in figure 16 after kinking, indicating to the predominance of a helical VC in time. Note that in figure 16 the contours of  $TKE_{m,qx}$  are asymmetric in the lowest vaneangle case, which will have implications in the following discussion. Further, note that the strength of footprints increases with vane-angle in the investigated cases.

The above discussion indicates that a helical flow structure appears predominantly on the shear layer in the wake of the CB. The footprints of coherent motion also reveal a helical VC prevailing over time. However, these footprints do not uniquely determine the VC topology over time. Similar footprints may result from a single-coherent-strand helix, a double-coherent-strand helix, or from an intermittent presence of both [66]. Moreover, the above analysis does not rule out the co-existence of an axisymmetric topology, since radial and axial oscillations of the IRZ can also produce peaks of  $TKE_{m,tang}$  in the ISL; though not in  $TKE_{m,tang}$ . We now resort to the set of spectral analyses discussed at the beginning

of Section 6 to precisely resolve the prevalent VC topologies and to identify the characteristics of their coherent oscillations that give rise to the above observed footprints.

We perform a cross-spectral analysis over the time-series of axial-velocity fluctuations across two diametrically opposite locations lying on the footprints of VC dynamics, i.e., at the locations where  $TKE_{m,ax}$  peaks in figure 16. The locations of these probe pairs in each investigated case are listed in table 2.

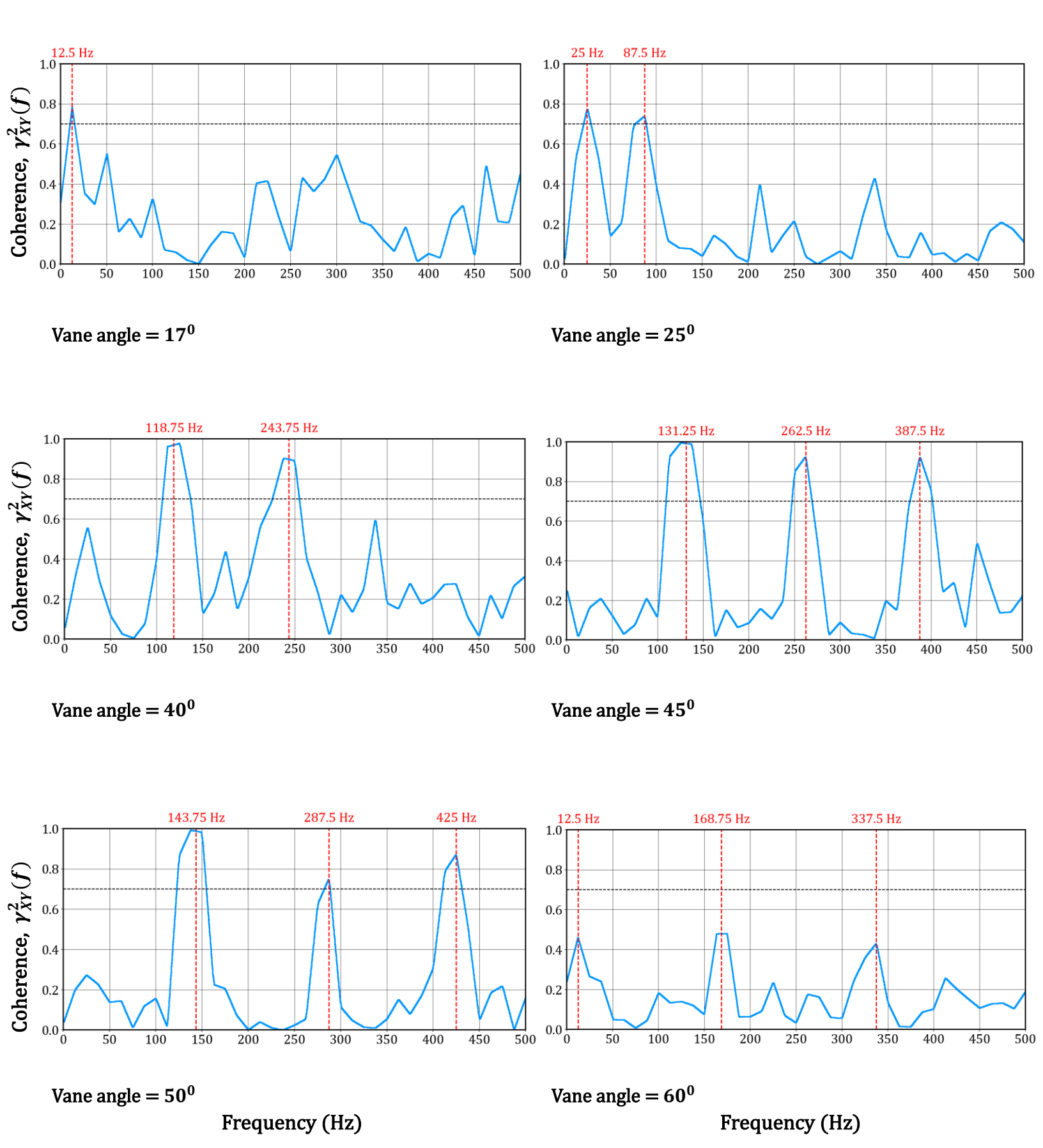
**Table 2.** Coordinates of points for cross-spectral analysis.

Vane-angle for the	Point 1 ( <i>r</i> , <i>z</i> )	Point 2 ( <i>r</i> , <i>z</i> )
investigated cases		
17 <sup>0</sup>	(0.0030 m, 0.2460 m)	(-0.0030 m, 0.2460 m)
25°	(0.0140 m, 0.1680 m)	(-0.0140 m, 0.1680 m)
400	(0.0170 m, 0.1330 m)	(-0.0170 m, 0.1330 m)
45 <sup>0</sup>	(0.0181 m, 0.1330 m)	(-0.0181 m, 0.1330 m)
50°	(0.0186 m, 0.1330 m)	(-0.0186 m, 0.1330 m)
60°	(0.0220 m, 0.1450 m)	(-0.0220 m, 0.1450 m)

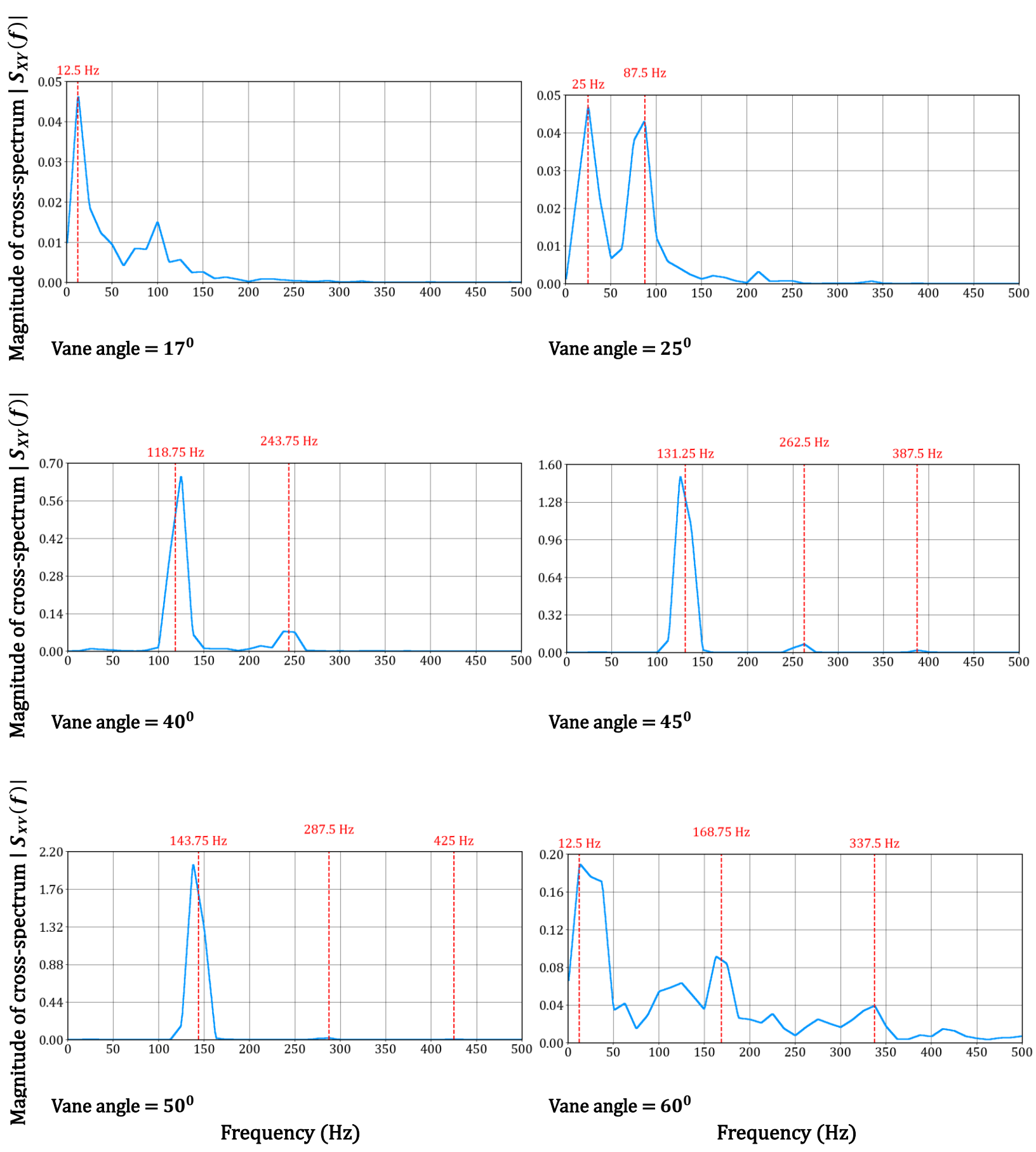
Figure 17 shows the variation of magnitude of the cross-spectrum,  $|S_{XY}(f)|$ , for the investigated cases, where X(t) and Y(t) correspond to the time-series of two diametrically opposite points. Further, Figure 18 shows the variation of the magnitude-squared coherence,  $\gamma_{XY}^2(f)$ . The peaks in  $\gamma_{XY}^2(f)$  in figure 18 and may be in some scenarios in  $|S_{XY}(f)|$  in figure 17 are not razor-sharp since the ensemble length,  $N_{seg}$ , is

modest and the frequency-bin, discrete slot, spacing is 12.5 Hz, as noted in the spectral approach in Section 6. We use a coherence threshold of  $\gamma^2=0.70$  to isolate coherent oscillations, i.e., phase-consistent oscillations, because as evident from figure 18 most of the other peaks lie well below this value and qualify as noise except in the largest vaneangle case. Figure 19 shows the unwrapped cross-phase,  $\Phi_{XY}(f)$ , between the two timeseries, which, using  $m\approx\frac{\Phi_{XY}(f)}{\pi}$  gives a preliminary estimate of the symmetry in coherent oscillations. We reiterate that two-point phase cannot distinguish m=0 from m=2 and since VC structures up to m=2 have been reported in swirling flows [9], we adopt the four-probe azimuthal FFT analysis to identify the correct azimuthal mode [61].

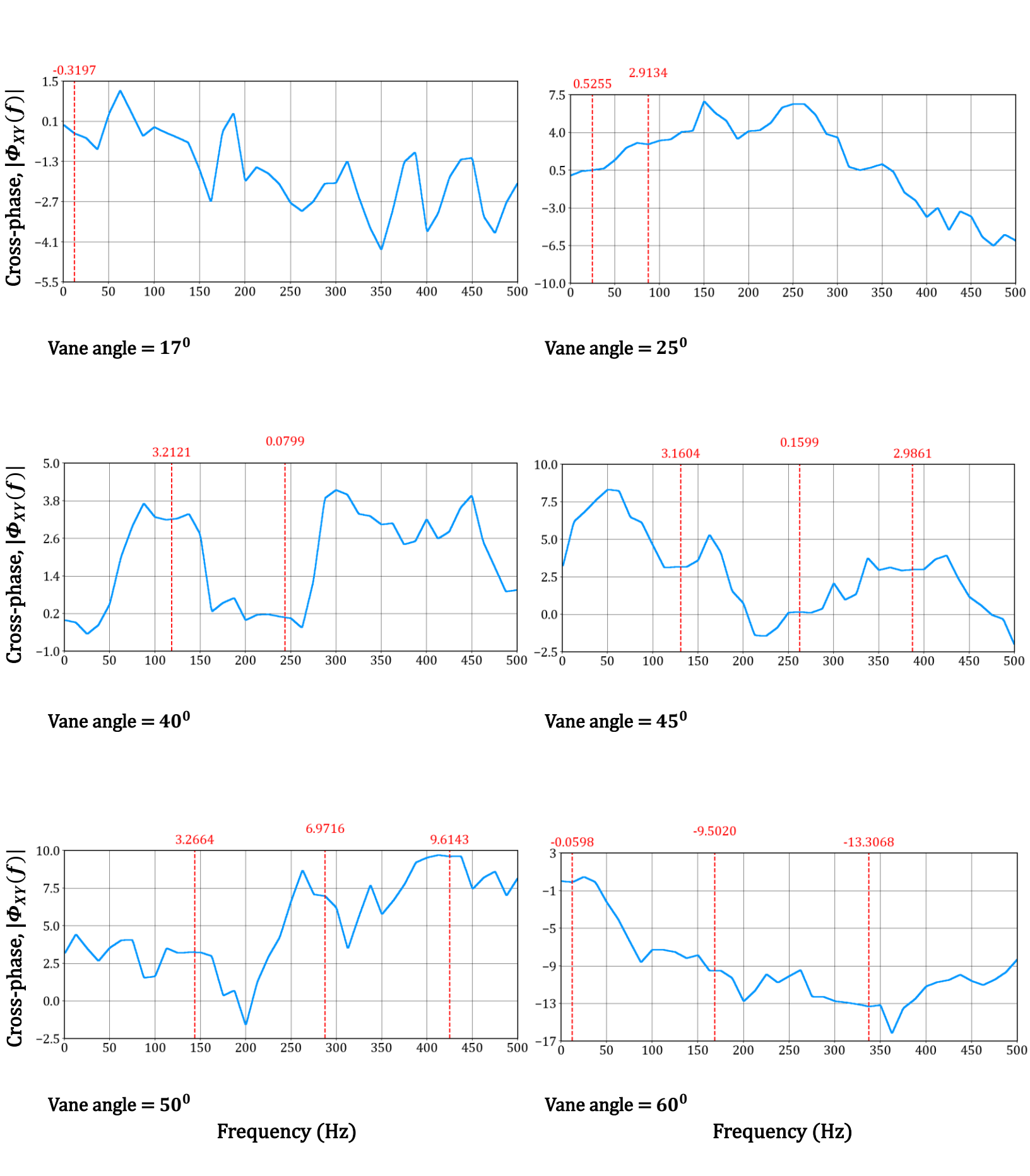
Figures 20 to 25 present the results from azimuthal FFT over the time-series of axial-velocity fluctuations of four probes at the same radius separated by  $\frac{\pi}{2}$  radian. Panels  $\boldsymbol{a}$  in figures 20 to 25 show the modal energy distribution,  $E_m(f)$ . Panels  $\boldsymbol{b}$  show the modal energy fraction, F(m,f) [Eq. (24)]. F(m,f) is distinguishably high at the coherent frequency of a particular mode number, indicating the dominant azimuthal symmetry of the oscillation and thus of the associated flow structure. The threshold value of F(m) for "distinguishably high" is case specific, as is apparent in panels  $\boldsymbol{b}$ , since it is interpreted only at frequencies that first pass the coherence threshold in figure 18. The panels  $\boldsymbol{d}$  in Figures 20 to 25 show the time trace of the band-passed modal signal  $\widetilde{c_m}(t)$  together with its envelope  $\pm |a_m(t)|$  for the selected m and f. Here  $\widetilde{c_m}(t)$  is the oscillatory narrowband signal and  $|a_m(t)|$  is the modal narrow-band amplitude, the slow envelope, for the selected m and f at the native sampling resolution. The native sampling resolution in the present work is the 250th simulation time-step.



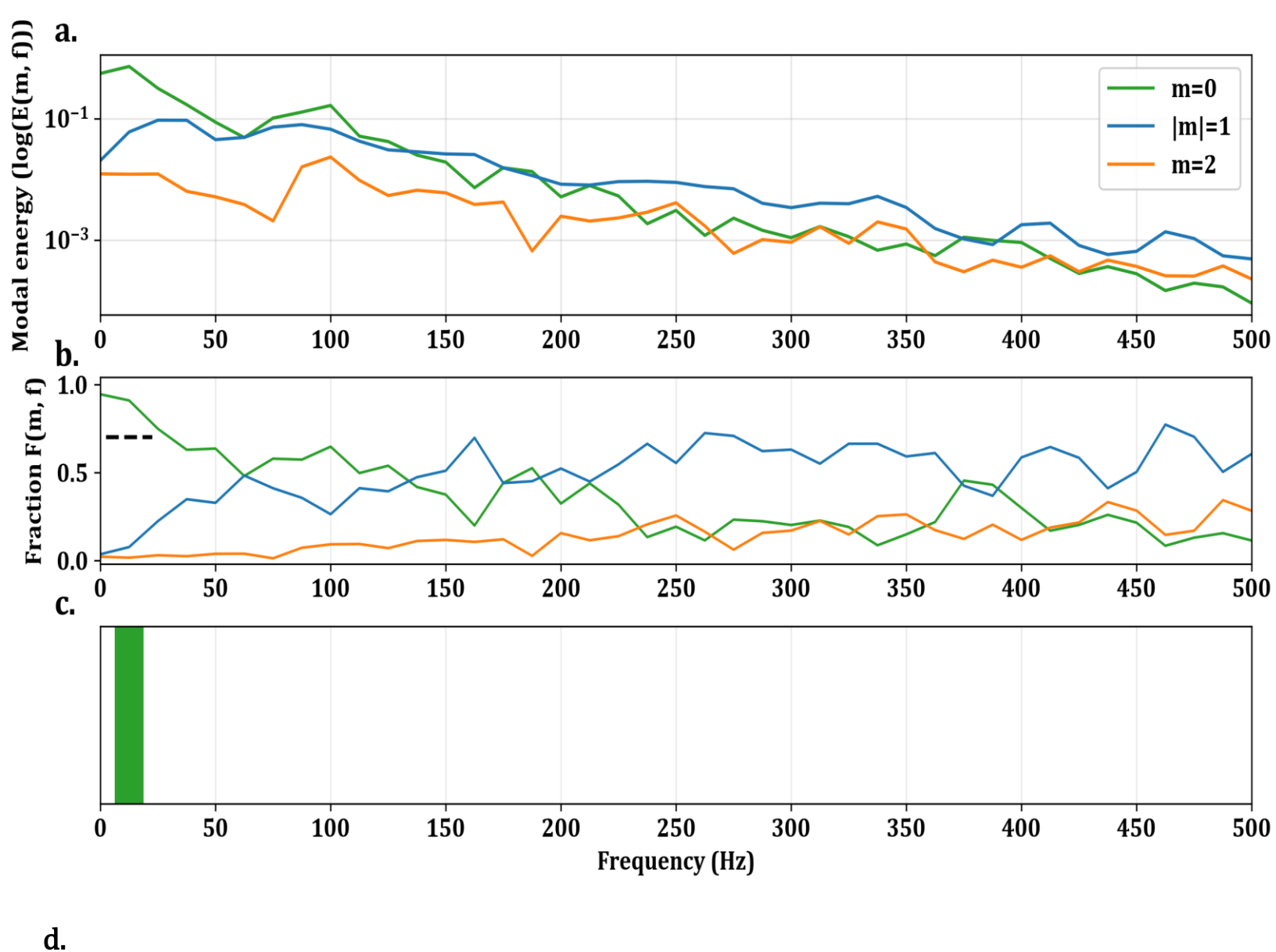
**Figure 17.** Variations of coherence,  $\gamma_{XY}^2(f)$  for the cases with different swirler vane angles. The dotted black line marks the threshold value of coherence, which is 0.7.



**Figure 18.** Variations Magnitude of cross-spectrum,  $|S_{XY}(f)|$  for the cases with different swirler vane angles.



**Figure 19.** Variations cross-phase,  $|\Phi_{XY}(f)|$  for the cases with different swirler vane angles.



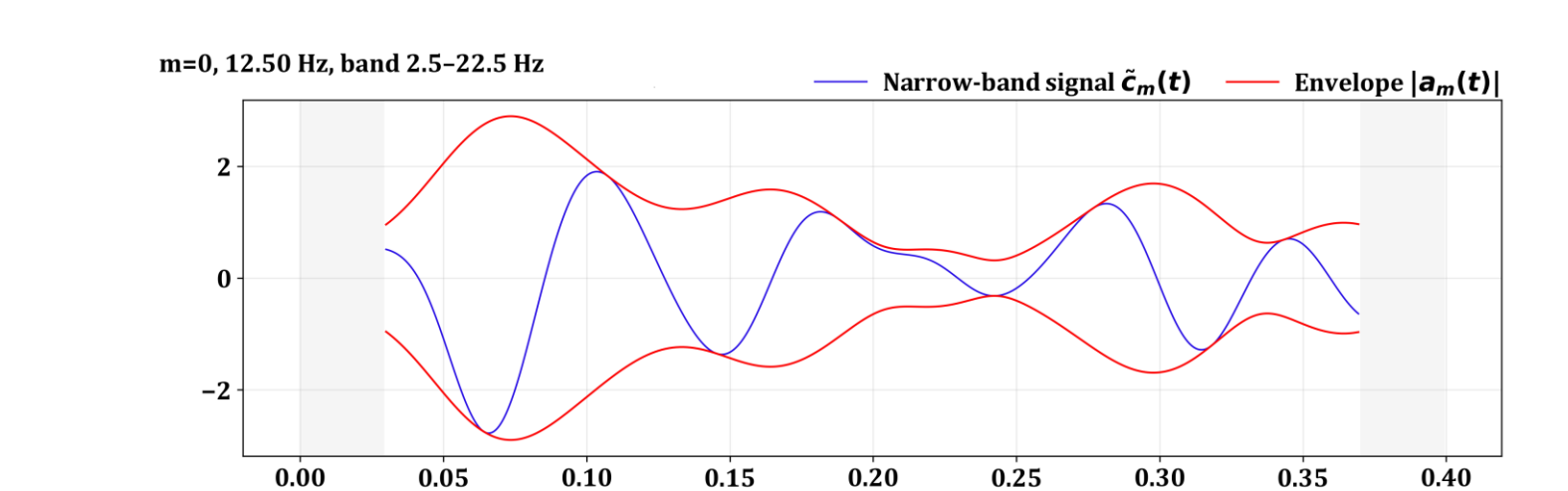


Figure 20 (a) Variation of modal energy, (b) variation of the fraction of modal energy, (c) dominant modes at the coherent oscillations and (d) temporal variation of the signal,  $\widetilde{c_m}(t)$ , and its envelope,  $|a_m(t)|$ , for the coherent oscillations for the case with the vane angle of 17°. Note that the black-color dashed lines in part (b) around the coherent frequencies mark a reference value of 0.7

Time (s)

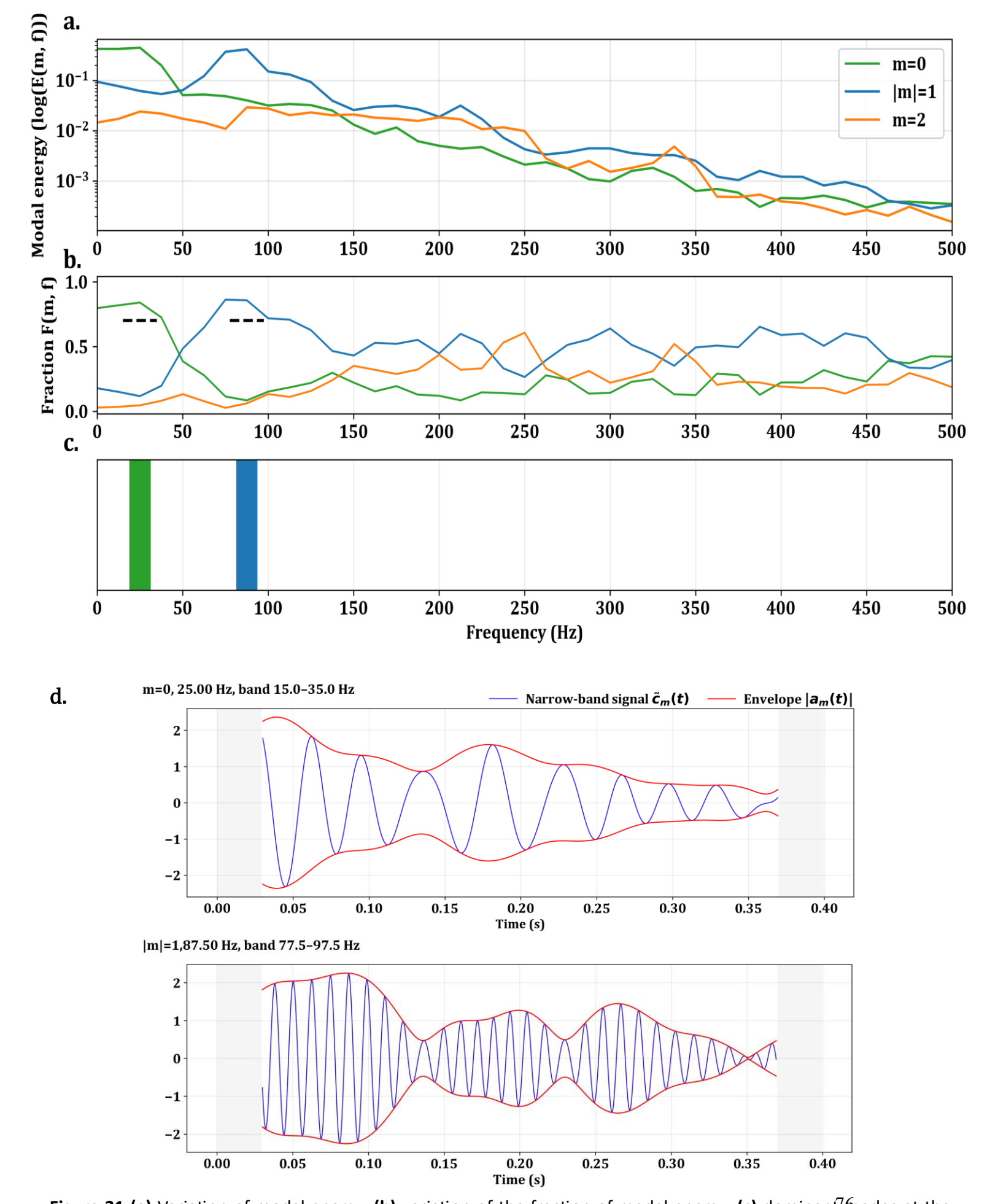


Figure 21 (a) Variation of modal energy, (b) variation of the fraction of modal energy, (c) dominant modes at the coherent oscillations and (d) temporal variation of the signal,  $\widetilde{c_m}(t)$ , and its envelope,  $|a_m(t)|$ , for the coherent oscillations for the case with the vane angle of 25°. Note that the black-color dashed lines in part (b) around the coherent frequencies mark a reference value of 0.7

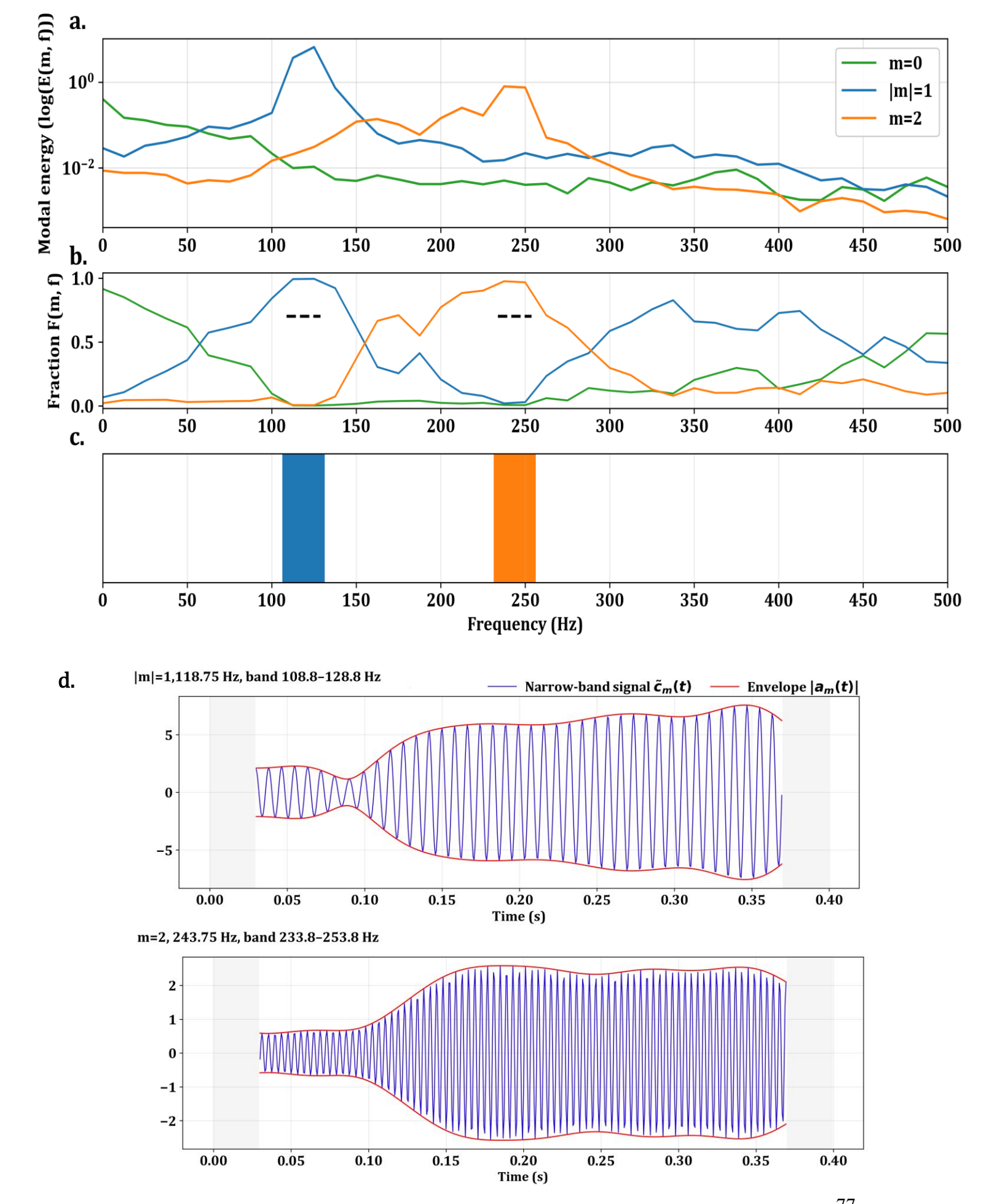
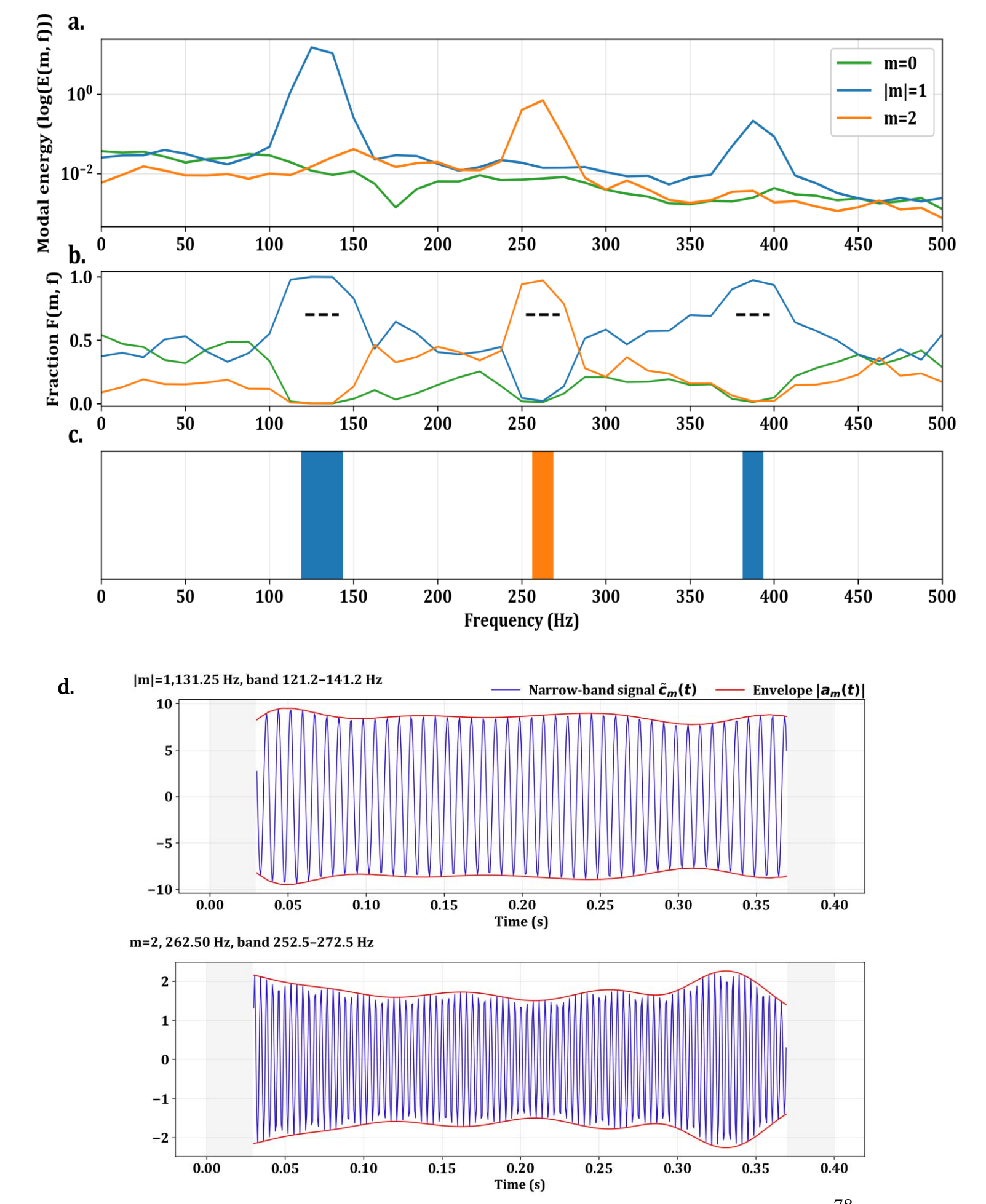
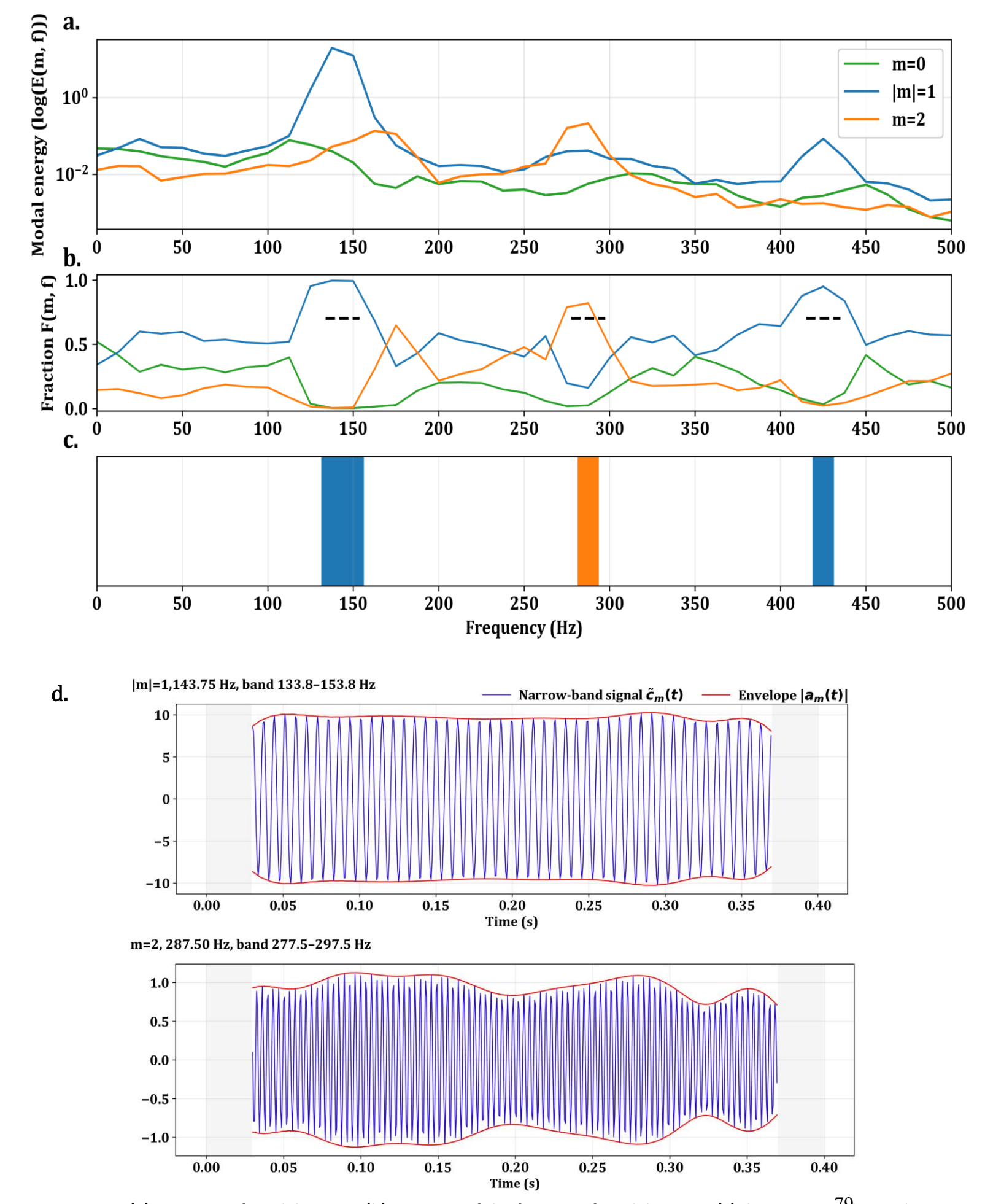


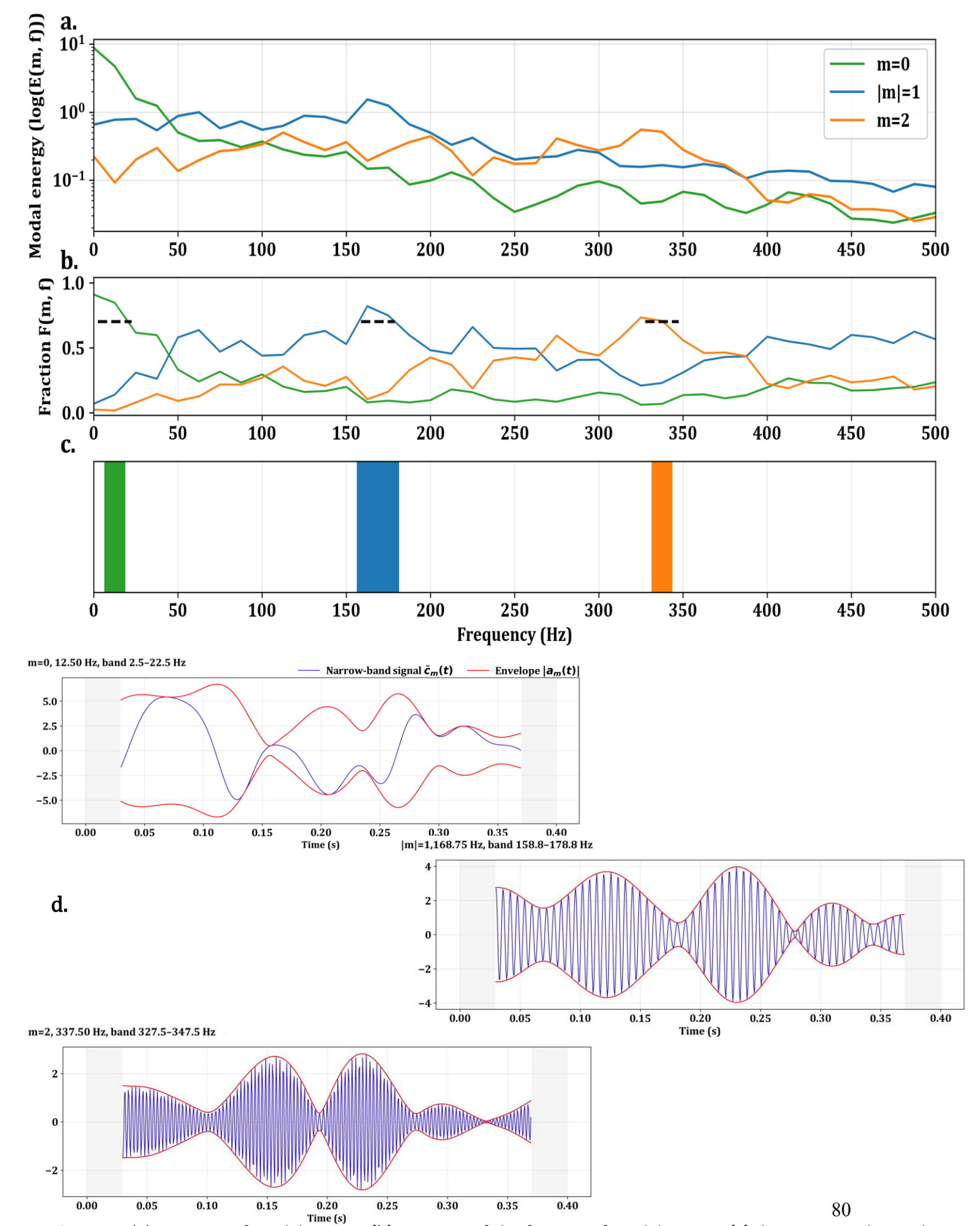
Figure 22 (a) Variation of modal energy, (b) variation of the fraction of modal energy, (c) dominant modes at the coherent oscillations and (d) temporal variation of the signal,  $\widetilde{c_m}(t)$ , and its envelope,  $|a_m(t)|$ , for the coherent oscillations for the case with the vane angle of  $40^{\circ}$ . Note that the black-color dashed lines in part (b) around the coherent frequencies mark a reference value of 0.7



**Figure 23 (a)** Variation of modal energy, **(b)** variation of the fraction of modal energy, **(c)** dominant modes at the coherent oscillations and **(d)** temporal variation of the signal,  $\widetilde{c_m}(t)$ , and its envelope,  $|a_m(t)|$ , for the coherent oscillations for the case with the vane angle of 45°. Note that the black-color dashed lines in part **(b)** around the coherent frequencies mark a reference value of 0.7



**Figure 24 (a)** Variation of modal energy, **(b)** variation of the fraction of modal energy, **(c)** dominant modes at the coherent oscillations and **(d)** temporal variation of the signal,  $\widetilde{c_m}(t)$ , and its envelope,  $|a_m(t)|$ , for the coherent oscillations for the case with the vane angle of 25°. Note that the black-color dashed lines in part **(b)** around the coherent frequencies mark a reference value of 0.7



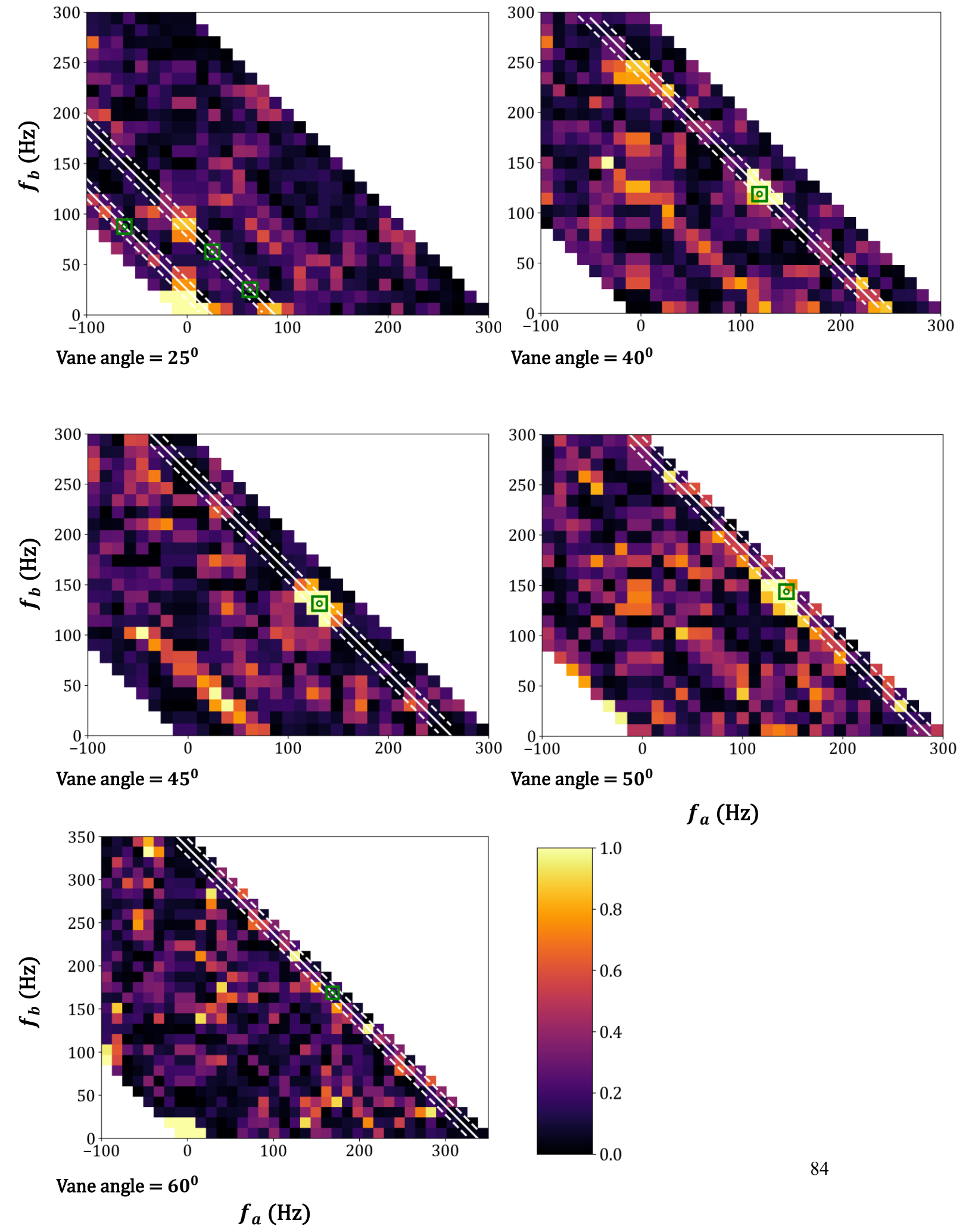
**Figure 25** (a) Variation of modal energy, **(b)** variation of the fraction of modal energy, **(c)** dominant modes at the coherent oscillations and **(d)** temporal variation of the signal,  $\widetilde{c_m}(t)$ , and its envelope,  $|a_m(t)|$ , for the coherent oscillations for the case with the vane angle of  $60^{\circ}$ .

Figure 18 shows red dashed lines that correspond to the frequencies where the magnitude-squared coherence,  $\gamma_{XY}^2(f)$ , peaks and is above the set threshold except in the largest vane-angle case. This first marking appears at  $f_1=118.75,131.25\,\mathrm{and}$ 143.75 Hz for the cases with vane-angle of  $40^{\circ}$ ,  $45^{\circ}$  and  $50^{\circ}$ , respectively. The  $|S_{XY}(f)|$  in figure 17 also peaks around these frequencies, indicating that the dominant correlated energy resides in the associated dynamics. Figures 22a to 24a,  $E_m(f)$ , confirm that among the coherent oscillations, the oscillations at  $f_1$  carry the largest energy in the three cases and they also show that this frequency corresponds to |m| = 1. Figure 19 shows that  $\Phi_{XY}(f) pprox \pi$  radian or m pprox 1 at  $f_1$  in the three cases. The frequencies at the other markings in figure 18, corresponding to coherence beyond threshold, are almost integral multiples of  $f_1$ , i.e.,  $f_2 \approx 2f_1$  and  $f_3 \approx 3f_1$ ; no coherent  $f_3$  in the  $40^0$  vane-angle case. A high value of  $\gamma_{XY}^2(f)$  shows that the two time-series remain consistently phasecorrelated at these frequencies. However,  $|S_{XY}|$  is relatively small at  $f_2$  and  $f_3$  in the three cases, implying small correlated energy in the corresponding oscillations, as also reflected in figures 22a to 24a.  $|S_{XY}|$  is specifically quite small at  $f_3$  and is therefore not discussed further. Figure 19 shows that  $\Phi_{XY}(f) pprox 2\pi$  radian or m pprox 2 at  $f_2$  in the  $50^0$  vane-angle case. It shows that  $\Phi_{XY}(f) \approx 0$  radian or  $m \approx 0$  at  $f_2$  in the cases with vane-angle of  $40^0$ and  $45^{\circ}$ . However, recall that the two-point phase cannot distinguish between 0 and  $2\pi$ radians and so between m=0 and m=2 [58]. This is also evident upon comparing figure 19 with figures 22b to 24b. Figures 22b to 24b, arising from the four probes azimuthal FFT, show that m=2 at  $f_2$  in each of the three cases of interest. Hence, a VC exhibiting strong single helix signatures, |m|=1, and weaker double helix signatures, m=2, is expected to form in the cases with vane-angles of the  $40^{\circ}$ ,  $45^{\circ}$  and  $50^{\circ}$ .

The band-passed modal signal  $\widetilde{c_m}(t)$  and its envelope  $|a_m(t)|$  for |m|=1 and m=2 at their characteristic frequencies  $f_1$  and  $f_2$ , respectively, in figures 22d to 24d show that the oscillation amplitudes are higher for the  $(|m|=1,f_1)$  pair or tone. Further, it is apparent that the amplitudes for  $(|m|=1,f_1)$  and  $(m=2,f_2)$  in the  $45^0$  and  $50^0$  vane-angle cases are nearly constant over time, indicating stable limit-cycle oscillations for these tones. This behavior is consistent with precession in the  $45^0$  and  $50^0$  vane-angle driven by a marginally stable hydrodynamic mode on the mean state. The oscillation amplitude for  $(|m|=1,f_1)$  and  $(m=2,f_2)$  in the  $40^0$  vane-angle case remains nearly constant for a while and then grows to a higher, nearly constant level. This behavior is consistent with slow drift of the mean flow (stochastic variations) that alters the characteristics of the marginally stable helical mode driving the precession.

We now test whether  $(m=2,\,f_2\approx 2f_1)$  arises from quadratic self-coupling of  $(|m|=1\,,f_1)$  or is an azimuthal coherent oscillation independent from it, by investigating the corresponding squared cross-bicoherence,  $b^2(X_{f_1},X_{f_1}\to Y_{2f_1})$ . A high  $b^2$  for a triad  $(f_a,f_b,f_c)$  indicates reproducible second-order phase-locking, a phase-sum/-difference relation, i.e.,  $\Phi_{XY}(f_c)\approx \Phi_{XY}(f_a)\pm \Phi_{XY}(f_b)$ , across ensembles, while a low  $b^2$  indicates no such stable phase-locking despite any spectral energy. The  $b^2(X,X\to Y)$  maps for the investigated cases are plotted in figure 26. To account for finite bin spacing,  $\Delta f=12.5$ , and window broadening, we draw guide bands so that bin mismatch is not misread as a weak coupling. We place constant-sum anti-diagonals at the measured second peak with

its own uncertainty,  $f_a+f_b=f_2\pm\sigma_{f_2}$  and we set  $\sigma_{f_2}=10$  Hz. The white-color solid anti-diagonal marks  $f_a+f_b=f_2$  and the white-color dashed anti-diagonals mark the tolerance band  $f_a+f_b=f_2\pm10$  Hz. We also mark the self-pair  $(f_1,f_1)$  with a green-color circle and draw an axis-aligned green-color square  $|f_a-f_1|\leq \frac{10}{\sqrt{2}}$  Hz,  $|f_b-f_1|\leq \frac{10}{\sqrt{2}}$  Hz around it, which is RMS uncertainty. Within the overlap of this square and the constant-sum band, the observed  $b^2(X_{f_a},X_{f_b}\to Y_{f_a+f_b})$  is very high in all three cases in figure 26, although  $\gamma_{XY}^2(f_2\approx 2f_1)$  is high. Therefore, m=2 oscillation at  $f_2\approx 2f_1$  is predominantly the first harmonic of |m|=1 oscillation at  $f_1$  in the investigated swirl combustor cases with vane-angles of  $40^0$ ,  $45^0$  and  $50^0$ . In other words, m=2 oscillation at  $f_1$  in these cases. Its implication on VC is that the double helix signatures apparent on it from  $(m=2,f_2\approx 2f_1)$  arise from self-coupling of single helix signatures from  $(|m|=1,f_1)$  and therefore the two signatures oscillate in a phase-locked manner.



**Figure 26.** Squared cross-bicoherence,  $b^2$ , map for the cases with different vane angles.

Figure 18 shows two frequencies, 25.0 and 87.5 Hz, where the magnitudesquared coherence,  $\gamma_{XY}^2(f)$ , peaks and is above the set threshold of 0.7 in the case with  $25^{\circ}$  vane-angle. Note that the  $\gamma_{XY}^2(f)$  value at each peak in the present case is just above the threshold value of 0.7, whereas it is very close to 1.0 at corresponding peaks in the  $40^{\circ}$ ,  $45^{\circ}$  and  $50^{\circ}$  vane-angle cases.  $|S_{XY}(f)|$  and  $E_m(f)$  in figures 17 and 21a are relatively high and comparable at these frequencies, indicating two dominant coherent oscillations in the flow. F(m, f) in figure 21b shows the dominance of m = 0 around 25.0 Hz and |m| = 1 around 87.5 Hz. Further, figure 17 shows that the magnitude-squared coherence,  $\gamma_{XY}^2(f)$ , around 62.5 Hz is well below the threshold value for a coherent motion. However, figure 18 shows a corresponding reasonable  $|S_{XY}(f)|$  relative to its value at 31.5 and 87.5 Hz.  $E_m(f)$  and F(m, f) in figure 21 are spread across different azimuthal modes at 62.5 Hz but are reasonably high in |m| = 1. The triad 25.0, 62.5  $\rightarrow$ 87.5 Hz and its permutations are frequency-consistent and  $b^2$  is low for 25.0, 62.5  $\rightarrow$ 87.5 Hz, for  $62.5, 25.0 \rightarrow 87.5 \text{ Hz}$  and for  $87.5, 62.5 \rightarrow 25.0 \text{ Hz}$  in figure 26. Accordingly, the axisymmetric oscillations (m=0, 25.0 Hz) and the helical oscillations (|m|=1, 87.5Hz) are quadratically independent. The band-passed modal signal  $\widetilde{c_m}(t)$  and the envelope  $|a_m(t)|$  for m=0 and |m|=1 at their characteristic frequencies, 25.0 Hz and 87.5 Hz, respectively, are shown in figure 21d. These signals have comparable amplitudes, with dips to small values and subsequent recovery. The |m|=1 signal appears more dynamic. The amplitudes for (|m| = 1, 87.5 Hz) wax and wane with large variations, approach near zero at times and then re-grow toward a limit-cycle-like oscillation. This evolution suggests that precession in the 25° vane-angle case is driven by stochastic forcing from

background turbulence acting on a slightly stable helical hydrodynamic mode. Taken together, a single helix VC coexists with an axisymmetric oscillation, likely associated with IRZ motion, in the  $25^{\circ}$  vane-angle case, with the two tones quadratically independent and sustained by stochastic forcing on slightly stable axisymmetric and helical modes.

Figure 18 shows a single above-threshold coherence peak at 12.5 Hz in the lowest vane-angle case,  $17^0$ .  $|S_{XY}(f)|$  and  $E_m(f)$  are also the highest near the same frequency in figures 17 and 20a. F(m, f) for m = 0 dominates around 12.5 Hz in figure 20b. The corresponding band-passed modal signal  $\widetilde{c_m}(t)$  and the envelope  $|a_m(t)|$  in figure 20d exhibit pronounced waxing and waning of the signal's amplitude. Accordingly, we attribute this coherent motion to the axial, axisymmetric, oscillation arising from the spatio-temporal intermittency of the IRZ in the present case, this intermittency has already been discussed in Sections 6.1 and 6.2. No sustained helical coherence is detected in the present case. It could result from the helical oscillations being either largely absent or incoherent, or from the asymmetry of the flow evident in figure 16. The asymmetry biases the VC toward one side of the domain so that the four probes do not receive a balanced helical signature. Spectral arrays respond best when the coherent structure affects all sensors similarly. Further, visual checks using the Q-criterion over about 640 instances show sporadic helical structure, supporting the interpretation that the absence of helical coherence is either a numerical artifact due to flow asymmetry or from genuinely incoherent helical motion of the VC.

Finally, we investigate the largest vane-angle case,  $60^{0}$ , where the magnitude-squared coherence,  $\gamma_{XY}^{2}(f)$ , does not exceed the set threshold of 0.7 at any investigated

frequency. However,  $\gamma_{XY}^2(f)$  shows distinguishable peaks, above the value 0.4, at 12.5, 168.75, and 337.5 Hz relative to other frequencies in figure 18. Thus, the precession flow dynamics in the largest vane-angle case would appear weakly coherent. The values of  $|S_{XY}(f)|$  and  $E_m(f)$  in figures 17 and 25a are highest around 12.5 Hz and reasonable at the other two characteristic frequencies. F(m, f), from azimuthal decomposition, in figure 25b shows that m=0 dominates around 12.5 Hz, |m|=1 dominates around 168.75 Hz and m=2 dominates around 337.5 Hz. Thus, this dynamic system exhibits all key aspects of helical oscillations prevalent in swirling flows [9]. Interestingly,  $b^2$  is low for the 168.75,  $168.75 \rightarrow 337.5$  Hz triad in figure 26, indicating that the m=2 oscillation at 337.5 Hz is not the first harmonic of the |m| = 1 oscillation at 168.75 Hz in the largest vane-angle case. This contrasts with the behavior in cases with vane-angles up to and including  $50^{\circ}$ . The temporal signal and its envelope for m=0, |m|=1 and m=2 at their characteristic frequencies, 12.5 Hz, 168.75 Hz and 337.5 Hz, respectively, in figure 25d show largest oscillation amplitudes for m=0, smaller for |m|=1 and smallest for m=2. None of these signals persist at a constant amplitude; their envelopes wax and wane strongly and approach near-zero at times. This behavior is consistent with the characteristic oscillations being sustained by stochastic forcing from background turbulence on slightly stable hydrodynamic modes. The IRZ extends across the combustor downstream of the swirler in the largest vane-angle case and thereby merges with the separation bubble of CB. This merger is known to disrupt the wavemaker of the precessing hydrodynamic mode and stabilize it [68]. Any residual precession then arises from stochastic forcing of this stabilized mode, leading to large amplitude modulations as observed. Conclusively, a VC forms in the largest vane-angle case with strong single helix characteristics and weaker double helix characteristics interacting with a stronger axisymmetric oscillation likely induced by IRZ motion; these helical and axisymmetric tones are sustained by stochastic excitation of stable hydrodynamic modes. Notably, the double-helix tone does not arise from quadratic self-interaction of the single-helix tone (low  $b^2$ ), i.e., they are quadratically independent and are distinct helical hydrodynamic modes.

Finally, the lowest coherent precession frequencies for the case with vane-angles of  $25^{\circ}$ ,  $40^{\circ}$ ,  $45^{\circ}$ ,  $50^{\circ}$  and  $60^{\circ}$  are 87.5, 118.75, 131.25, 143.75 and 168.75 Hz, respectively. The precession frequency for the smallest vane-angle if exist could not be resolved using the above spectral methods.

To probe the origin of the weakly coherent strand discussed earlier and seen for cases with vane-angles of  $17^{\circ}$ ,  $25^{\circ}$ ,  $40^{\circ}$ ,  $45^{\circ}$  and  $50^{\circ}$  we compute an FFT (fast DFT) on the time-series of x-velocity fluctuations at the footprint of the weakly coherent strand in the  $TKE_{m,tang}$  in figure 15. Figure 27 shows that strongest FFT amplitudes occur at 52.00, 94.12, 120.00, 128.00 and 140.00 Hz for the cases with vane-angles of  $17^{\circ}$ ,  $25^{\circ}$ ,  $40^{\circ}$ ,  $45^{\circ}$  and  $50^{\circ}$ , respectively. These frequencies are nearly the same as the lowest precession frequencies mentioned above, supporting the interpretation that the strand originates from VC precession dynamics. Note that the spectrums for the two lowest vane-angle cases are very noisy around their global peak in amplitude.

Conclusively, a VC with strong single-helix characteristics appears to prevail in the swirl combustor with ER=2.0 operating at  $Re_{inlet}=2\times10^4$  for all the investigated

vane-angles; up to  $60^0$ , i.e.,  $SN_g \leq 1.15$ . Manoharan et~al. [58] likewise observed a single-helix VC to prevail in a swirling jet with  $Re_{inlet} \approx 6 \times 10^4$  over a wide range of swirl numbers. Drawing on this background and studies [11-13], recall literature review, VB in any isothermal swirl-combustor flow with  $Re_{inlet} \geq 10^4$  and  $ER \geq 2.0$  is expected to produce a VC with strong single helix characteristics. Notably, weak but observable double-helix characteristic appear for vane angles above  $25^0$  in the present work. The double-helix tone is found to result from quadratic self-interaction of the single helix tone for vane angles below  $60^0$ . These two tones are quadratically independent in the  $60^0$  vane-angle case, i.e., they are distinct helical hydrodynamic modes. We believe the foregoing discussions address most of the open issues identified in the literature review and therefore we proceed to the conclusion of the present work.

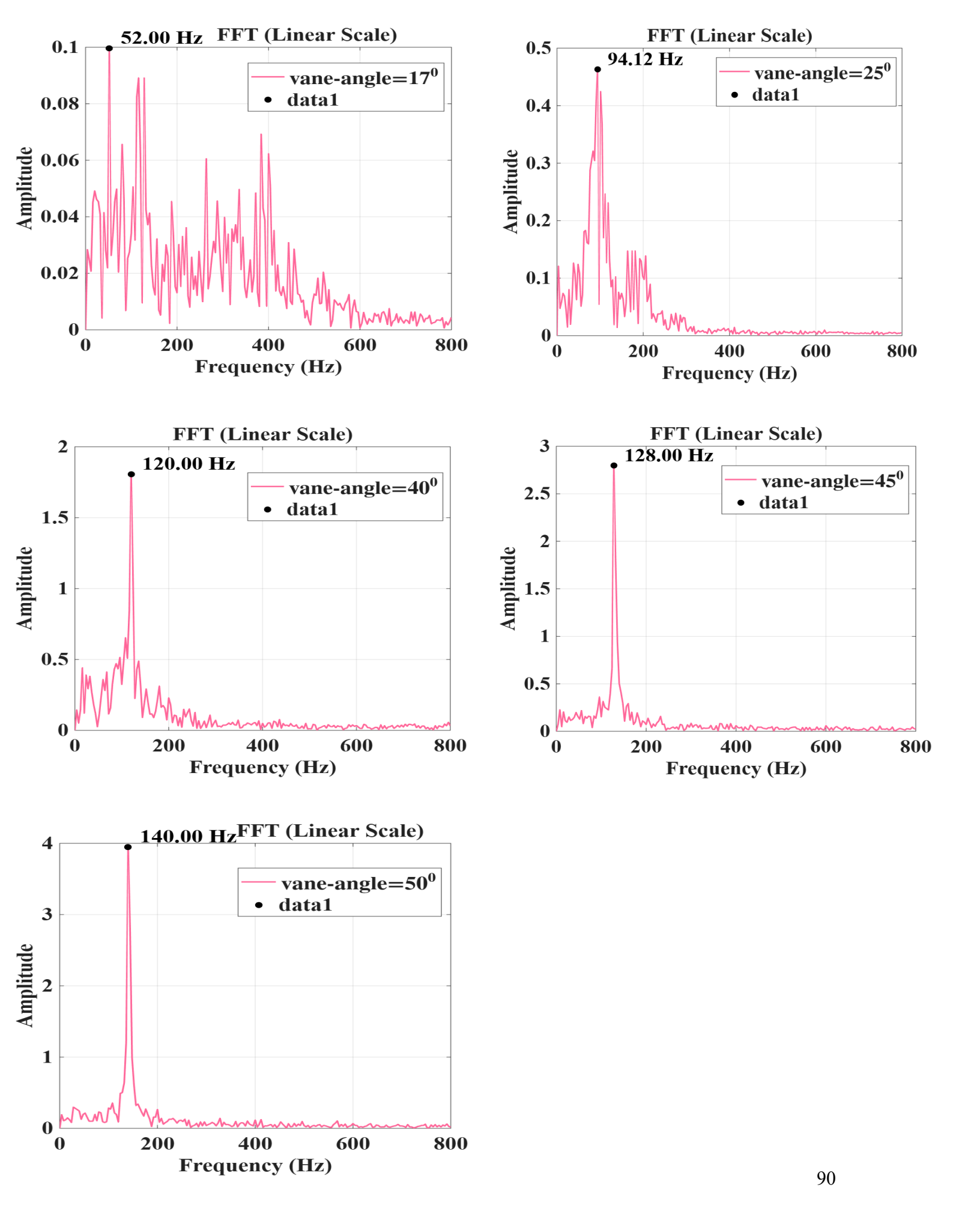


**Figure 27.** Fast Fourier Transform of the fluctuation of x-velocity component at the geometric centre of the cross-stream plane located 0.115 m downstream from the inlet.

#### **Conclusions**

This study maps the onset and topology of vortex breakdown in isothermal swirling flows with inlet Reynolds number,  $Re_{inlet} \ge 10^4$  within a canonical swirl combustor geometry with expansion ratio,  $ER_1 \ge 2.0$  by systematically varying the swirler vane-angles. The study uses a Large-eddy-simulation based solver validated against an experimentally obtained velocity field in a well-documented lab-scale swirl combustor facility. The onset of VB is quantified using the generic swirl strength formulation,  $\mathit{SN}_g$ , where the onset is identified by the appearance of IRZ in the mean flow since highly intermittent IRZs may appear at lower swirl strengths in instantaneous flows but could not support flame stabilization. A stable VB first appears in the selected swirl combustor flow at the vaneangle of  $25^{\circ}$ . Further,  $SN_q$  provides the most appropriate formulation for assessing swirl strength in isothermal flows, as its variation within a fixed cross-sectional domain remains comparatively small and monotonically decreasing, in accordance with the expected characteristics of a flow strength measure. The measurement of  $SN_a$  within 40 mm downstream of the swirler offers a reliable metric for comparing swirl strength and substantially reduces the likelihood of drawing physically inconsistent conclusions. The critical value of  $SN_g$  for the onset of stable-VB in the investigated swirl combustor flows lies between 0.21 and 0.35. This value is reasoned in the present work to exhibit only weak sensitivity to ER, and  $Re_{inlet}$  for  $ER \ge 1.5$  and  $10^4 \le Re_{inlet} \le 1.6 \times 10^5$ . Three-dimensional vortex-core (VC) structures visualized using Q-criterion iso-surfaces and their coherent dynamics characterized from velocity time-series sampled at their footprints reveal that a single-helix VC prevails across all investigated vane angles; up to  $60^{\circ}$ , i.e.,  $SN_{g}=1.15$ . Weaker double-helix characteristics also appear in the investigated cases, arising from quadratic self-interaction of the single-helix tone for vane-angles at or below  $50^{\circ}$ ,  $SN_q = 0.77$ . In contrast, it appears as a quadratically independent tone from the single-helix tone in the largest vane-angle case,  $60^{\rm o}$ , i.e.,  ${\it SN}_g=1.15$  and thus as a distinct helical hydrodynamic mode in that case. Axisymmetric IRZ oscillations coexist and interact with the helical dynamics of the VC in the  $25^{\circ}$  and  $60^{\circ}$ , largest vane-angle, cases. The  $40^{\circ}$ ,  $45^{\circ}$  and  $50^{\circ}$  vane-angle cases exhibit nearly constant-amplitude single-helix precession and associated double-helix precession, consistent with stable limit-cycle oscillations driven by a marginally stable helical mode on the mean state. In contrast, the amplitude of the characteristic helical oscillations in the  $25^{\circ}$  and  $60^{\circ}$  vane-angle cases waxes and wanes strongly, approaching zero at times. The 25° vane-angle case corresponds to the onset of the stable IRZ and the IRZ merges with the separation bubble of centerbody in the  $60^{\circ}$  vane-angle case, both scenarios are known to stabilize precessing modes. This waxing-waning and stabilizing behavior indicates that the characteristic helical oscillations, coherent beyond a threshold, or precession in  $25^{\rm 0}$  and  $60^{0}$  vane-angle cases are sustained by stochastic forcing from background turbulence on the stabilized helical modes. The research also argues a generic applicability of the above observations to isothermal swirl-combustor flows with  $Re_{inlet} \geq 10^4$  and  $ER \geq 2.0$ . Besides a coherent VC strand, a weakly coherent strand also appears to originate from the swirler. The lowest precession frequencies of the coherent strands identified by the above-mentioned spectral analysis appear consistent with separately evaluated oscillation frequencies of the weakly coherent strand in the investigated cases, corroborating a VC-precession origin for the latter structure.

Overall, these results provide (i) a suitable criterion for the onset of stable VB, (ii) guidelines on where to evaluate the criterion to minimize spurious variability, and (iii) a VC topology map against swirl strength that can inform reactor design and diagnostics under isothermal conditions. While the present analysis is restricted to non-reacting flows, it has the ingredients for extension to reacting flows.

### **Acknowledgements**

The authors thank IIT (ISM) Dhanbad and the High-Performance Computing facility at IIT Delhi for the computational support.

## **Funding statement**

The present work is supported by the Faculty Research Scheme (FRS) Grant; FRS (217)/2024-25/FMME of IIT-ISM Dhanbad.

### **Competing interests**

The authors have no conflicts of interest.

# Data availability statement

The data that supports the findings of this study are available from the corresponding author upon reasonable request.

### **Author ORCID**

N.K. Sahu, https://orcid.org/0000-0001-9941-215X

A. Dewan, <a href="https://orcid.org/0000-0002-1561-713X">https://orcid.org/0000-0002-1561-713X</a>

M. Kumar, <a href="https://orcid.org/0000-0002-4478-8798">https://orcid.org/0000-0002-4478-8798</a>

#### **CRediT**

**N.K. Sahu**: Conceptualization, Data curation, Formal analysis, Funding acquisition, Investigation, Methodology, Project administration, Resources, Software, Validation, Visualization, Writing – original draft and Writing – review & editing.

**A. Dewan**: Project administration, Writing – review & editing.

M. Kumar: Conceptualization, Funding acquisition, Resources, Writing – review & editing.

### **Use of AI tools**

An Al-assisted grammar checker (**ChatGPT**, version current as of **28 September 2025**) was used for language polishing only. All scientific content, analyses and conclusions are the authors' own.

### **Ethical statements**

This study involved no human participants or animals and required no ethical approval.

#### References

- [1] P. Weigand, W. Meier, X.R. Duan, W. Stricker, M. Aigner, Investigations of swirl flames in a gas turbine model combustor: I. Flow field, structures, temperature, and species distributions, *Combustion and Flame* 144, 205–224 (2006).
- [2] T. Liu, F. Bai, Z. Zhao, Y. Lin, Q. Du, Z. Peng, Large-eddy simulation analysis on confined swirling flows in a gas turbine swirl burner, *Energies* 10, 2081 (2017).
- [3] N. Fang, L. Zeng, B. Zhang, Z. Li, H. Wang, X. Liu, Numerical simulation of flow and gasification characteristics with different swirl vane angles in a 2000 t/d GSP gasifier, *Applied Thermal Engineering* 153, 791–799 (2019).
- [4] D. Bi, Q. Guan, W. Xuan, J. Zhang, Numerical simulation of GSP gasifier under different swirl angles, *Fuel* 155, 155–163 (2015).
- [5] L. Chen, A.F. Ghoniem, Simulation of oxy-coal combustion in a 100 kWth test facility using RANS and LES: A validation study, *Energy & Fuels* 26, 4783–4798 (2012).
- [6] G. Kewlani, Z.A. LaBry, N. Abani, S.J. Shanbhogue, A.F. Ghoniem, Large-eddy simulations and experimental investigation of flow in a swirl-stabilized combustor, 50th AIAA Aerospace Sciences Meeting including the New Horizons Forum and Aerospace Exposition, Nashville, Tennessee, 02139 (2012).
- [7] G. Kewlani, S. Shanbhogue, A. Ghoniem, Investigations into the impact of the equivalence-ratio on turbulent premixed combustion using particle image velocimetry and large-eddy simulation techniques: V and M flame configurations in a swirl combustor, *Energy & Fuels* 30, 3451–3462 (2016).
- [8] N.W. Chakroun, S.J. Shanbhogue, S. Taamallah, D. Michaels, G. Kewlani, A.F. Ghoneim, Investigation of reduced kinetics mechanisms for accurate LES and scaling of the dynamics of premixed swirling oxy-fuel combustion, *Combustion Science and Technology* 193, 1099–1119 (2021).
- [9] O. Lucca-Negro, T. O'Doherty, Vortex breakdown: a review, *Progress in Energy and Combustion Science* 27, 431–481 (2001).
- [10] J. Zhang, C. Sui, B. Zhang, J. Li, Effects of swirl intensity on flame stability and NO emission in swirl-stabilized ammonia-methane combustion, *Applications in Energy and Combustion Science* 14, 100138 (2023).

- [11] T. Sarpkaya, On stationary and travelling vortex breakdowns, *Journal of Fluid Mechanics* 45, 545–559 (1971).
- [12] J. H. Faler, S. Leibovich, Disrupted states of vortex flow and vortex breakdown, *Physics of Fluids* 20, 1385–1400 (1977).
- [13] M. P. Escudier, N. Zehnder, Vortex-flow regimes, *Journal of Fluid Mechanics* 115, 105–121 (1982).
- [14] Y. Bouremel, M. Yianneskis, A. Ducci., Vorticity and strain dynamics for vortex ring mixing process, *Proceedings 14<sup>th</sup> International Symposium on Applications of Laser Techniques to Fluid Mechanics*, Lisbon, 2008.
- [15] M.O. Vigueras-Zuñiga, A. Valera-Medina, N. Syred, Studies of the precessing vortex core in swirling flows, *Journal of Applied Research and Technology* 10, 755-765 (2012).
- [16] D. Bradley, P.H. Gaskell, X.J. Gu, M. Lawes, M.J. Scott, Premixed turbulent flame instability and NO formation in a lean burn swirl burner, *Combustion and Flame* 115, 515–538 (1998).
- [17] S. Lee, S. Seo, J.C. Broda, S.L. Pal, R.J. Santoro, An experimental estimation of mean reaction rate and flame structure during combustion instability in a lean premixed gas turbine combustor, *Proceedings of the Combustion Institute* 28, 775–782 (2000).
- [18] C. O. Paschereit, E. J. Gutmark, Enhanced stability and reduced emissions in an elliptic swirl-stabilized burner, *AIAA Journal* 46, 1063–1071 (2008).
- [19] A. Spencer, J.J. McGuirk, K. Midgley, Vortex breakdown in swirling fuel injector flows, *Journal of Engineering for Gas Turbines and Power* 130, 021503 (2018).
- [20] S. Taamallah, Y. Dagan, N. Chakroun, S.J. Shanbhogue, K. Vogiatzaki, A.F. Ghoniem, Helical vortex core dynamics and flame interaction in turbulent premixed swirl combustion: A combined experimental and large-eddy simulation investigation, *Physics of Fluids* 31, 025108 (2019).
- [21] N. Syred, J. M. Beer, Combustion in swirling flows: a review, *Combustion and Flame* 23, 143–201 (1974).
- [22] M.P. Escudier, J.J. Keller, Vortex Breakdown: A two-stage transition, AGARD Symposium on Aerodynamics of Vortical Type Flows in Three Dimensions, April 1983.
- [23] V.Y. Mudkavi, The phenomenon of vortex breakdown, *Proceedings of the Fluid Dynamics Symposium* 9, 123–135 (1993).

- [24] R. E. Spall, T. B. Gatski, C. E. Grosch, A criterion for vortex breakdown, *Physics of Fluids* 30, 3434–3440 (1987).
- [25] P. Billant, J.M. Chomaz, P. Huerre, Experimental study of vortex breakdown in swirling jets, *Journal of Fluid Mechanics* 376, 183–219 (1998).
- [26] N. A. Chigier, A. Chervinsky, Aerodynamic study of turbulent burning free jets with swirl, *Symposium (International) on Combustion* 11, 489–499 (1967).
- [27] N. A. Chigier, A. Chervinsky, Experimental investigation of swirling vortex motion in jets, *Journal of Applied Mechanics* 34, 443–451 (1967).
- [28] N. A. Chigier, J. M. Beer, Velocity and static-pressure distributions in swirling air jets issuing from annular and divergent nozzles, *Journal of Fluids Engineering* 86, 788–796 (1964).
- [29] G. Vignat, D. Durox, S. Candel, The suitability of different swirl number definitions for describing swirl flows: Accurate, common and (over-) simplified formulations, *Progress in Energy and Combustion Science* 89, 100969 (2022).
- [30] G. Ogus, M. Baelmans, M. Vanierschot, On the flow structures and hysteresis of laminar swirling jets, *Physics of Fluids* 28, 123604 (2016).
- [31] Y. Gao, X. Zhang, W. Han, J. Li, L. Yang, Effects of swirl number and bluff body on swirling flow dynamics, *AIP Advances* 13, 025246 (2023).
- [32] M. Vanierschot, M. Percin, B.W. Oudheusden, Double helix vortex breakdown in a turbulent swirling annular jet flow, *Physical Review Fluids* 3, 034703 (2018).
- [33] M.P. Escudier, A.K. Nickson, R.J. Poole, Influence of outlet geometry on strongly swirling turbulent flow through a circular tube, *Physics of Fluids* 18, 125103 (2006).
- [34] X. Lu, S. Wang, H.-G. Sung, S.Y. Hsieh, V. Yang, Large-eddy simulations of turbulent swirling flows injected into a dump chamber, *Journal of Fluid Mechanics* 527, 171–195 (2005).
- [35] A.K. De, S. Sarkar, Vortex-shedding modes of a streamwise and transversely rotating sphere undergoing vortex-induced vibrations, *Physics of Fluids* 36, 061705 (2024).
- [36] J. Samarasinghe, S.J. Peluso, B.D. Quay, D.A. Santavicca, The three-dimensional structure of swirl-stabilized flames in a lean premixed multi-nozzle can combustor, *Journal of Engineering for Gas Turbines and Power* 138, 031502 (2016).

- [37] A.A. Adedoyin, D.K. Walters, S. Bhushan, Investigation of turbulence model and numerical scheme combinations for practical finite-volume large-eddy simulations, *Engineering Applications of Computational Fluid Mechanics* 9, 324–342 (2015).
- [38] Y. Dong, Y. Yan, C. Liu, New visualization method for vortex structure in turbulence by lambda2 and vortex filaments, *Applied Mathematical Modelling* 40, 500–509 (2016).
- [39] D.G. Lilley, Swirl flows in combustion: a review, AIAA Journal 15, 1063–1078 (1977).
- [40] W.L.H. Hallett, D.J. Toews, The effects of inlet conditions and expansion ratio on the onset of flow reversal in swirling flow in a sudden expansion, *Experiments in Fluids* 5, 129–133 (1987).
- [41] S. Terhaar, T.G. Reichel, C. Schrödinger, L. Rukes, K. Oberleithner, C. O. Paschereit, Vortex breakdown and global modes in swirling combustor flows with axial air injection, *Journal of Propulsion and Power* 31, 219–229 (2015).
- [42] S. Taamallah, Z.A. LaBry, S.J. Shanbhogue, M.A.M. Habib, A.F. Ghoniem, Correspondence between "stable" flame macrostructure and thermo-acoustic instability in premixed swirl-stabilized turbulent combustion, *Journal of Engineering for Gas Turbines and Power* 137, 071505 (2015).
- [43] S. B. Pope, Turbulent Flows, Cambridge University Press, 2000.
- [44] S. Hickel, C.P. Egerer, J. Larsson, Subgrid-scale modeling for implicit large eddy simulation of compressible flows and shock-turbulence interaction, *Physics of Fluids* 26, 106101 (2014).
- [45] CFD Direct 2024. Energy Equation in OpenFOAM. CFD Direct Documentation. Available at: https://doc.cfd.direct/openfoam/energy-equation/#x1-100006 (accessed 13 June 2025).
- [46] OpenFOAM Foundation 2023. eddyDiffusivity.H source file, OpenFOAM v10 C++ Source Code Guide. Available at: <a href="https://cpp.openfoam.org/v10/eddyDiffusivity8H source.html">https://cpp.openfoam.org/v10/eddyDiffusivity8H source.html</a> (accessed 13 June 2025)
- [47] P. Kakka, K. Anupindi, Assessment of sub grid-scale models for large-eddy simulation of a planar turbulent wall-jet with heat transfer, *International Journal of Heat and Mass Transfer*, 153, 119593 (2020).

- [48] OpenFOAM Foundation 2022. Open-source software from the OpenFOAM Foundation. *OpenFOAM v10* C++ *Source Code Guide*. Available at: <a href="https://cpp.openfoam.org/v10/">https://cpp.openfoam.org/v10/</a> (accessed 13 June 2025)
- [49] OpenFOAM Foundation 2022. Turbulent inlet directory reference. *OpenFOAM v10* C++ *Source Code Guide*. Available at: <a href="https://cpp.openfoam.org/v10/dir\_966d1c898e0249b61a6dc8a3eac9d5e1.html">https://cpp.openfoam.org/v10/dir\_966d1c898e0249b61a6dc8a3eac9d5e1.html</a> (accessed 13 June 2025)
- [50] ANSYS Inc. 2023. Turbulence Intensity. ANSYS Fluent User's Guide. Available at: <a href="https://www.afs.enea.it/project/neptunius/docs/fluent/html/ug/node238.htm">https://www.afs.enea.it/project/neptunius/docs/fluent/html/ug/node238.htm</a> (accessed 13 June 2025)
- [51] T.J. Poinsot, S. K. Lele, Boundary conditions for direct simulations of compressible viscous flows, *Journal of Computational Physics* 101, 104–129 (1992).
- [52] Q. Yupeng, Impact of LES sub grid-scale modelling on the acoustic and flow properties for Helmholtz resonators without mean flow, Master's Thesis, *Technical University Munich* (2016).
- [53] S. Krajnovic, L. Davidson, A mixed one-equation sub grid model for large-eddy simulation, *International Journal of Heat and Fluid Flow* 23, 413–425 (2002).
- [54] P. Vincent, A. Jameson, Facilitating the adoption of unstructured high-order methods amongst a wider community of fluid dynamicists, *Mathematical Modelling of Natural Phenomena* 6, 97–140 (2011).
- [55] S. Saaed, PIMPLE algorithm and pimple-foam solver: Open-source CFD course, Chalmers University of Technology, September 2022. Available at: https://www.tfd.chalmers.se/~hani/kurser/OS CFD 2022/lectureNotes/PIMPLE.pdf
- [56] H. Jasak, Error analysis and estimation for the finite-volume-method with applications to fluid flows, PhD Thesis, *University of London* (1996).
- [57] N.K. Sahu, A. Dewan, M. Kumar, Characterizing flow field transition in a pressurized tangential-injection gas-fired reactor, *Thermal Science and Engineering Progress* 41, 101811 (2023).
- [58] K. Manoharan, M. Fredreick, S. Clees, J.O. Connor, S. Hemachandra, A weakly nonlinear analysis of the precessing vortex core oscillation in a variable swirl turbulent round jet, *Journal of Fluid Mechanics* 884, A29 (2020).
- [59] T. Hiejima, Streamwise vortex breakdown due to the interaction with crossed shock waves, *Journal of Fluid Mechanics* 973, A41 (2023).

- [60] J.S. Bendat, A.G. Piersol, Random Data: Analysis and Measurement Procedures, *John Wiley & Sons*, 2010.
- [61] T. Poinsot, P. Wolf, G. Staffelbach, L.Y.M. Gicquel, J. D. Muller, Identification of azimuthal modes in annular combustion chambers, *Center for Turbulence Research*, Annual Research Briefs, 249–258 (2011).
- [62] K. Srinivasan, P. Panickar, G. Ramana, B. Kim, D.R.Williams, Study of coupled supersonic twin jets of complex geometry using higher-order spectral analysis, *Journal of Sound and Vibration* 323, 910–931 (2009).
- [63] M.V. Tabib, G. Lane, W. Yang, M.P. Schwarz, CFD study of single phase and multiphase (liquid–liquid) pump-mixer: Analyzing design parameters, flow structures and turbulence, *Chemical Engineering Science* 80, 55–69 (2012).
- [64] A.K. Pandey, P.K. Mohapatra, Flow dynamics and pollutant transport at an artificial right-angled open-channel junction with a deformed bed, *Journal of Hydraulic Engineering* 149, 04023006 (2023).
- [65] M. Vanierschot, J. S. Müller, M. Sieber, M. Percin, B. W. Oudheusden and K. Oberleithner, Single- and double-helix vortex breakdown as two dominant global modes in turbulent swirling jet flow, *Journal of Fluid Mechanics* 883, A31 (2020).
- [66] I.V. Litvinov, D.A. Suslov, E.U. Gorelikov, S.I. Shtork, Swirl number and nozzle confinement effects in a flat-vane axial swirler, *International Journal of Heat and Fluid Flow* 91, 108812 (2021).
- [67] K. Manoharan, S. Hansford, J.O. Connor, S. Hemachandra, Instability mechanism in a swirl flow combustor: Precession of vortex core and influence of density gradient, *Proceedings of ASME Turbo Expo: Turbine Technical Conference and Exposition* GT2015, 42985 (2015).
- [68] S. Gupta, S. Shanbhogue, M. Shimura, A. Ghoniem, S. HemaChandra, Impact of a centerbody on the unsteady flow dynamics of a swirl nozzle: Intermittency of precessing vortex core cocillation, *Journal of Engineering for Gas Turbines and Power* 144, 021014 (2022).